HIGH PRECISION MASS MEASUREMENTS NEAR N=Z=33

By

Peter Henry Schury

A DISSERTATION

Submitted to
Michigan State University
in partial fulfillment of the requirements
for the degree of

DOCTOR OF PHILOSOPHY

Department of Physics

2007

ABSTRACT

HIGH PRECISION MASS MEASUREMENTS NEAR N=Z=33

By

Peter Henry Schury

The Low Energy Beam and Ion Trap (LEBIT) facility at the NSCL converts the beam of rare isotope ions produced at relativistic energies by in-flight separation of heavy projectile fragments into a low energy beam. To achieve this, gas stopping and advanced beam manipulation techniques are used. The facility's first experimental apparatus is a 9.4 T Penning trap mass spectrometer for performing high-precision mass measurements on short-lived isotopes. Within this work important components of the LEBIT facility have been developed and a series of high precision mass measurements performed.

Mass measurements of ^{63,64}Ga, ^{64,65,66}Ge, ^{66,67,68}As and ^{69}Se at the LEBIT facility at the NSCL by Penning trap mass spectrometry have been performed within this work. Masses of the N=Z nuclei ^{66}As and ^{64}Ge have been determined with uncertainties of δm/m = 5x10^{-7} and 6x10^{-8}, respectively, representing a more than 10-fold improvement in precision over previous measurements. For ^{63,64}Ga, ^{65,66}Ge, ^{67,68}As and ^{69}Se relative mass uncertainties of δm/m < 5x10^{-8} have been obtained. ^{69}Se is found to be 135 keV more bound than the value listed in the 2003 Atomic Mass Evaluation. Using theoretical Coulomb shift energies in combination with the experimental mass values, improved mass predictions for ^{63}Ge, ^{64,65}As, ^{66,67}Se and ^{68,69}Br have been made. These predicted mass values, in conjunction with the experimentally determined mass values, are used to calculate improved effective lifetimes of the rp-process waiting point nuclei ^{64}Ge and ^{68}Se. It is shown that ^{64}Ge is less of a waiting

point while ^{68}Se poses a larger delay in the rp-process than previously thought. The more precise mass values now available in this region are also used to investigate the neutron-proton pairing energy of odd-odd N=Z nuclei.

Study without reflection is a waste. Reflection without study is a danger.
– Confucius

Dedicated to the number zero; thanks for nothing.

ACKNOWLEDGMENTS

The results in this thesis are certainly not the result of my efforts alone, nor are they derived solely from the efforts of the research group which I have been lucky enough to have been a part of. Without the many support divisions at the NSCL – the design department, the machine shop, the computer support group, the electricians, the plumbers, and of course the cyclotron operators and A1900 group who provided the rare isotope beams for us to work with – this thesis would only report simulations. I want to thank everyone at the NSCL for being such great team players. I would like to extend my personal thanks to Ben Arend, who never balked when I asked him to read a mechanical drawing for me, as well as to Mike Noe and Arlieta Sawyer, who were always cheerfully helpful in procuring needed supplies, even if it required a late night call to suppliers in Japan.

I wish to thank Céline Guénaut and Michael Block for helping in the preparation of this thesis. They read numerous draft copies and made wonderfully helpful suggestions.

I would also like to express immense gratitude to Stefan Schwarz, Prof. Dave Morrissey and my advisor Prof. Georg Bollen. The three of you have provided so much wonderful advice, both personal and professional; I would have been lost without you. Under your tutelage I believe I have truly grown from a student into a researcher. I would also like to thank the wonderful graduate students with whom I worked throughout this project, in particular Ryan Ringle and Sun Tao.

On a more personal note, I would like to thank my parents for encouraging my

curiosity when I was young and instilling me with a desire for education and a strong work ethic. And also for never asking me when I would get a real job. I must also thank my wife, Beth, and her family for all the support they have provided me – your faith in me hasn't gone unappreciated.

TABLE OF CONTENTS

LIST OF TABLES

LIST OF FIGURES

Images in this dissertation are presented in color.

CHAPTER 1

Introduction

The precise determination of the masses of atomic nuclei with equal and nearly equal numbers of neutrons, N, and protons, Z, is of interest for nuclear astrophysics and the study of nuclear structure, as well as for tests of fundamental interactions. In the study of fundamental interactions, the determination of Q-values for T=1, $0^+ \rightarrow 0^+$ super-allowed β-decays provide data necessary for testing the Conserved Vector Current hypothesis [1]. Such measurements also provide the best determination of the V_{ud} term of the Cabibbo-Kobayashi-Maskawa matrix [2]. The strength of the T=0 neutron-proton pairing interaction, of great importance for the understanding of nuclear structure along the N=Z line [3], can be probed using binding energies of N=Z nuclei and their neighbors. In nuclear astrophysics, calculations determining the pathway of the rp-process, believed to synthesize elements beyond iron in Type I X-ray bursts [4, 5], rely on proton capture Q-values of nuclei near N=Z. In each of these cases, the important data – β-decay Q-values, binding energies and proton capture Q-values – can be obtained by precise atomic mass measurements.

The measurement of atomic masses by mass spectroscopy stretches back more than 80 years, to Aston [6]. Since then a number of complementary methods have been developed to measure atomic masses. The most precise method of measuring

atomic masses available today is through the use of Penning trap mass spectrometers [7].

While the valley of β-stability follows the N=Z line for light nuclei, it curves toward more neutron rich isotopes beyond ^{32}S. The heaviest stable N=Z nucleus is ^{40}Ca. The study of heavier N=Z nuclei requires their production by artificial means.

A number of methods exists for production of such so-called rare isotopes. Perhaps the most powerful method, with respect to the ability to reach isotopes far from stability, is projectile fragmentation. Until recently, however, this method has been incompatible with the use of Penning trap mass spectrometers due to the high beam energy and the poor beam quality. In order to allow Penning trap mass spectrometry of nuclei produced by fast projectile fragmentation the Low Energy Beam and Ion Trap (LEBIT) facility has been constructed at the National Superconducting Cyclotron Laboratory at Michigan State University.

1.1 Importance of Atomic Masses

One of the most fundamental properties of an atomic nucleus is its mass, which is the sum of the masses of the constituent nucleons less the total energy required to separate them – the binding energy. Thus, how tightly bound an atomic nucleus is can be directly inferred from its mass. Knowledge of nuclear binding energies of rare isotopes is relevant to a number of areas of research. These include tests of fundamental interactions, the study of nuclear structure and the modeling of astrophysical processes.

1.1.1 Fundamental Interactions

The determination of atomic masses with very high accuracy has played and will continue to play an important role in the study of the weak interaction. According

to the Conserved Vector Current (CVC) hypothesis, the vector component of the weak interaction is completely uncoupled from the strong interaction. As such, it is expected that the β-decay strength, measured by the so-called ft-value, should be constant in all super-allowed $0^+ \to 0^+$ transitions. In order to calculate the ft-value of a decay, three quantities are needed: the β-decay lifetime, the branching ratio for the $0^+ \to 0^+$ transition and the Q-value, Q_{EC}. The latter is equivalent to the mass difference between the mother and daughter nucleus.

Small theoretical corrections need to be applied to the ft-values to account for Coulomb and radiative effects. The result is a corrected $\mathcal{F}$t value, which should be constant among all super-allowed $0^+ \to 0^+$ transitions. At this time, very precise $\mathcal{F}$t values are available for 12 such candidates, confirming CVC at a level of 3×10^{-4} [1].

Recently, precision mass measurements of ^{38}Ca were performed at the LEBIT facility with a mass precision of $\delta m/m < 10^{-8}$ [8, 9]. With this high precision mass measurement, ^{38}Ca became a new candidate for testing the CVC hypothesis. Beyond A=62, however, there is an increase in the uncertainty of theoretical corrections required for calculating $\mathcal{F}$t values [10]. High-precision measurements of Q_{EC} (as well as half-life and branching ratios) for such candidates could provide a useful check on these calculations and eventually lead to an improved test of the CVC hypothesis. One such possible candidate is the short-lived ^{66}As ($T_{1/2} = 96$ ms), whose mass was, for the first time, precisely measured at LEBIT [11] as part of this work. While the mass uncertainty achieved in this first measurement of ^{66}As was not yet sufficient to test the CVC hypothesis, it is anticipated that future measurements of this nuclide at LEBIT will provide sufficient precision.

1.1.2 Nuclear Structure

Through systematic mass measurements, it is possible to probe nuclear structure. Effects of shell structure, such as shell closures and the onset of deformation, are visible

as changes in trends of nucleon separation energies. Systematic mass measurements provide the first evidence for the change of shell structure far from the valley of stability. Since the discovery of a region of nuclear deformation near the magic number N=20 in neutron-rich isotopes [12], much interest has been paid to the evolution of magic numbers far from stability.

While neutron-neutron and proton-proton pairing has a strong effect on nuclear binding across the nuclear chart, a very interesting local effect appears along the N=Z line. It is experimentally known that the binding energy of N=Z nuclei is considerably increased compared to nuclei nearby with N≠Z. This increased binding energy was first explained by Wigner in terms of SU(4) symmetry [13]. It has also been interpreted as T=0 neutron-proton pairing [14]; for N=Z isotopes, protons and neutrons occupy the same orbitals with essentially the same wave functions, allowing the neutron and proton to interact more strongly than for N≠Z isotopes. There is an expectation that this Wigner energy may vanish as the N=Z line approaches ^{100}Sn due the effect of increased Coulomb and spin-orbit interactions which break the orbital symmetry [15]. However, it has also been speculated that there may be a mid-shell restoration of the Wigner energy due to pseudo-SU(4) symmetry in the pf-shell [16]. Beyond Z=32, experimental values from which neutron-proton pairing energies of N=Z nuclei can be calculated have largely been based on extrapolations or suffered from large experimental uncertainties. New mass measurements of ^{66}As and nearby nuclei [11] performed within this work have considerably improved the situation and reduced the uncertainty of n-p pairing energies in this region.

1.1.3 Nuclear Astrophysics

The rapid proton capture process (rp-process) is believed to drive Type I X-ray bursts in accreting neutron stars, producing elements beyond iron [4, 5]. The rp-process proceeds along isotonic chains until proton capture is inhibited, either by proton

decay or photodisintegration. When the rp-process reaches an equilibrium between proton capture and loss, the process must wait for the β-decay of the equilibrium nucleus before it can continue [4]. These nuclei are the so-called waiting point nuclei.

The lifetimes of waiting point nuclei are of particular interest as they set the time scale for the rp-process, which shapes the observed X-ray burst light curves [17, 18, 19]. The waiting point lifetimes also determine the final composition of the burst ashes, important for reliable predictions of the composition of neutron star crusts [20]. Proton capture and β-decay rates determine the effective lifetime of nuclei in X-ray bursts. As the reaction rates have an exponential dependence on the proton separation energy, Q_p, accurate X-ray burst model calculations require mass values with small uncertainties, desirably less than 10 keV [19, 20].

As the N=Z line approaches the proton drip line, and therefore the rp-process pathway, near N=Z=33 [19], mass uncertainties in excess of 100 keV are typical at present. This is the region of the nuclear chart where the rp-process is believed to encounter three relatively long-lived waiting point nuclei: ^{64}Ge, ^{68}Se and ^{72}Kr [20]. Reduced mass uncertainties at and near these waiting points improve our understanding of the rp-process timescale. Precision mass measurements of several isotopes near N=Z=33 have been made as part of this work.

1.2 Methods of Atomic Mass Measurements of Rare Isotopes

There exist numerous means by which to determine atomic masses. Indirect measurements, such as decay and reaction energy measurements, provide mass differences. Direct measurements, such as time-of-flight, magnetic rigidity and cyclotron frequency measurements, in general provide mass ratios. The present work concentrates on the direct method of cyclotron frequency measurements in a Penning trap.

1.2.1 Indirect Measurements of Atomic Masses

Indirect measurements derive atomic masses from measurements of reaction or decay Q-values. These techniques have long been applied to nuclei near and far from stability. Reaction Q-value measurements provide the only means for determining masses of particle unbound nuclei. Decay measurements provide a mass difference between mother and daughter nuclei. For nuclei far from stability, long chains of such measurements are often required to connect new measurements to a well-known mass, which can result in a compounding of errors. For β-decay end-point measurements there are additional uncertainties in detector response, as well as low statistics near the end-point, that can cause systematic errors [21].

1.2.2 Direct Measurements of Atomic Masses

The first mass measurements of sufficient precision to detect the deviation between atomic mass and atomic number (a result of the binding energy) were performed by Aston in the early 1920's using a magnetic spectrograph [6]. In the original system, the deflection of an ion passing through a powerful magnet was measured on a photographic plate. Mass ratios were determined through deflection comparisons.

The first direct mass measurements on rare isotopes were performed at CERN/PS in the 1970's with a magnetic spectrometer. The direct measurement of the mass of the very short-lived nucleus ^{11}Li, later found to be a halo nucleus, was performed and the onset of an enhancement in neutron binding for neutron-rich sodium isotopes near N=20 [12] was discovered. These measurements were followed by a series of mass measurements of long isotopic chains of alkali elements using a double-focusing spectrometer at CERN/ISOLDE [22]. The success of these pioneering measurements motivated groups throughout the world to improve and develop new methods for direct mass measurements of rare isotopes.

Today a number of magnetic spectrometers are in use worldwide for mass mea-

surements of rare isotopes. For the direct mass measurement of isotopes produced by projectile fragmentation, systems are used which combine magnetic rigidity and time-of-flight measurements. Examples of such devices include the SPEG [23] facility at GANIL and the S800 [24] at the NSCL. While the achievable mass precision is typically 100 keV - 1 MeV [25], the technique has the ability to access nuclei very far from stability and with very short half-lives.

The resolution of time-of-flight spectrometers is ultimately limited by the length of the flight path. The use of a storage ring, such as the Experimental Storage Ring (ESR) [26] at GSI, increases the flight path by a factor equal to the number of revolutions. When the ring is operated in isochronous mode the time-of-flight resolving power can be increased by an order of magnitude compared to that from a single-pass time-of-flight spectrometer. Using this technique the masses of short-lived neutron-deficient isotopes have been measured with accuracies of $\approx$100 keV [27].

Frequency measurements allow for yet greater resolution. At the ESR ions in the ring can be cooled with an electron cooler to allow for Schottky detection of the circulating ions. The revolution frequency can then be determined using Fourier analysis of the signal induced by the ions in pickup electrodes. This technique increases the resolving power by as much as an order of magnitude over the time-of-flight method, but the cooling time limits the technique to ions with halflives of $T_{1/2} > 5$ s. The Schottky technique has nonetheless been used to measure masses of more than 500 neutron-deficient nuclei, with a typical mass precision 20 - 50 keV [28].

Another device relying on frequency measurements is the Smith-type transmission spectrometer MISTRAL [29] at CERN/ISOLDE. In the MISTRAL spectrometer the cyclotron frequency, ν_c, of ions is measured through application of radiofrequency signals to a small RF cavity through which the beam passes twice. If the frequency of the applied signal, ν_{RF}, is such that $\nu_c = \nu_{RF} \cdot (n+1/2)$, the acceleration on the first pass will be compensated by the deceleration in the second pass and the beam

will be able to pass through a narrow extraction slit. This technique has been used to measure very short-lived nuclei, such as ^{11}Li, with mass precisions of δm/m$<10^{-6}$ [30].

Penning trap mass spectrometers can be used to determine the cyclotron frequency of ions in a strong, homogeneous magnetic field. They provide the highest resolving power and greatest mass accuracy of any technique available [7]. For stable isotopes, relative mass precisions of δm/m $< 10^{-10}$ [31] have been reached. For short-lived nuclei, precisions of δm/m $< 10^{-8}$ have been achieved [8, 9].

The first Penning trap to be installed at a rare isotope beam facility was ISOLTRAP [32] at CERN/ISOLDE. Based on the immense success of that facility, Penning traps have been installed at a several rare isotope beam facilities throughout the world. LEBIT at the NSCL is the first Penning trap mass spectrometer [33] to perform mass measurements on rare isotopes created in fragmentation reactions at high energies ($\approx$100 MeV/A) [8, 9, 11].

1.3   Rare Isotopes Production and Penning Trap Mass Measurements

Three methods are dominantly used to create isotopes away from the valley of stability: isotope separation on-line (ISOL), low-energy fusion-evaporation reactions and fast projectile fragmentation at high energies. Each method has advantages and restrictions as the isotopes delivered by each differ in beam quality and quantity. All of these production methods have been successfully combined with Penning trap mass spectrometry.

The ISOL technique uses an energetic light projectile, such as a proton beam, impinging a thick target of suitable material, such as Tantalum. Rare isotopes are produced in the target through fission, spallation and fragmentation reactions, depending

on the target material. Maintaining the target at high temperatures ($>2000°C$) allows rare isotopes to diffuse out of the target into an ion source to form an ion beam. Because of its reliance on diffusion, ISOL production does not lend itself well to the production of refractory chemical elements and the production of short-lived isotopes is limited by diffusion times. Benefits of the ISOL production technique are the high beam intensity and low energy beam, generally 40 - 60 keV, and low emittance, which make the ISOL technique particularly well suited for trapped ion studies, such as Penning trap mass spectrometry. The pioneering ISOLTRAP experiment continues to operate at the ISOL facility ISOLDE at CERN. A new facility, TITAN [34], is under construction at ISAC/TRIUMF in Vancouver, Canada, which will make use of highly-charged rare isotope ions.

Medium energy ions impinging a thin target can produce radioisotopes through fusion-evaporation and fission reactions. This technique is chemically independent and fast, but the range of isotopes that can be produced is limited to relatively proton-rich isotopes. The fusion-evaporation technique is the only production method which offers access to trans-uranium elements. At the SHIP facility at GSI, the heaviest elements [35] are created through fusion-evaporation reactions of heavy projectiles, such as ^{70}Zn, impinging very heavy targets, such as ^{208}Pb. The ATLAS facility at Argonne National Laboratory uses light and medium mass projectiles and targets, such as ^{40}Ca impinging carbon, to create rare isotopes with kinetic energies of a few tens of MeV.

Fusion-evaporation reaction products exit the target with typical energies of between 100 keV/A and a few MeV/A. To couple such beams to Penning trap mass spectrometers low-pressure gas stopping cell systems are used for "post-thermalization" of the fusion-evaporation reaction products after magnetic separation. This is done at the Canadian Penning trap (CPT) [36] at ATLAS and SHIPTRAP [37] at GSI.

In a similar way, the ion guide isotope separation online (IGISOL) method [38] at

JYFL produces rare isotopes by impinging a primary beam on a thin target located directly inside a low-pressure gas cell. The reaction products exit the target and are thermalized in the buffer gas and extracted by gas flow. The JYFLTRAP [39] Penning trap mass spectrometer makes use of rare isotope beams produce with such a method.

Projectile fragmentation with in-flight separation is a powerful technique for rare isotope production. This technique makes use of a high energy (>50 MeV/A) heavy ion impinging a thin light element target and fragmenting more-or-less combinatorially. In doing so a wide range of isotopes with less neutrons and protons than the projectile are produced. A powerful magnetic separator is used to select the isotope of interest. Projectile fragmentation with in-flight separation is used at several facilities worldwide. They include SISSI and LISE at GANIL [40] in France, the FRS [41] at GSI in Germany, RIPS [42] at RIKEN in Japan and the A1900 [43] at the NSCL in the USA.

There are many advantages to this method. It is chemically independent. The fragment beam experiences virtually no delay in passing through the target and requires less than a microsecond to pass through the fragment separator, which allows access to extremely short-lived isotopes without decay losses. Furthermore, it can produce isotopes much further from the valley of β-stability, particularly on the neutron rich side, than any other technique. A drawback of the technique is that the fragmentation process results in a high energy (>50 MeV/A) beam with large emittance, which until recently precluded trapped ion experiments. The LEBIT facility at the NSCL is so far the only facility to successfully demonstrate the ability to perform Penning trap mass spectrometry with ions created by fast projectile fragmentation.

1.4 Outline for this Thesis

This thesis represents the culmination of more than six years of intense and concerted efforts to help create a facility to perform trapped ion experiments on rare isotopes created at relativistic energies. The design, construction and commissioning of the LEBIT facility, which began in 2000, has been a long and at times difficult project. At the time that I joined this project, the LEBIT facility was only a concept – the experimental vault which houses most of the facility was not even built yet. After roughly two years of computer simulations performed by Sun Tao, Ryan Ringle, Stefan Schwarz and myself, the facility was still largely conceptual, but it was clear how to proceed. After one and a half years of manual labor – assembling electronics, mounting electrodes in vacuum chambers, running wires for the control system and the like – the facility was complete and ready to be tested. While offline tests showed that the beam cooler-and-buncher as well as the Penning trap worked as expected, the first online tests yielded unexpected difficulties with impurities in the beam extracted from the gas stopping station. After one more year spent improving the system and implementing techniques to purify the beam extracted from the gas cell, in May, 2005, success came in the form of a high precision mass measurement of ^{38}Ca. Since then, the precise masses of more than 30 rare isotopes have been measured at LEBIT.

My thesis will continue with a discussion of basic methods for low-energy beam and trapped ion manipulation in chapter 2. Chapter 3 will provide an overview of the LEBIT facility. The facility is used to convert the energetic fragmentation beam into a low energy beam suitable for trapping. The three main components, the gas stopping station, the beam cooler-and-buncher and the Penning trap, will be described in detail.

Chapter 4 will discuss simulations performed to assist in the design for the LEBIT gas stopping station. Chapter 5 will be to describe the methods implemented to purify the low energy beam extracted from the gas cell.

In chapter 6 I will present mass measurement data for ^{63,64}Ga, ^{64,65,66}Ge, ^{66,67,68}As and ^{69}Se. These N$\approx$Z nuclei are on or near the path of the rp-process. In addition to the very high precision measurements of these nuclei, Coulomb shift calculations [19] were used to predict the masses of ^{65}As, ^{66,67}Se and the proton unbound ^{69}Br with an estimated precision of 100 keV. I will end chapter 6 by presenting calculations for the effective lifetimes of the rp-process waiting point nuclei ^{64}Ge and ^{68}Se.

CHAPTER 2

Basic Ion Trapping Techniques

Ion traps are a powerful tool for the study of charged particles at rest. Trapped charged particles can be used to probe fundamental properties of particles such as their mass [7] and g-factor [44] with extraordinary precision. The use of traps allows the study of charged particles in free space, where they can be maintained and manipulated for extended periods. Such extended storage times have been one of the keys to extremely high-precision measurements. Ions traps have also gained importance in ion beam manipulation such as ion cooling and bunching [45, 46] and purification [47, 48]. In particular, the ability to cool trapped ions has been of great importance in achieving high-precision measurements, while bunching techniques have greatly improved the efficiency of capturing ions in traps.

While numerous schemes have been developed for trapping charged particles, the most prevalent configurations currently in use for trapping low energy ions are the Paul trap [49] and the Penning trap [50]. This chapter will discuss the basic principles of Paul traps and Penning traps. Their application as relevant to this thesis - ion cooling and bunching, mass filtering and mass spectrometry - will also be discussed.

2.1 Radiofrequency Ion Confinement

Radiofrequency (RF) ion traps find application in many fields of research. In analytical chemistry, 2-dimensional RF traps – or "ion guides" – are used to transport ions from electrospray chambers to mass spectrometers [51], as well as for ion-molecular reactors [52, 53]. Residual gas analyzers (RGAs) use RF ion guides to determine residual gas compositions by operating the ion guides in a mass selective mode which will be described later. Linear 3-dimensional RF traps have been used in the development of atomic clocks [54] and are often used to confine ions in dilute buffer gas for ion cooling purposes [45, 46] as will be discussed later.

According to Earnshaw's theorem there is no electrostatic potential with a local minimum in free space. If this is so, how can a charged particle be trapped? One approach, developed by Kingdon, is to place the trap minimum inside an electrode (allowed by Earnshaw's theorem) and "trap" an ion in an orbit about the electrode [55]. In such "traps" the ions can never come to rest, limiting the usefulness of this technique.

Another technique for trapping ions avoids the consequences of Earnshaw's theorem through the application of non-static oscillating electric fields. Suppose an ion is placed inside a set of parallel plates, as shown in Fig. 2.1a. If the potential difference between the plates is given by $\Phi(t) = U \cdot cos(\omega t)$ then the electric field will be given by $E(t) = -\frac{U}{d} \cdot cos(\omega t) = E_0 \cdot cos(\omega t)$. An ion initially at rest between the plates will oscillate between the plates, its displacement given by $x(t) = -E_0 \frac{q}{m\omega^2} \cdot cos(\omega t)$. Thus the field opposes the displacement but on average exerts no force.

If curved plates are used, as shown in Fig. 2.1b, the situation changes. Applying the same potential difference yields

$$E(t) = \frac{U}{r} \frac{1}{lnR_1/R_2} \cdot cos(\omega t) = E_0 \cdot cos(\omega t). \tag{2.1}$$

The ion will be pushed toward the concave plate in the first half of the cycle. In the
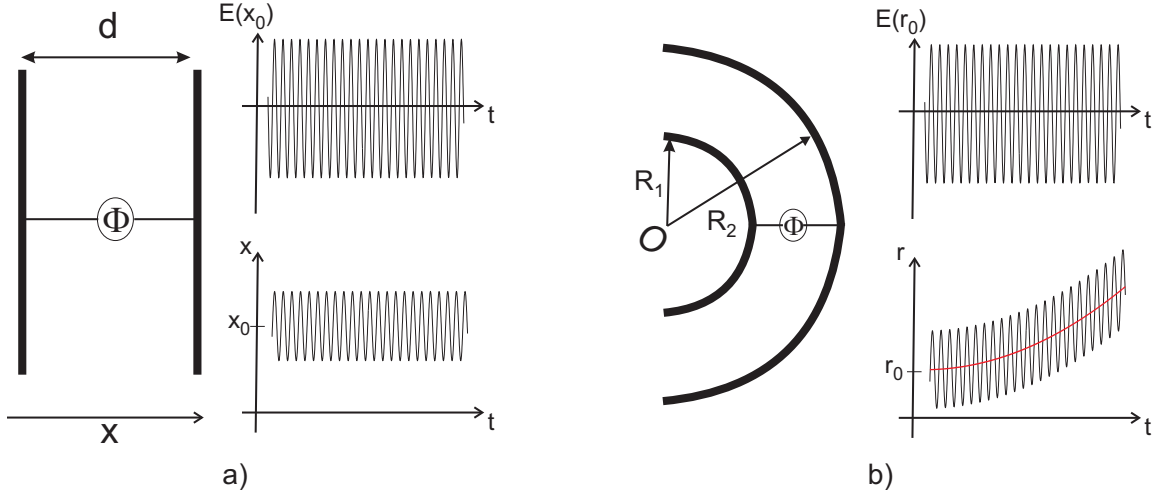
Figure 2.1. Sketch of a) parallel and b) curved plates for visualization of net force effect of inhomogeneous RF electric field. The red curve in b) represents the time averaged drift motion of the ion.

second half of the cycle the ion will be pushed away from the concave plate. However, since E_0 is non-uniform, the average force experienced in the second half cycle will not balance that experienced in the first half and an ion initially at rest will "walk" to the concave plate, as illustrated in Fig. 2.1b. An ion experiencing an oscillating non-homogeneous electric field experiences a non-zero average force. This time-averaged force caused by an oscillating non-uniform electric field can be described by an electric pseudo-potential [56], given by

$$D = \frac{q}{4m\omega^2}(E_0^2). \qquad (2.2)$$

Thus, if E_0^2 has a local minimum in free space and is modulated by a time-oscillating function a pseudo-potential with a local minimum in free space – also known as a trap – will be created.

Consider a set of electrodes consisting of pair of hyperbolic cylinders with perpendicular cross-sections, as shown in Fig. 2.2a. If a potential difference, U, is applied between adjacent electrodes, a quadrupole electric potential is formed in the cross-sectional plane, as shown in Fig. 2.2b. The electric potential and field are given
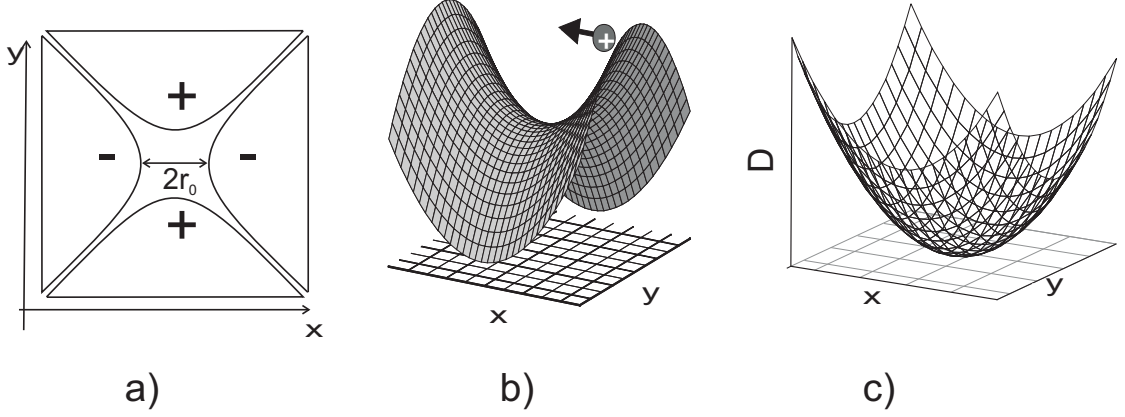
Figure 2.2. a) Sketch of cross-sectional view of a quadrupole electrode system. b) Quadrupole electric potential created by static potentials applied to such electrodes. c) Pseudo-potential experienced by an ion if the potential applied are modulated by a time-oscillating function.

by

$$\phi = U \cdot \frac{x^2 - y^2}{r_0^2} \tag{2.3}$$

and

$$\vec{E} = \begin{pmatrix} -x \\ y \end{pmatrix} \frac{2U}{r_0^2}, \tag{2.4}$$

where $2r_0$ is the inter-electrode separation and x and y are measured relative to the center of the set of electrodes.

If U is modulated by $f(\omega t)$, an oscillatory function with frequency ω, then from eq. 2.2 the time-average potential experienced by the ion of mass m and charge q is given by

$$D = \frac{q}{m} \frac{U^2 r^2}{\omega^2 r_0^4}, \tag{2.5}$$

where $r^2 = x^2 + y^2$. Hence, the ion will behave as if confined in a parabolic "pseudo-potential" well, as shown in Fig. 2.2c.

A set of electrodes as shown in Fig. 2.2a operated with an oscillatory potential $\Phi = U \cdot f(\omega t)$ will provide radial confinement of ions. Such a system is commonly referred to as a radiofrequency quadrupole (RFQ) ion guide. Such ion guides are

commonly used to transport ions at low kinetic energies, and are particularly well-suited to the transport of ions through regions where a buffer gas may be present. By superimposing a potential well along the axis of the ion guide a 3-dimensional ion trap can be made. One means to form such an axial potential is by segmenting the structure, as shown in Fig. 2.3a, and applying the appropriate bias voltages to each section.

a)   b)
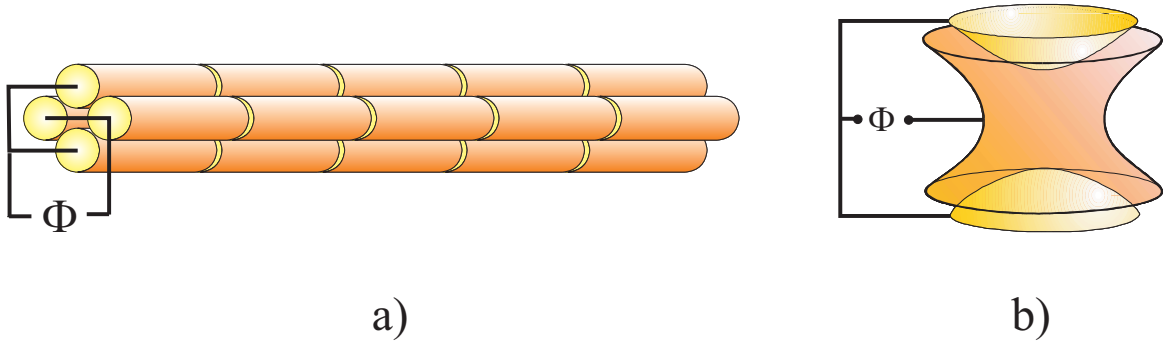
Figure 2.3. a) A segmented RFQ ion guide. Applying an RF potential $\Phi = U \cdot f(\omega t)$ can create transverse confinement. Properly biasing each RFQ section can create a 3-dimensional ion trap. b) Classical Paul trap. Applying a potential difference Φ between the endcaps and the ring produces an axially symmetric quadrupole field. Trapping can be achieved by modulating Φ with an oscillatory function.

On the other hand is possible to create an axially symmetric quadrupole field by using a hyperbolic ring and hyperbolic end caps. If an oscillatory potential difference is applied between the ring and end caps, 3-dimensional ion confinement can be achieved. Such a configuration, shown in Fig. 2.3b, is commonly referred to as the classical Paul trap [57]. As the classical Paul trap is not germane to the content of this thesis, and its operation and behavior analogous to that of the linear Paul trap, no further discussion of it will be provided.

2.1.1 Stability of Ion Motion in an RFQ Ion Guide

Ions in a Paul trap or RFQ ion guide travel along a complicated trajectory that consists of oscillations in the pseudo-potential well at the secular frequency, modulated by a micro-motion at the frequency of the applied RF potential U_{RF}. Depending on the relative amplitudes and frequencies of these motions, the trajectories will be stable and the ion remain trapped indefinitely or unstable, resulting in ion loss.

The action of the RFQ ion guide can be explained by analogy with a focusing-defocusing (FoDo) beam transport system. As the name suggests, in a FoDo beam transport system an ion beam is alternately focused and defocused during transport. When the beam is focused along one plane, it is defocused along the other. In a FoDo system, the focus and defocus are separated by fixed distances, while in an RFQ they are separated by fixed time durations. A standard FoDo system, where short focusing elements are separated by stretches where the ion beam drifts, is analogous to an RFQ ion guide operated with $f(\omega t)$ given by a three-state (positive-zero-negative) pulse train.

Consider a series of static quadrupole elements with equal strength, as shown in Fig. 2.4. In the case of an isochronous ensemble of ions, where all ions have the same velocity regardless of mass, this is analogous to the RFQ ion guide with $f(\omega t)$ given by a square wave.

As the focal length is dependent on the ion's energy, lighter ions will have a shorter focal length than heavier ions. For a given quadrupole strength, sufficiently light ions will have a focal length shorter than the focal element, as in Fig. 2.4a. In this way, a low mass cut-off exists.

Now suppose that the defocussing elements are stronger than the focusing elements. This is equivalent to an RFQ ion guide operated with $\Phi = V_{DC} + U_{RF} \cdot f(\omega t)$, *i.e.* an additional static quadrupole potential is added to the system. In this case there exist three possible scenarios for ions of a given mass. In the first scenario,

the focal length is too short and the ions are lost (2.4a). In the second scenario, the focal length is too long, the ion envelope increases with each cycle until the ions are lost (2.4b). This results in a heavy mass cut. The third scenario is the Goldilocks scenario, where the balance between focusing and defocussing is just right and the ion is not lost (2.4c). Depending on the relative strength of focusing elements compared with the defocusing elements, this balance can be precarious.
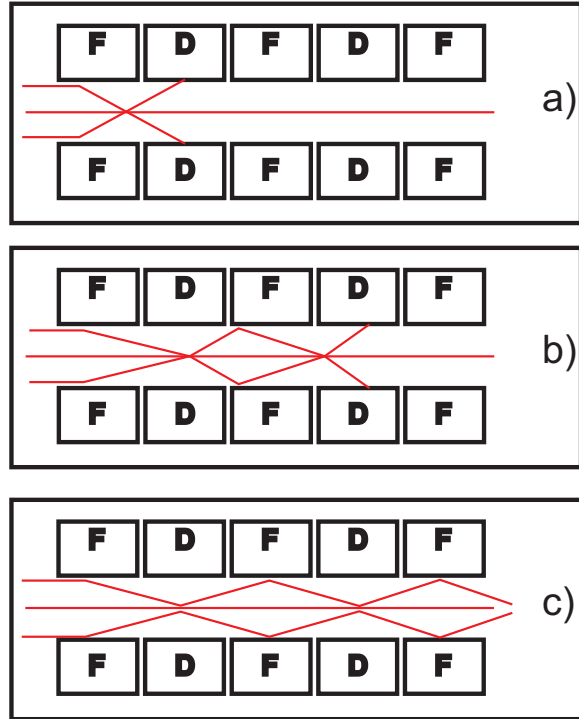
Figure 2.4. Focusing-Defocusing transport system analogous to RFQ ion guide operated with $f(\omega t)$ given by a square wave. The beam travels from left to right and the envelope of the beam is indicated by the thin lines. a) Overfocusing system. b) Underfocusing system. c) System with sufficient balance between focus and defocus.

Criteria for stable trajectories in the RFQ ion guide can be quantified in a stability diagram. However, it is important to more formally consider motion of an ion in the RFQ ion guide first.

If the potential difference between adjacent rods is given by $\Phi = V - U \cdot cos(\omega t)$, then from eq. 2.4 the equations of motion are

$$\ddot{z} = 0 \tag{2.6}$$

$$\ddot{x} + \frac{e}{mr_0^2}(V - U \cdot \cos \omega t)x = 0 \tag{2.7}$$

$$\ddot{y} - \frac{e}{mr_0^2}(V - U \cdot \cos \omega t)y = 0 \tag{2.8}$$

Introduction of the so-called Mathieu parameters,

$$a_x = -a_y = \frac{4eV}{m\omega^2 r_0^2} \tag{2.9}$$

$$q_x = -q_y = \frac{2eU}{m\omega^2 r_0^2} \tag{2.10}$$

$$\omega t = 2\eta, \tag{2.11}$$

reduces eqs. 2.7 and 2.8 to the well-known Mathieu equation [58, 59],

$$\frac{d^2u}{d\eta^2} + [a_u - 2q_u \cos 2(\eta - \eta_0)]u = 0, \tag{2.12}$$

where u represents either x or y and η_0 accounts for the initial phase when the ion enters the RF-field. The Mathieu equation allows solutions of four types: trivial, oscillatory, exponentially increasing and exponentially increasing oscillatory. The solution type depends on the values of the parameters a and q.

For values of a and q providing oscillatory solutions, the ion trajectory will be stable provided the amplitude of oscillation is not greater than the inter-electrode separation, while values of a and q providing exponential solutions will result in ion loss. The boundary between these two solution types is given by the Mathieu functions of integral order.
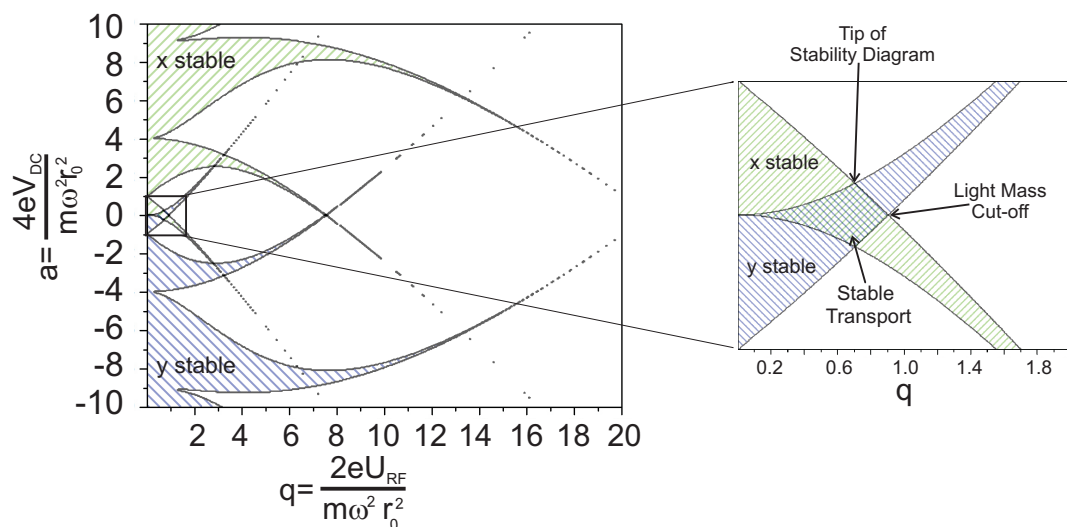
Figure 2.5. Diagram in Mathieu parameter space (a, q) where stable $x-$ and $y-$trajectories exist. The expanded region details the primary region in Mathieu parameter space with both stable $x-$ and $y-$trajectories, where stable ion transport occurs.

Figure 2.5 shows the (a,q) space with stable trajectories in the $x-$ and $y-$directions. In the region where the x and y stability diagrams overlap, ion trajectories are stable in the $x - y$ plane. The region of overlap which includes $(a,q) = (0,0)$ is known as the first stable region; throughout this thesis we will refer to its boundaries simply as the "stability diagram."

The ion guide stability diagram has a number of features which should be pointed out. The first is the low-mass cut-off at q=0.906, beyond which trajectories are instable even in the absence of any DC quadrupole component. The second is the tip of the stability diagram, occurring at (a,q)=(0.237,0.706). When operated near this point, the ion guide becomes highly mass selective [60]. This will be discussed in more detail in the next section.

As the stability diagram is symmetric with respect to the sign of a, it is common to show only the range of positive a-values, as shown in Fig. 2.6. The scan line,

21

which will be discussed again in the next section, is the path through the stability diagram that is traced when the RF and DC amplitudes, U_{RF} and V_{DC}, are scanned while their ratio is held constant.
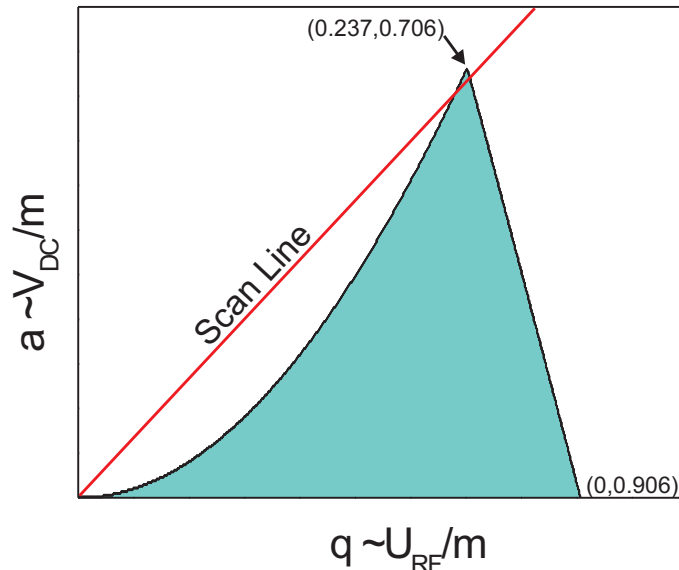
Figure 2.6. Stability diagram for ions in an RF quadrupole ion guide. The low-mass cut occurs at q=0.906 while the tip of the stability diagram occurs at $(a, q) = (0.237, 0.706)$. The scan line is the path traced through the stability when the RF and DC amplitudes are scanned and their ratio is held constant. By convention, the stability is generally shown within the range of positive a-values due to its reflection symmetry about a=0.

2.1.2 RFQ Mass Filter

When the RFQ ion guide is operated near the top of the stability diagram (see Fig. 2.6), it functions as a band-pass mass filter. This is shown in Fig. 2.7, where the stability diagram is drawn in (V_{DC}, U_{RF}) space for an incremental series of ion masses. Clearly, with the proper choice of U_{RF} and V_{DC}, only ions with a specific mass will

be transported. This mass filter function is used in the LEBIT facility and is one of the keys to being able to perform Penning trap mass measurements.
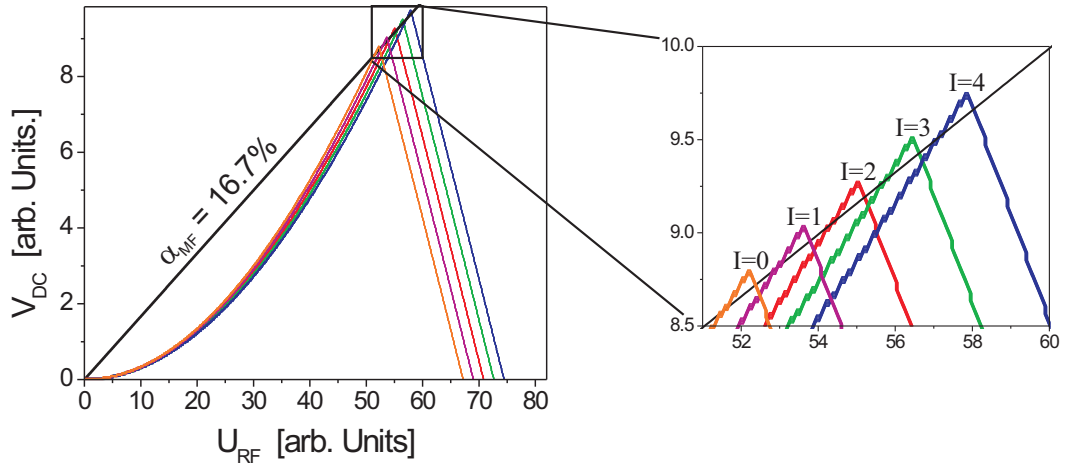
Figure 2.7. Stablity diagrams plotted in voltage space (V_{DC},U_{RF}) for a series of ions with incremental mass numbers, A+I, in the sinusoidally operated radiofrequency ion guide. The scan line given is for $\alpha_{MF} = 16.7\%$. The expanded region makes clear that when operated on this scan line, the mass filter will transport only one mass number at a time. The jagged shaped seen in expanded region is an artifice.

The mass filter operates at a constant resolution determined by the scan line. Throughout this thesis, scan lines will be identified by the ratio $\alpha_{MF} = \frac{V_{RF}}{U_{DC}}$, expressed as a percentage. The top of the stability diagram lies on the scan line $\alpha_{MF} = 16.78\%$. The resolution of the mass filter can be defined by the width of the range of masses which can be transported. Suppose the mass filter is operated at a given (V_{DC},U_{RF}) where ions with mass A±1 are transported with half the efficiency of ions with mass A. Under such conditions the mass filter resolution would be 2 u; the resolution would be the same at any point on the scan line connecting (0,0) and (V_{DC},U_{RF}).

As Fig. 2.7 shows, in order to achieve single mass unit resolution, the RFQ mass filter must be operated near the upper limit of the stability diagram. In order to

acheive this resolution, the frequency, RF and DC amplitudes all need to be stable to better than the 1% level. How this is achieved will be discussed in greater detail in chapter 5.1. As a practical matter, most RFQ ion guides are constructed using cylindrical rods. While this results in an approximation of the proper hyperbolic field, it is sufficient as long as r is small compared to r_0. It has been pointed out [61] that a misalignment of the rods by less than 1°, deviation in thickness along the length of the rods of as little of 1% and even small patches of oil, water or other non-conducting material can result in far larger field imperfections.

2.1.3 Ion Cooling and Bunching with RFQ Ion Guides and Traps

Ion cooling and bunching is important for performing high-precision measurements with trapped ions. In general ion cooling is used to reduce the emittance of ion beams, often with the goal of matching the emittance to the acceptance of subsequent devices. Bunching is a technique which converts a continuous beam of ions into a pulse; this is, for example, important for the efficient capture of ions in a Penning trap.

Beam Cooling

Liouville's theorem says that the phase space volume of an ion ensemble cannot be changed through conservative forces. This means that while electromagnetic lenses may be used to focus a beam, they cannot alter the beam emittance. Interaction with a buffer gas, however, constitutes a non-conservative force and provides a means to reduce the phase space volume.

The collisions occurring between an energetic ion and a buffer gas will tend to thermalize the velocity of the ion. If the buffer gas is lighter than the ion then the transfer of energy will be more efficient. Nonetheless, the ion needs to be confined due the random nature of the collisions.

When an ion undergoes a collision with a significantly more massive buffer gas atom, the change in the ion's momentum can be large. Depending on the phase of the RF and the magnitude of the momentum change, it is possible for the ion to gain energy from the RF field. This so-called RF heating [62] can lead to ion loss.

Optimal cooling requires that the buffer gas be chosen well. In order to avoid charge exchange between the ion and the buffer gas atoms requires a buffer gas with high ionization energy, such as a noble gas. The mass of the buffer gas atom should be considerably smaller than that of the ion in order to avoid RF heating. For these reasons, helium is the most commonly used buffer gas. The presence of molecular isobars in the beam, however, may necessitate the use a heavier buffer gas as will be discussed in chapter 5.

Ion interactions with a buffer gas can be modeled as a series of elastic collisions [63]. As discussed above, quite often the buffer gas is very light compared to ions, resulting in minimal ion recoil. Under such conditions, the ion-atom interaction can be approximated by a viscous force

$$\vec{F} = -q \frac{P}{1013 \cdot K_0} \cdot \vec{v}, \tag{2.13}$$

where q is the ion charge, P is the pressure in mbar, $\vec{v}$ is the ion velocity and K_0 is the reduced ion mobility, which determines the drift velocity of an ion through a buffer gas in a uniform electric field.

Using the viscous drag approximation, it is easy to visualize the ions performing a damped harmonic motion in the harmonic radial pseudo-potential well present in a linear quadrupole ion guide. In this way, ion cooling reduces the radial amplitude (and emittance) of an ion beam. In much the same way, the axial motion will be damped and the ion may come to rest. To prevent this, an axial drift field can be applied by, *e.g.* segmenting the ion guide as shown in Figs. 2.3 and 2.8.
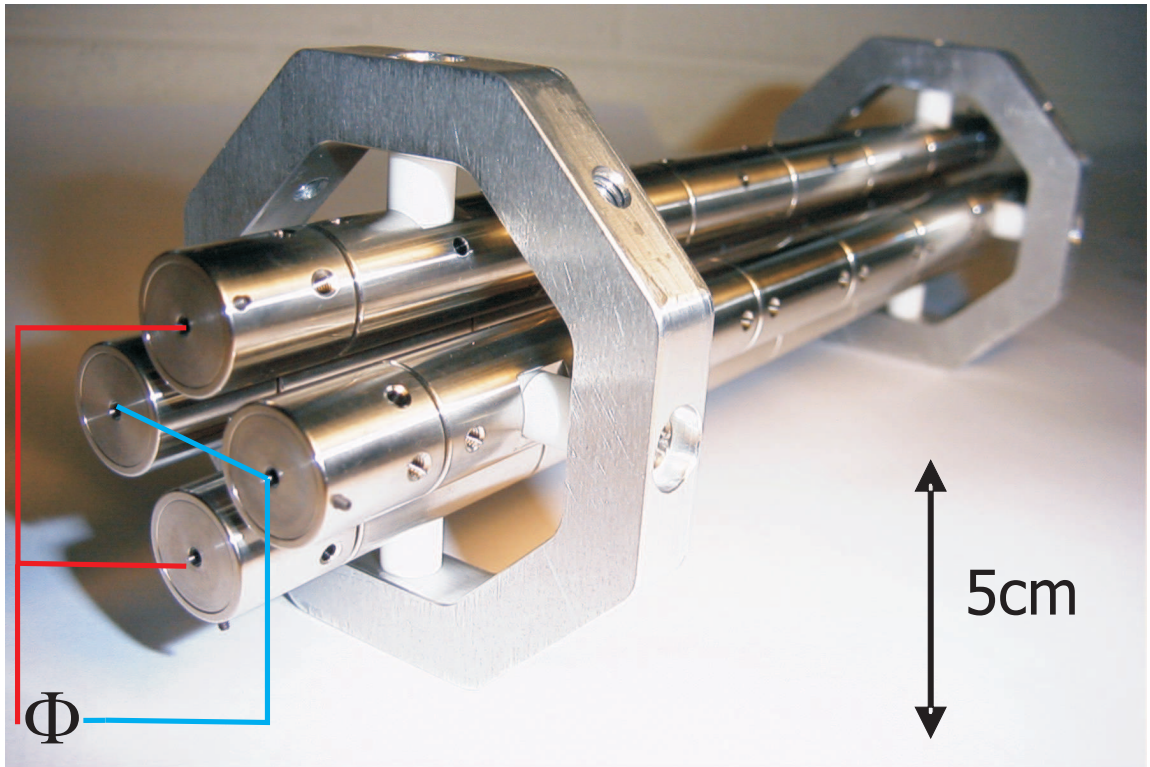
Figure 2.8. Photograph of a segmented RFQ ion guide.

Ion Bunching

If the (axial) potential applied to the segments of an RFQ ion guide such as shown in Fig. 2.8 are properly chosen, a linear RFQ ion trap can be created. To do this, the segments are biased such that a potential well is formed along the axis. If the trap is filled with a buffer gas, such a device can be used to cool, accumulate and bunch and incoming ion beam. Figure 2.9 provides a schematic representation of such a bunching technique. If the potential at the front of the well is chosen to exceed the energy of the ions after one oscillation of the system (see Fig. 2.9) the ions will perform a damped oscillatory motion and accumulate in the axial potential well, eventually equilibrating at the buffer gas temperature.

Once the ions have cooled, the voltages applied to the segments can be quickly changed to allow the ions to leave the trap as a pulse. This allows for a continuous

beam to be converted into a pulsed beam with well defined axial energy and low emittance. The operation of such a device, which is used at LEBIT, will be further discussed in chapters 3 and 5.
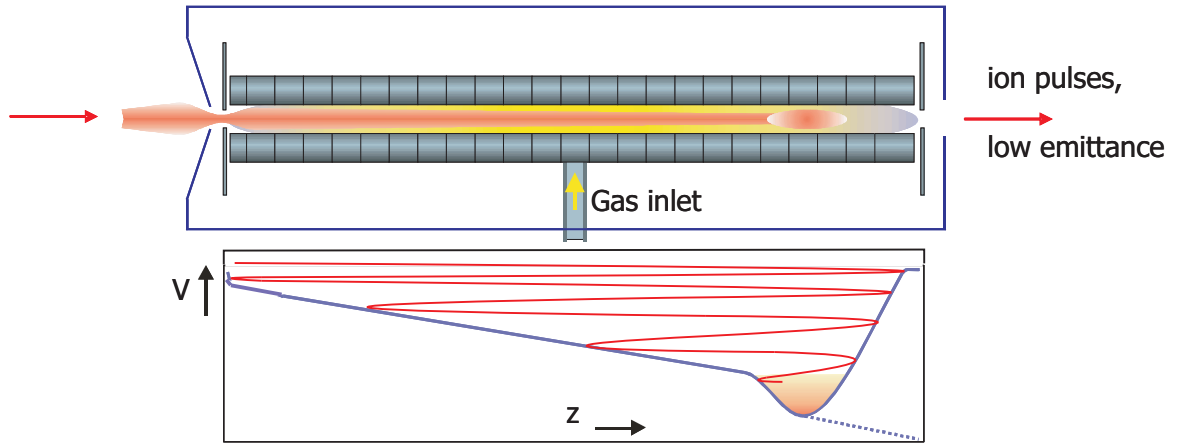
Figure 2.9. Schematic representation of the use of a linear RFQ ion trap to accumulate, cool and bunch an ion beam. The segmented rods of a linear RFQ system (top) are biased to create a potential well (bottom, solid line). Ions entering the trap loose energy in collisions with the buffer gas and decay to the bottom of the potential well. Once ions have been cooled, the potential can be switched to eject ions as a pulse (dashed line).

2.2 Ion Confinement with Combined Electric and Magnetic Fields

The Penning trap uses an homogeneous axial magnetic field superimposed upon a static quadrupole electric field to confine ions 3-dimensionally. Fig. 2.10 illustrates a hyperbolic Penning trap, for which the electrodes form an equipotential surface of an axially symmetric quadrupole potential.
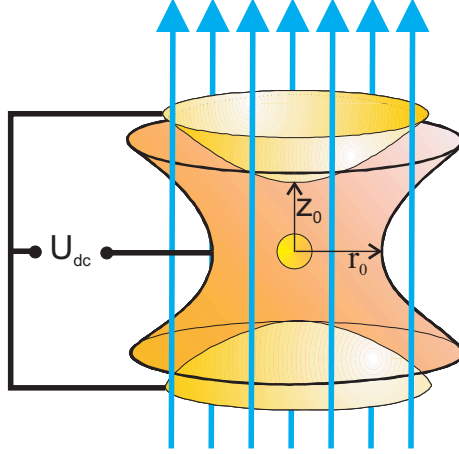
Figure 2.10. Sketch of a hyperbolic Penning trap. The magnetic field provides radial confinement while a static electric field, created by a voltage, U_{DC}, applied between a pair of endcaps and a ring electrode, provides axial confinement.

2.2.1 Ion Motion in a Penning Trap

An ion with mass m and charge q in a homogeneous magnetic field will perform circular motion with a frequency

$$\omega_c = \frac{q}{m} B, \tag{2.14}$$

referred to as the cyclotron frequency. In a Penning trap this motion is modified due to the presence of the electric quadrupole field, resulting in three eigenmotions.

In the axial direction, the quadrupole potential

$$\phi = \frac{U_{DC}}{4d^2} (2z^2 - r^2) \tag{2.15}$$

gives rise to a harmonic force $F_z = q \cdot E_z = -\frac{qU_{DC}}{d^2} z$. This leads to an axial oscillation with frequency

$$\omega_z = \sqrt{\frac{qU_{DC}}{md^2}}, \tag{2.16}$$

where $d = \sqrt{\frac{1}{4}r_0^2 + \frac{1}{2}z_0^2}$ (see Fig. 2.10).

In the radial direction the force $F_r = q \cdot E_r = \frac{qU_{DC}}{2d^2} r$ points toward the ring electrode. This results in two radial eigenmotions. One is an $\vec{E} \times \vec{B}$ drift motion, called

28

the magnetron motion, with frequency ω_-. The other is a fast cyclotron oscillation with frequency ω_+. The three eigenmotions are illustrated in Fig. 2.11.

In the case of a pure quadrupole electric field, the radial eigenmotions are given by [64]

$$\omega_\pm = \frac{\omega_c}{2} \pm \sqrt{\frac{\omega_c^2}{4} - \frac{\omega_z^2}{2}} \tag{2.17}$$

Important relations between these eigenfrequencies are: $\omega_+ + \omega_- = \omega_c$ and $\omega_+ \approx \omega_c$. In a strong magnetic field ($B > 4$ T) with light ions ($m_{ion} \lesssim 1000$ u) and trapping potential $U_{DC} > 10$ V, the eigenfrequencies can be ordered $\omega_- \ll \omega_z \ll \omega_+$. For a Penning trap with B $\approx$ 9 T and d $\approx$ 10 mm, with U $\approx$ 10 V the eigenfrequencies are $\nu_- \approx 1$ kHz, $\nu_z \approx 100$ kHz, $\nu_+ \approx 1$ MHz for A $\approx$100.
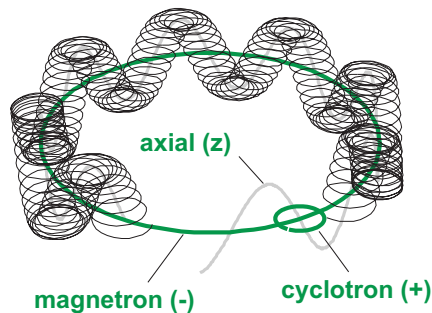
Figure 2.11. Illustration of ion motion in a Penning trap. There are two radial motions - magnetron (ω_-) and modified cyclotron (ω_+) oscillations - as well as an axial (ω_z) oscillation.

2.2.2 Excitation of Ion Motions in a Penning Trap

An ion's radial eigenmotions can be excited by means of azimuthal multipolar RF electric fields. These multipolar fields are generally achieved by segmenting the hyperbolic ring electrode and applying RF signals such that the potentials applied to adjacent electrodes are 180° out of phase. Using $N = 2^n$ hyperbolic ring segments results in an azimuthal n-pole field capable of exciting the radial eigenmotions at

frequencies equal to the sum of $\frac{1}{2}N$ radial eigenfrequencies [65].

A dipole field (ring electrode divided in two segments) can drive one of the radial eigenmotions. When a dipole RF electric field is applied at frequency ω_- or ω_+ either the magnetron or cyclotron motion is excited, increasing the amplitude of the relevant eigenmotion linearly with time. Dipolar excitation at ω_- is commonly used to place trapped ions into a magnetron orbit in preparation for mass measurements. Dipolar excitation at ω_+ can be used to mass-selectively remove ions from the trap.

A quadrupole field (ring electrode divided in four segments) can drive the eigenmotions at $2\omega_-$, $2\omega_+$ or $\omega_-+\omega_+$. In the case of $\omega_-+\omega_+$ the magnetron and cyclotron motions are coupled, leading to a periodic beating between both motions [65, 66]. The use of quadrupolar excitation at the true cyclotron frequency to perform mass measurements will be described in the following section.

2.2.3 Penning Trap Mass Spectrometry

The basis of Penning trap mass spectrometry (PTMS) is the determination of the ion cyclotron frequency, $\nu_c = \frac{q}{2\pi m} \cdot B$. In order to derive the mass from ν_c two other quantities must be known - the ion's charge state and the magnetic field strength. The charge state is generally a known small integer, most often 1+ or 2+. The magnetic field strength, however, must be measured. This is accomplished by measuring the cyclotron frequency of a reference ion with well-known mass.

Several techniques exist for determining the ion cyclotron frequency. A commonly used technique for determining ω_c of short-lived isotopes is the time-of-flight ion cyclotron resonance (TOF-ICR) technique [66, 67, 68]. This technique involves the measurement of the time-of-flight of ions ejected from the trap after being subjected to an azimuthal RF field.

As previously mentioned, an azimuthal quadrupole RF field can couple an ion's radial eigenmotions. When a trapped ion is subjected to an azimuthal quadrupole
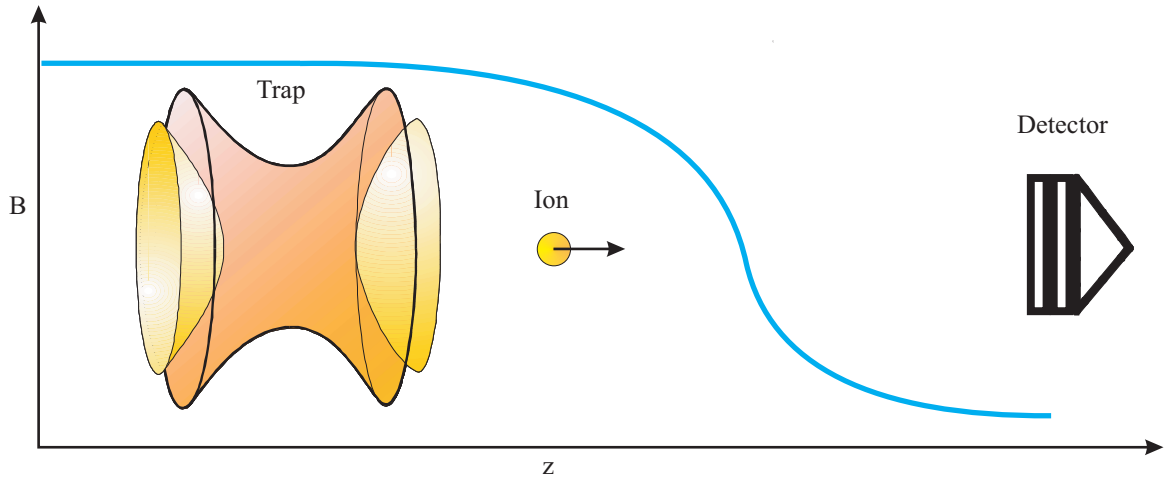
Figure 2.12. Ions performing cyclotron motion, caused by RF excitation in the trap, will have a larger radial energy than ions whose motion is not excited. When the ions are ejected from the trap and pass through the inhomogeneous portion of the magnetic field outside of the Penning trap, radial energy is converted into axial energy. This reduces their time of flight to an ion detector.

RF-field with frequency $\nu_{RF} \approx \nu_c$, there is a periodic conversion between magnetron motion and reduced cyclotron motion. For a given excitation time, T_{RF}, there is an RF amplitude V_{RF} such that the magnetron motion is completely converted into reduced cyclotron motion [65]. This conversion is accompanied by an increase in radial energy and will be maximized when $\nu_{RF} = \nu_c$.

In order to detect this increase in energy, the ion can be ejected from the trap. When the ion passes through the inhomogeneous magnetic field (see Fig. 2.12) radial energy is converted into axial energy. Therefore the larger the radial energy of the ion, the shorter the time of flight to a detector. This is used in the time-of-flight cyclotron resonance detection method used at LEBIT to determine an ion's cyclotron frequency.

Plotting the mean time of flight, from the trap to a detector, of the ejected ions as a function of excitation frequency, ν_{RF} yields a cyclotron resonance curve, as shown in Fig. 2.13. The frequency corresponding to the time-of-flight minimum is the

cyclotron frequency of the species of interest. The lineshape for such a curve has been analytically determined [66].
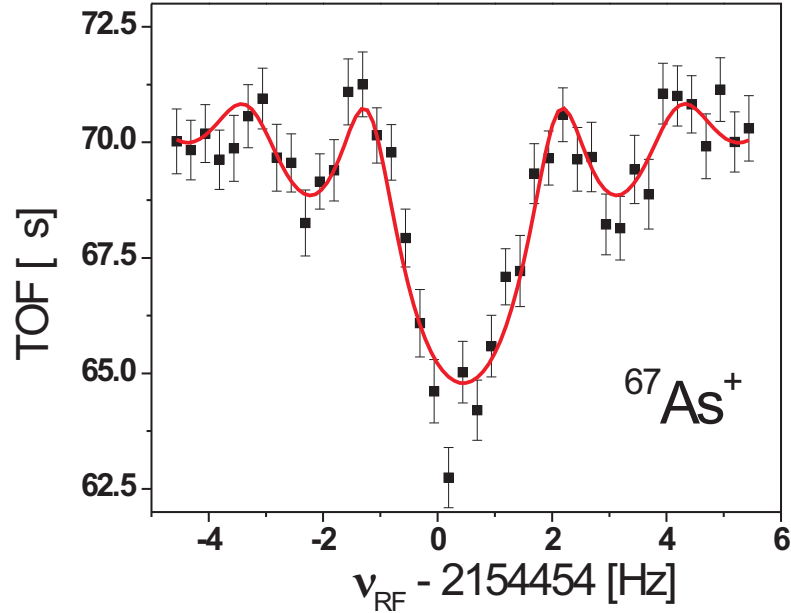
Figure 2.13. Cyclotron resonance curve for ^{67}As$^+$ (T$_{1/2}$ = 42.5 s) measured at LEBIT in this work. Plotted is the mean time-of-flight versus excitation frequency, ν_{RF}. The solid red line is a fit to the data of an analytic lineshape [66] .

The resolving power of a spectrometer is a measure of how well nearby masses can be distinguished. The resolving power of a Penning trap mass spectrometer is given by

$$R = \frac{m}{\Delta m} = \frac{\nu_c}{\Delta \nu_{FWHM}} \tag{2.18}$$

where $\Delta \nu_{FWHM}$ is the line-width of the frequency determination for ν_c. For a given observation time, T_{ex}, the line-width is Fourier limited to $\Delta \nu \approx \frac{1}{T_{ex}}$. The resolving power of a Penning trap mass spectrometer, therefore, is determined by the observa-

tion time, T_{ex}, and is given by

$$R = \frac{\nu_c}{\Delta \nu_c} \approx T_{ex} \cdot \nu_c \tag{2.19}$$

As an example, ^{81}Se, recently studied at LEBIT [69], has an isomeric state which differs in mass from the ground state by ≈ 2 ppm. In order to distinguish both states, a resolving power of $> 500{,}000$ would be required. The cyclotron frequency of ^{81}Se in a 9.4 T field is about $\nu_c \approx 1$ MHz. In order to separate ground and isomeric states would require an observation time of at least 500 ms.

The statistical precision which can be achieved with PTMS has been estimated [70] as

$$\frac{\delta m}{m} \approx \frac{k}{R \cdot \sqrt{N}} = \frac{k}{\nu_c} \cdot \frac{1}{T_{ex}\sqrt{N}} \tag{2.20}$$

where N is the number of detected ions and k is typically close to unity, but depends on the actual detection method. For measurements of sufficiently long-lived species, precision can be increased simply by extending the observation time - a feature not available in most other techniques.

CHAPTER 3

The LEBIT Facility

The Low Energy Beam and Ion Trap (LEBIT) facility at the NSCL converts the beam of rare isotope ions produced at relativistic energies by in-flight separation of heavy projectile fragments into a low energy beam. To achieve this, gas stopping and advanced beam manipulation techniques are used. The facility's first experimental apparatus is a 9.4 T Penning trap mass spectrometer for performing high-precision mass measurements on short-lived isotopes. Laser spectroscopy and decay study experiments, as well as possible post-acceleration, are additional options currently under consideration at the NSCL.
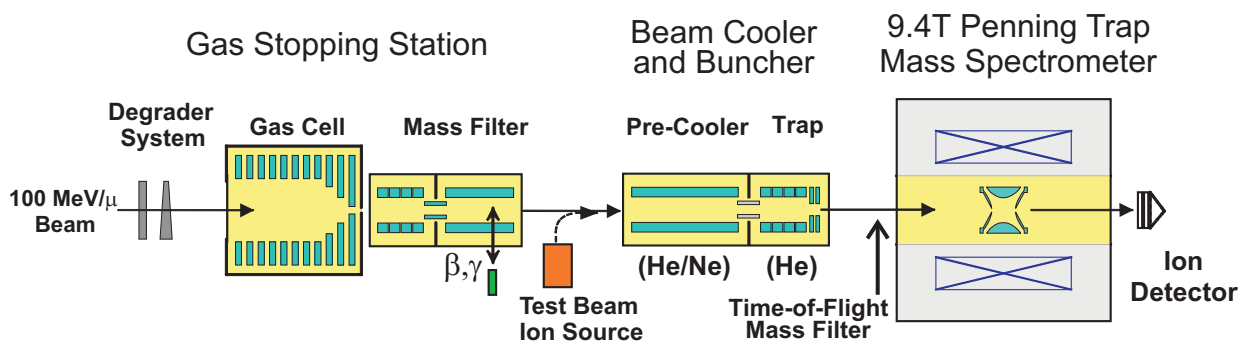
Figure 3.1. Schematic overview of the LEBIT facility at the NSCL

34

3.1 LEBIT Facility Overview

Figure 3.1 provides a schematic overview of the major components of the LEBIT facility. These components are a gas stopping station, a beam cooler-and-buncher, and a Penning trap mass spectrometer. The components are connected by electrostatic beam transport systems. For beam diagnostics, a suite of beam monitors (not shown in Fig. 3.1) are installed along the beamline.

Relativistic ions delivered from the A1900 fragment separator [43] are slowed in a degrader system, where most of their energy is dissipated, before passing through a beryllium window and entering the gas cell. Inside the gas cell, the ions lose their remaining energy via collisions with helium buffer gas near atmospheric pressure. Once thermalized, the ions are drawn to an extraction nozzle at the end of the gas cell by means of a static electric field. In the extraction nozzle, gas flow becomes a dominant force, sweeping the ions out of the gas cell in a super-sonic gas jet.

Ions extracted from the gas cell are carried through a differential pumping system into ultra-high vacuum by a series of radio-frequency quadrupole (RFQ) ion guides. Upon reaching the end of the ion guide system, the ions are accelerated to 5 keV/q.

The ion beam cooler-and-buncher system consists of two main sections. The first section is an RFQ ion guide filled with a buffer gas of helium or neon at $\approx 10^{-2}$ mbar. As ions pass through the cooler, buffer gas collisions cool the ions. After this initial cooling, the ions are guided into the second section, an RFQ ion trap filled with helium buffer gas at $\approx 10^{-4}$ mbar. After being held in the trap long enough to come into thermal equilibrium with the buffer gas, the ions can be ejected as short pulses.

Ions ejected from the buncher are accelerated to 2 keV/q and electrostatically transported to the Penning trap. In this beam transport line the ions pass a time-of-flight mass separator, realized with a fast pulsed beam deflector.

After passing the time-of-flight mass filter, ions are captured by a Penning trap in a 9.4 T magnet. Ion masses can then be measured through determination of the

true cyclotron frequency by means of the time-of-flight resonance detection method, discussed in chapters 2.

3.2   Gas Stopping Station

Relativistic beams of 80-150 MeV/u are delivered to the gas stopping station from the A1900 fragment separator and converted into low energy beams. As shown in Fig. 3.1, the gas stopping station consists of three major components: degrader system, gas cell and ion guide system.

The degrader system consists of glass plates and a glass wedge. The glass plates are parallel to 1 μm and can be rotated to adjust their effective thickness, allowing control over how far inside the gas cell the ions come to rest. The glass wedge is placed at a point in the beam line with a horizontal momentum dispersion to compensate for the momentum spread [71] of the ions coming from the A1900. This reduces the range distribution of the ions in the gas to the limit produced by range straggling and non-uniformities in the degraders.

The gas cell, shown in schematic detail in Fig. 3.2, is a 50 cm long vacuum chamber which can be filled with helium gas to a pressure of 200 - 1000 mbar. The gas cell is sealed on the entrance side of the gas cell by a thin (0.566 mm) beryllium window. Inside of the gas cell, 21 ring electrodes are used to create a static electric field to drag the stopped ions through the gas. In addition to the ring electrodes, four spherical electrodes are used to approximate the electric field of a point charge near the extraction region of the gas cell, thus focussing ions into the opening of the extraction nozzle.

In order to reduce the number of power supplies and operational parameters required to create an electric field along the axis of the cell, the ring electrodes are resistively connected in-vacuo. The third ring electrode, counting from the beryl-

lium window, is not part of a resistive chain. This allows for independent biasing of that electrode for use as a charge collector, which provides a tool for monitoring the ionization produced inside the gas cell.
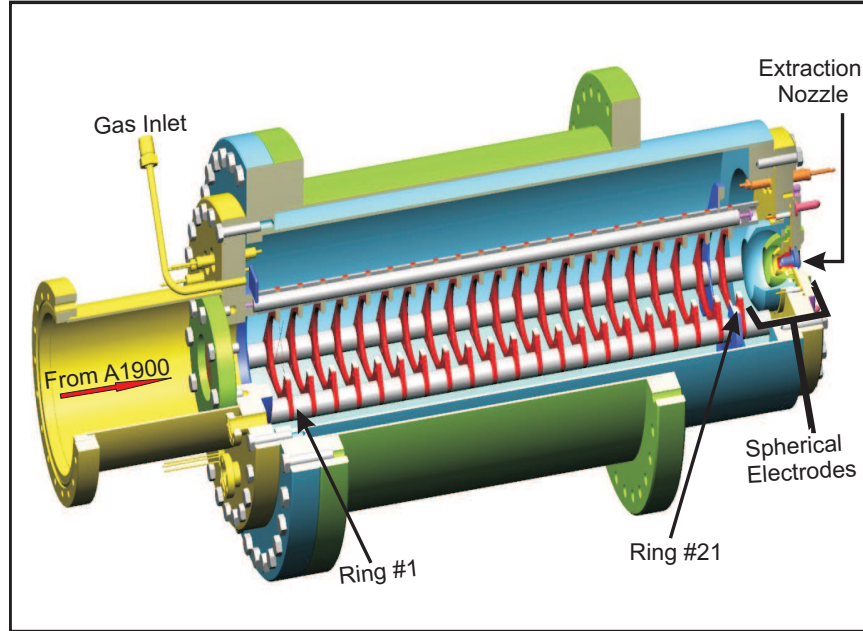
Figure 3.2. Mechanical drawing of the gas cell. The ring electrodes are connected in a pair of resistive chains (not shown) connected in-vacuo.

The shape of the extraction nozzle was designed such that the gas forms a supersonic jet when entering the chamber following the gas cell, thus reducing turbulent flow which could result in ion loss. The use of a semi-conducting material allows for the application of an electric field inside the nozzle, which helps to guide the ions toward the nozzle apex. Near the nozzle apex, gas flow becomes the dominant force, transporting the ions into the next chamber in the flow of a supersonic gas jet.

Studies of the stopping and extraction of relativistic radio-isotope ions with the LEBIT gas stopping cell was the focus of the PhD. thesis of Patrick Lofy in 2004 [72]. Details of stopping and extraction of relativistic ions from the LEBIT gas stopping cell under various conditions can also be found in [73, 74, 75].

Within this thesis work, a number of simulations of ion transport in the gas cell were performed during the initial design period. These simulations included feasibility studies for the use of electrostatic transport and extraction from the gas cell. Details of these simulations will be given in chapter 4.

As described above, the ions are extracted from the gas cell in a super-sonic gas jet. The ions are transported into high-vacuum through series of radiofrequency quadrupole (RFQ) ion guides which carry them downstream through a series of differentially pumped vacuum chambers. This is important as high-vacuum conditions are required for fast and efficient ion transport to the following LEBIT components.

The ion guide system is composed of three functional sections. The first section is a segmented RFQ ion guide, allowing for superposition of an electrostatic field to drag the extracted ions through the residual helium gas, which is viscous in this region where the pressure can be as high as 0.1 mbar. The second section is a small RFQ ion guide (μRFQ) which provides efficient transport through a small orifice for differential pumping. The third RFQ section has been designed to operate as a high efficiency mass filter. After passing the mass filter, the ions are accelerated to 5 keV/q for further transport. This ion guide system will be described in greater detail in chapter 5.1.

3.3 Beam Transport from the Gas Cell to the Beam Cooler

After the gas stopping station, the ion are accelerated to 5 keV/q and transported to the beam cooler-and-buncher system through a series of einzel lenses. A schematic representation of the 5 kV beam transport system is given in Fig. 3.3. Inside the dashed box, the beam line is biased at -5 kV to allow the gas cell to be on ground potential.
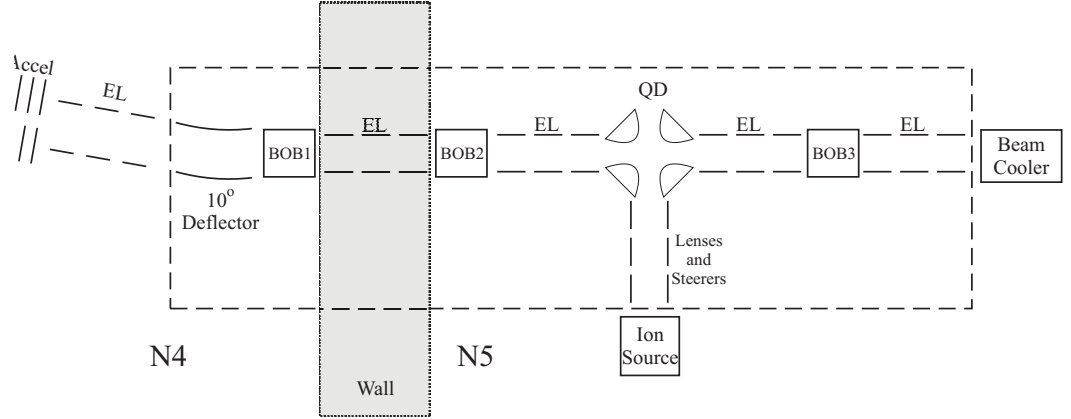
Figure 3.3. Schematic representation of the beam transport system to carry ions from the ion guides to the beam cooler. "EL" designates einzel lenses while "BOB" designates beam observation boxes. The quadrupole deflector is designated "QD". Inside the dashed box, the beamline is floated on the transport potential of -5 kV.

The gas stopping station is located in a separate experimental vault (referred to as N4) from the rest of the LEBIT facility (located in N5). There is a 10° angle between the beam lines in N4 and N5. A spherical electrostatic deflector in the 5 kV transport system is used to correct for this. This deflector is also used as an electric beam gate. One of the deflector electrodes is connected to a fast high-voltage switch which nominally supplies a voltage such that ions are not transmitted through the deflector; when triggered, the switch output swings by ≈1 kV, allowing ion transport. The switch, described in Appendix D.4, is capable of pulse lengths from <500 ns - ∞. This allows for control over how many ions are accumulated in the buncher at one time.

The 5 kV transport line includes a set of three beam observation boxes (BOBs) containing beam diagnostic elements. Each BOB is equipped with a set of parallel plate beam steerers and an insertable Faraday cup. Additionally, BOB1 is equipped with a silicon surface-barrier (SSB) detector which can be inserted to measure the β-decay of rare isotope ions extracted from the gas cell. BOB2 is equipped with

a phosphor screen and BOB3 is equipped with a micro-channel plate (MCP) ion detector. The phosphor screen and MCP detector allow visualization of the beam profile. The MCP detector at BOB3 can additionally be used to measure time-of-flight spectra of ion pulses for mass identification of ions delivered from the gas stopping station. The MCP detector at BOB3 uses a fibre optic readout system which is described in Appendix D.5.

As shown in Figs. 3.1 and 3.3, a plasma ion source is installed perpendicular to the beam line. The ion source is a Colutron Model 100 [1] designed for providing noble gas ions; it is also capable of delivering alkali ions such as Na^+, K^+ and Rb^+ via thermal ionization of these elements which are present in the filament material of the source. The ion source is followed by a small RFQ mass filter. Following the mass filter, ions are accelerated to 5 keV/q. The ions then pass through a suite of electrodes - steerers and lenses - for transport onward. One of the steerer electrodes is utilized as a fast beam gate operated by means of a high voltage switch identical in design to that used implement the 10° deflector as a beam gate. This allow for control over how many ions are accumulated in the buncher at one time.

An electrostatic quadrupole deflector [76] (labeled QD in Fig. 3.3) can be operated in one of three modes, providing transport of ions from the gas cell to the Penning trap, the ion source to the Penning trap, or the ion source to the gas stopping station. The latter mode was used in tests of the ion guide system which are discussed in the next chapter.

3.4   Ion Beam Cooler-and-Buncher

Both the gas cell and ion source provide continuous beams of ions. The beam cooler-and-buncher [45] converts the continuous beams into pulses of cold ions with a low

---

[1]http://www.colutron.com/products/kit/kit.html#A1_2
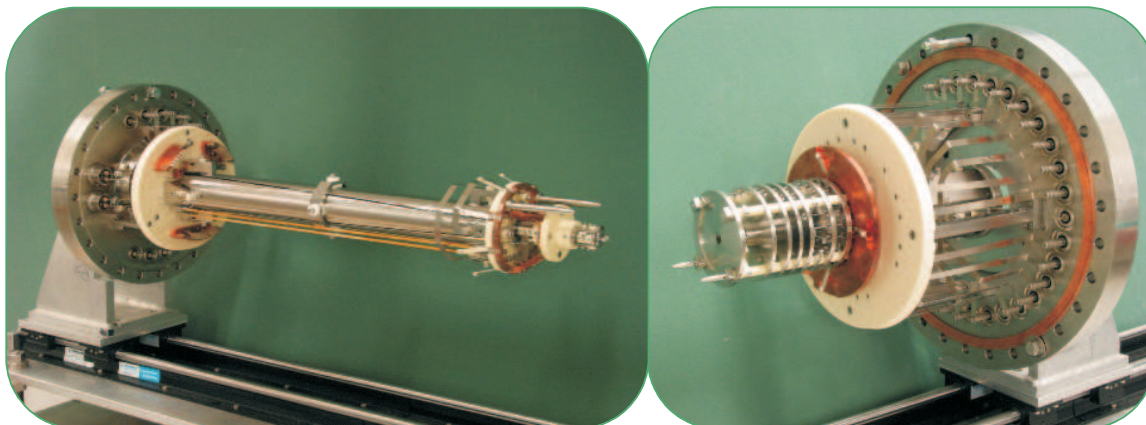
Figure 3.4. Photo of inner components of the beam cooler-and-buncher system. The photo on the left is the cooler with the μRFQ structure at the end. The photo on the right is the RFQ trap system.

emittance [76], greatly enhancing the efficiency of ion capture in the Penning trap. The system is composed of two separate components: a gas-filed RFQ ion guide acting as beam cooler and a gas-filled RFQ ion trap. The cooler is connected to the trap by a μRFQ identical to the one found in the gas stopping station ion guide system described earlier.

Ions enter the cooler and undergo collisions with the buffer gas, resulting in transverse cooling of the ions, as discussed in chapter 2.1.3. The cooled ions are then transferred to the trap where the ions are stored and undergo further collisions with the buffer gas, resulting in further transverse and longitudinal cooling. Once fully cooled, the ions are ejected from the trap and transported to the Penning trap.

For a buffer gas, the cooler uses either helium or neon, typically at a pressure of $\approx 10^{-2}$ mbar. To ensure that ions do not become "stuck" the buffer gas, electric fields are superimposed along the lengths of the cooler and μRFQ to drag the ions. These electrostatic fields are created using cylinders, cut into four wedges to make a pair of electrodes, which surround the RFQ rods [45].

The μRFQ provides a pumping barrier between the cooler and trap, allowing

the trap pressure to be regulated independently from the cooler. The trap is thus operated with helium as a buffer gas, typically at a pressure of $\approx 8 \times 10^{-4}$ mbar. The trap section consists of a series of disc electrodes which encircle an RFQ ion guide. Properly biasing each of the discs creates an electrostatic potential well along the axis of the ion guide. As described in chapter 2.1.3 ions are accumulated in the potential well and are cooled by collisions with helium buffer gas. Ion cooling in the trap occurs quickly, on the order of 10 ms.

After the ions accumulated in the trap have cooled, they are ejected by switching the electric potentials applied to the disc electrodes. The ejected ion pulse has a low emittance as well as small longitudinal energy spread, which is important for capture in the Penning trap. By using fast switches ($\tau_{rise} \approx \tau_{fall} <$100 ns) the quality of the pulse can be maintained while reducing the temporal duration of the pulse.

Figure 3.4 shows the assembled electrodes of the ion beam cooler-and-buncher. The wedged-cylinder electrodes providing the axial field in the cooler are clearly visible in the left photograph, with the μRFQ at the end of the cooler structure. The right image shows the buncher assembly. The disc electrodes used to form the trapping potential are visible.

The ion beam cooler-and-buncher vacuum chamber has a liquid nitrogen cryostat with thermal contacts to the electrode structure. This reduces the temperature of the buffer gas, improving the emittance of the ejected beam pulse while providing cryogenic pumping to minimize charge exchange losses. The impact of the cryogenic cooling on charge exchange is exemplified by the lifetime of triply charged Argon ions in the buncher, which has been measured to be $\approx$100 ms when using the cryogenic cooling and <20 ms without.

A second beam transport system connects the beam cooler-and-buncher to the Penning trap. This second transport system is operated at -2 kV and includes a pair of BOBs, referred to as BOB4 and BOB5. As in the 5 kV beam transport

system, einzel lenses are used for electrostatic transport. BOB5 is equipped with an MCP detector, similar to BOB3, which can provide time-of-flight mass spectra for identification of ions ejected from the buncher. The MCP detector at BOB5 use a fibre optic readout system which is described in Appendix D.5.

The beam steerer in BOB5 is used as a time-of-flight mass filter. The steerer is nominally operated at a potential sufficient to steer ions such that they are not captured in the Penning trap. At the appropriate time to allow passage of ions of the desired mass, the deflector voltage is switched to allow optimal transport. Details will be discussed in chapter 5.

3.5   Penning Trap Mass Spectrometer
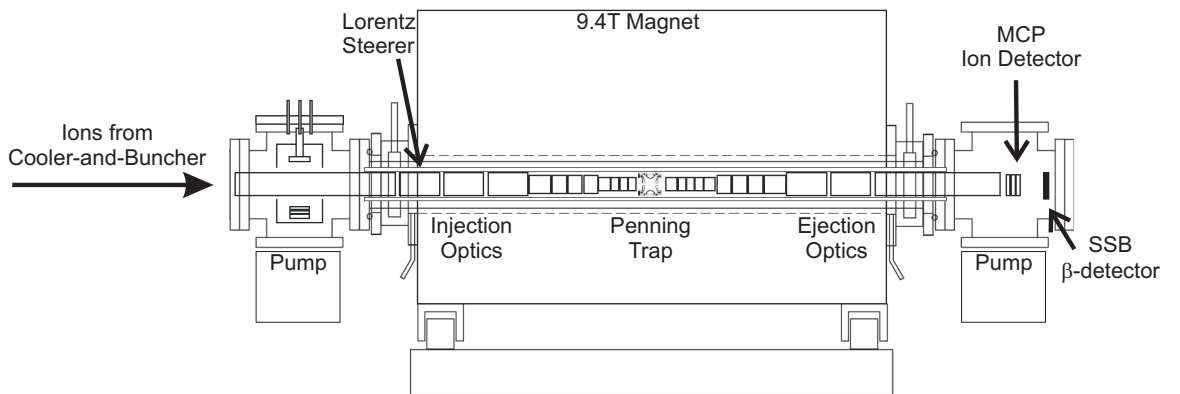
Figure 3.5. Schematic drawing of the LEBIT Penning trap mass spectrometer system.

Figure 3.5 shows a schematic drawing of the Penning trap mass spectrometer system implemented at LEBIT. The Penning trap electrode system is located in a region of ultra-high magnetic field homogeneity (±10 ppm within a 25 cm^2 $\times$ 10 cm cylinder) in a 9.4 T superconducting persistent solenoid magnet with a room-temperature bore. The magnet includes external-field compensation coils [77] to reduce the effect of external field changes that may occur in an accelerator environment. An aluminum

tube inserted into the magnet bore serves as both vacuum chamber and optical bench for the Penning trap and associated injection and ejection optics. A copper wire is wound about the aluminum tube, providing a means to bake the vacuum chamber as well as the ability to counteract the natural decay of the magnetic field during measurements.

After the final einzel lens in the -2 kV beam transport system, a series of drift tubes transport the ions into and out of the Penning trap. The first injection drift tube is implemented as a "Lorentz" steerer [78]. The tube is quartered and operated so as to produce an electric dipole field. Being located inside the strong magnetic field, this results in an $\vec{E} \times \vec{B}$ force on a passing ion, resulting in off-center injection into the Penning trap. This off-center injection provides an initial magnetron orbit and prevents the need to use valuable measurement time on magnetron excitation.
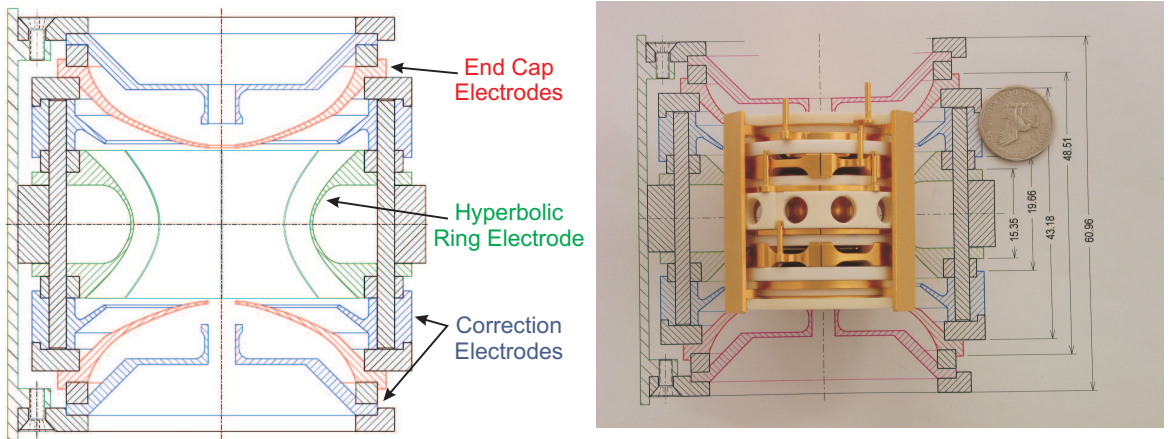
Figure 3.6. (left) Mechanical drawing of the LEBIT Penning trap. (right) Photo of LEBIT Penning trap sitting on schematic drawing of Penning trap, with a Susan B. Anthony dollar used as a scale reference.

The LEBIT Penning trap, shown in Fig. 3.6, has an 8-fold segmented hyperbolic ring electrode. The hyperbolic endcap electrodes have 4 mm holes for ions to enter and exit the trap. A set of correction electrodes minimize deviations in the hyperbolic electric field induced by the endcap holes and the finite extent of the ring and endcap

44

electrodes. Additionally, the trap has been designed in such a way as to minimize magnetic field perturbations induced by the material composition of the trap itself [79].

As the LEBIT Penning trap mass spectrometer is designed to use the TOF-ICR method, described in 2.2.3, an MCP ion detector is installed in a vacuum chamber following the magnet (see Fig. 3.5) in order to measure the time-of-flight of ions ejected from the Penning trap. The MCP is implemented in a so-called "Daly configuration" [80]. In this configuration, the MCP is situated off-center from and perpendicular to the central beamline. A metal plate, biased at -6 kV, is mounted parallel to the MCP on the opposite side of the beamline. Ions strike the plate, creating secondary electrons which are collected on the MCP, yielding an ion detection efficiency of nearly 100%.

A silicon surface-barrier (SSB) β-detector is mounted after the Daly detector. When the Daly plate is biased at the same potential as the MCP, ions are transported to the β-detector instead of impacting the Daly plate. This allows for the option to measure activity after the beam cooler-and-buncher, the importance of which will be discussed in chapter 5.

CHAPTER 4

Technical Developments for the Gas Stopping Station

Many ion transport simulations were performed to help guide the design of the gas stopping station. Simulations of ion extraction from the gas cell were performed for both electrostatic transport and transport utilizing radiofrequency (RF) confinement. Simulation of transport through the ion guide system originally focused on the use of square waves.

All simulations were performed using the commercial program SimIon [81] and the IonFly [63] extension for SimIon written by Stefan Schwarz. Neither of these computer codes account for space charge effects. In order to take space charge effects into account, an extension of IonFly was written.

4.1 Simulation of Ion Extraction from the Gas Cell

After stopping in the helium gas, the ions need to be extracted efficiently and quickly. If gas flow alone were relied upon to move the ion out of the gas cell, the extraction timescale would be on the order of several minutes [72]. Such long extraction times do not provide a good match for the timescale of rare isotope production via projectile

fragmentation. In order to expedite the extraction process electric fields can be used. A static electric field created by a series of annular electrodes can easily guide the ions from the back of the gas cell to the front, provided that space charge effects from the ionization of the gas is not an issue. The critical point is how to get the ions into the extraction nozzle which has a very small opening. For the LEBIT gas cell system, the use of both static electric fields and a combination of RF and static electric fields have been studied.

Each approach has advantages and drawbacks. The use of static electric fields is simple, but requires that the ions can be guided to a point where gas flow provides the dominant force. The combination of static and RF electric fields is potentially less susceptible to deleterious space charge effects brought about by the large number of Helium ions created in the stopping process. It is, however, difficult to implement at the high pressures required to stop ions created via projectile fragmentation. Therefore, as a first concept, the electrostatic approach was chosen for the LEBIT gas cell.

4.1.1 Extraction Using a Combination of Static and RF Electric Fields

Consider a stack of annular electrodes whose inner diameters taper to form a cone. Such systems are called "RF-Funnels" and have been studied and used at low pressures [82, 83, 84]. If an RF signal is applied each electrode, with a 180° phase difference between adjacent electrodes, such a system should have some ion-optical properties analogous to an RFQ ion guide; in particular, such a system should have a low mass cut for ion transport.

By super-imposing a DC-field, ions could be pulled through through the buffer gas, allowing for use as an ion transport system for the extraction of stopped beams. Such systems have been successfully implemented at SHIPTRAP, CPT and RIKEN

for extraction of stopped rare isotope beams produced at low energies. The gas cells at these facilities, however, are operated at pressures 5 - 10 times lower than the LEBIT gas cell.

In the presence of a buffer gas, the pseudo-potential (eq. 2.5) must be modified to become:

$$D \sim \frac{q}{m} \frac{V^2}{d^2} \frac{1}{[\omega^2 + \gamma^2]} \tag{4.1}$$

where γ is proportional to the pressure and d is the characteristic distance – the inter-rod separation in an RFQ ion guide, or the plate separation in an RF funnel. Equation 4.1 makes clear that in order to maintain a given pseudo-potential depth, the RF amplitude would need to be increased for higher pressures. This limits the application of such a technique in a high-pressure regime, as RF high amplitudes could lead to electrical breakdown of the helium gas.
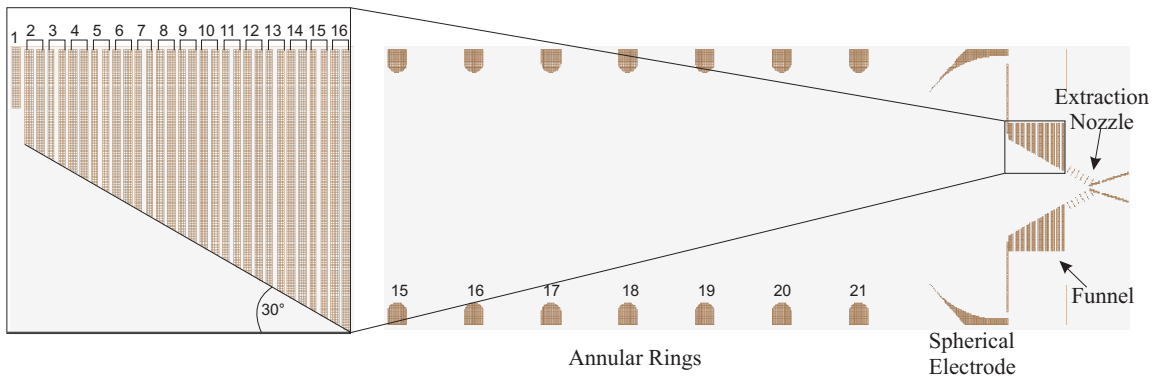
Figure 4.1. SimIon electrode geometry used to study feasibility of an RF funnel at LEBIT. Simulated geometry includes 7 DC drift ring electrodes (labeled 15 - 21) one spherical focusing electrode and 16 funnel electrodes (labeled 1 - 16) of which a zoomed in view is provided.

To investigate the feasibility of using an RF-funnel in the extraction region of the LEBIT gas cell, as shown in Fig. 4.1, simulations were performed using SimIon and IonFly. To match the nozzle, the funnel had an opening angle of 60°. A funnel configuration with 30 segments, 0.5 mm thick and separated by 0.2 mm placed, was

Table 4.1. Electric potentials (in V) for the electrodes used in the RF-funnel simulations. An ion mobility of $K_0 = 18.25$ cm^2/V·s was used.

Rings		Funnel				Nozzle	
#15	400	#1	300	#9	290.7	#1	290
16	370	2	291	10	290.6	2	232
17	340	3	291	11	290.6	3	174
18	340	4	290.9	12	290.5	4	116
19	340	5	290.9	13	290.5	5	58
20	340	6	290.8	14	290.4	6	0
21	340	7	290.8	15	290.4		
Sphere	300	8	290.7	16	290.3		

chosen. The thickness and spacing was chosen based on the minimum sizes of readily available stainless steel sheets and ceramic spacers.

To allow the simulation to take into account ion optical effects associated with transporting ions into and out of the funnel, the geometry include 7 DC drift electrodes and one spherical focusing electrode, as well as an approximation of the nozzle. SimIon has a 35 electrode limit, requiring that two plates of the funnel be treated as a single electrode. This result in an effective doubling of the characteristic distance d.

A number of studies were performed with this geometry. These studies focussed on the RF amplitude required to successfully transport ions through the funnel as a function of ion mass and buffer gas pressure. Nominal values used in these simulations are provided in Table 4.1

The effect of the buffer gas was calculated in a viscous force approximation (see chapter 2.1.3). In this approximation collisions with gas are assumed to be so frequent as to be well represented by a viscous drag. The total force acting on the ion is then given by

$$\vec{F} = q \cdot [\vec{E} - \frac{P}{1013 \cdot K_0} \cdot \vec{v}], \tag{4.2}$$

where $\vec{E}$ is the electric field, P is the pressure in mbar, K_0 is the reduced ion mobility and $\vec{v}$ is the ion velocity. For most ions in helium, $K_0 \approx 18.25$ cm^2/V·s.

Figure 4.2 shows calculated trajectories for two ion species of different mass, A = 4 and A = 40 using the electric potentials listed in Table 4.1 and a pressure of 500 mbar. It can be seen that the RF funnel does not transport the He^+ while transporting heavier ions. This can be explained by analogy with the RFQ ion guide system, where the stability diagram for the quadrupole RF-field features a low-mass cut-off.
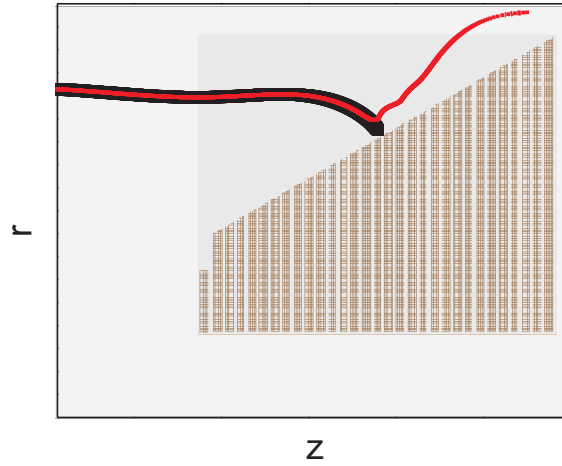
Figure 4.2. Calculated trajectories for two ion species. The red curve is the trajectory for an A=40 ion while the black curve is for an A=4 ion. The RF funnel was operated at 500 mbar with electric potentials as listed in Table 4.1 using a 900 V_{0p} 1 MHz sine wave.

The results of simulations to determine minimum RF amplitudes required for ion transmission as functions of ion mass and buffer gas pressure are shown in Fig. 4.3. Simulations showed no correlation between frequency, ν_{RF}, and required amplitudes. The data show good agreement with equation 4.1, with the largest effect on the required amplitude being the gas pressure. In order to transport ions with A $\approx$ 40 in a high pressure environment would require more then 1000 V_{pp} and would definitely result in an electric breakdown of the helium gas. However, since the system was

approximated by treating adjacent plates as a single electrode, the characteristic distance is twice what it would be in reality. So the amplitude actually required could be reduced by as much as a factor of 4, which may result in an acceptable amplitude.

Based on the results of these simulations, a prototype RF funnel has been constructed recently. The prototype consists of a stack of 62 discs 0.2 mm thick separated by 0.1 mm with ceramic spacers. Tests are underway in a separate test system.
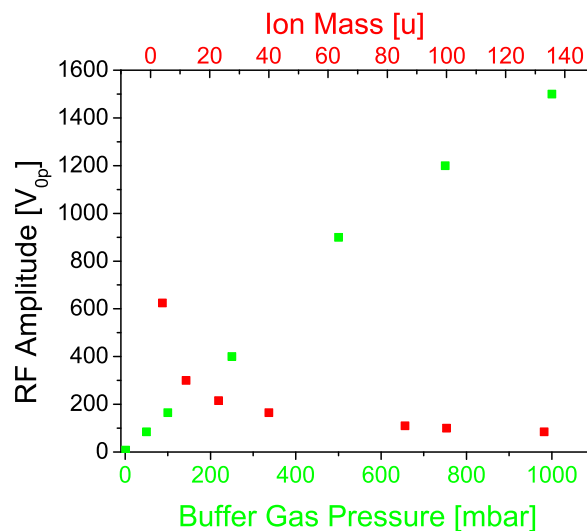
Figure 4.3. Calculated minimum RF amplitudes required for ion transmission in the RF funnel as functions of ion mass and buffer gas pressure. For exploring the required amplitude as a function of pressure, an RF frequency of $\nu_{RF} = 1$ MHz and A=40 ions were used. For exploring the required amplitude as a function of mass, an RF frequency of $\nu_{RF} = 1$ MHz and a buffer gas pressure of 100 mbar were used.

4.1.2 Extraction Using Electrostatic Fields

The use of a static electric field to guide ions to the end of gas cell provides simplicity in operation and sidesteps the difficulties of implementing an RF system in the high pressure buffer gas required to stop fragmentation beams. Annular electrodes, as used

in the simulation of the RF funnel, provide a means to transport ions from the back of the gas cell toward the extraction region so long as space charge effects from the ionization of the buffer gas are sufficiently minimal. Gas flow calculation performed by Victor Varentsov using his VarJet code [85] and gas flow measurements conducted by Pat Lofy [72], indicated that gas flow is the dominant force in the extraction nozzle of the gas cell. As such, an electrode system needed only to transport ions into the extraction region and the gas would move them quickly out of the cell. A number of geometries were investigated for focusing ions into the extraction nozzle.

Combining the electric fields from SimIon with gas flow calculations from Victor Varentsov, simulations of ion extraction from the gas cell by electrostatic transport and gas flow were performed. This was done using IonFly, an extension of SimIon written by Stefan Schwarz [63]. The simulation calculated ion trajectories using electric fields calculated by SimIon and VarJet gas flow fields along with a viscous deceleration given by

$$\ddot{\vec{x}} = -\frac{q}{m}\frac{P}{1013 \cdot K_0}\vec{v},\tag{4.3}$$

where $\vec{v}$ is the ion velocity, P is the pressure in mbar and K_0 is the ion mobility in cm^2/V·s, to approximate the high pressure buffer gas environment. Table 4.1.2 lists the parameters used in the simulation. Extraction is defined in the context of this simulation as transport to the nozzle apex, where the gas flow is assumed to provide the dominant force.

A number of extraction field electrode scenarios were considered. The most promising proved to be the use of spherical electrodes to approximate the field of a point charge within the region of gas flow. A cross-section of the spherical electrodes can be seen at the far right of Fig. 4.5 and a photograph of the electrodes is shown in Fig. 4.4.

In this simulation, the whole gas cell was considered. The configuration used can be seen in Fig. 4.5. By starting with a set of ions spaced at 1 mm radial and 10

Figure 4.4. Photograph of spherical electrodes used to focus ions into extraction nozzle.

cm axial increments, the region from which stopped ions can be extracted can be obtained. For the extracted ions, the mean extraction time can be obtained as well. Figure 4.5 shows the result of one extraction simulation, using the parameters listed in Table 4.1.2; the red lines represent equipotential lines. This simulations formed the starting point for experimental optimization.
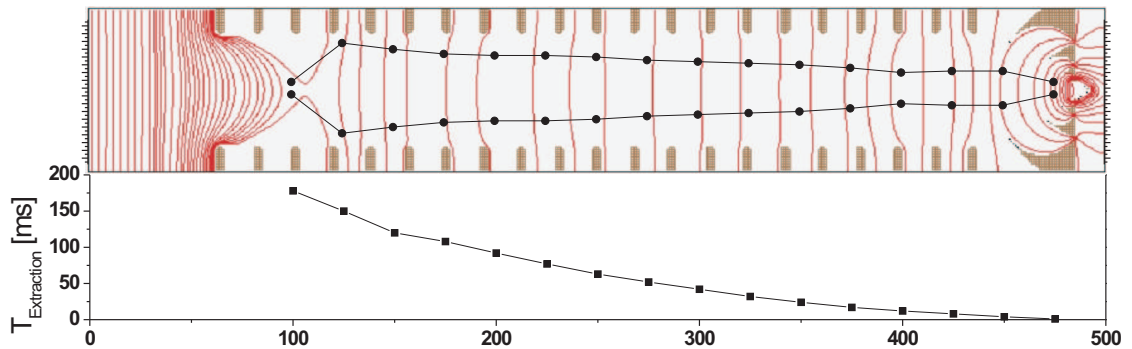
Figure 4.5. (Top) Calculated region of extractability. Ions which initially are stopped in the region between the black lines should be extracted from the gas cell when using electrostatic transport with gas flow. The red lines are equipotential lines. (Bottom) Extraction time as a function of stopping depth inside the gas cell.

Table 4.2. Parameters used in the simulation of ion extraction from the gas cell via electrostatic transport and gas flow. Electrodes are numbered in ascending order away from the entrance window. P and K_0 are the pressure and ion mobility; m and q are the ion mass and charge.

Electrodes							
Rings				Spheres		Nozzle	
#1	1420 V	#11	1300 V	#1	875 V	#1	300 V
2	1415	12	1280	2	850	2	240
3	1410	13	1260	3	705	3	180
4	1400	14	1230	4	510	4	120
5	1390	15	1200			5	60
6	1380	16	1170			6	0
7	1370	17	1140				
8	1360	18	1100				
9	1340	19	1060				
10	1320	20	955				
		Parameters					
		P	1000	mbar			
		K_0	18.25	cm^2/V·s			
		m	100	u			
		q	+1				

The Extraction Nozzle

For the simulation results shown in Fig. 4.5 the potential difference across the nozzle was 300 V. The actual nozzle has a resistance of ≈ 5 kΩ. Thus, a high voltage power supply capable of sinking and sourcing as much as 20 W would be needed to bias the nozzle with a 300 V potential difference. As this also risked overheating the nozzle, in practice the potential difference was always kept below this value. To investigate the impact of this on the extraction efficiency, a series of simulations were performed.

In these simulations, ion extraction for an ensemble of 500 ions evenly distributed within a 5 mm radius 17.5 mm from the apex of the nozzle were simulated for 16 different nozzle potential differences. All other parameters were as in Table 4.1.2. As the ensemble traveled through the nozzle, the number of ions remaining was recorded every 0.1 mm. The results are shown in Fig. 4.6 as a color relief plot of the fraction of remaining ions as a function of axial position and potential difference across the nozzle. The thick black line designates the apex of nozzle where the opening is smallest. All ions reaching this point should be carried out of the gas cell by gas flow.

A number of offline tests have been performed to attempt to verify the results of these simulations - and improve extraction efficiency. Unfortunately, these tests have thus far been unable to duplicate the simulated results. This could be due to space charge effects that have not been considered. Another possibility is that the potential may not distribute across the nozzle in the linear manner that has been assumed.

4.1.3 Extraction Simulations with Space Charge Included

The SimIon program used to calculate electric fields and calculate ion trajectories solves the Laplace equation,

$$\nabla \cdot E = 0 \tag{4.4}$$
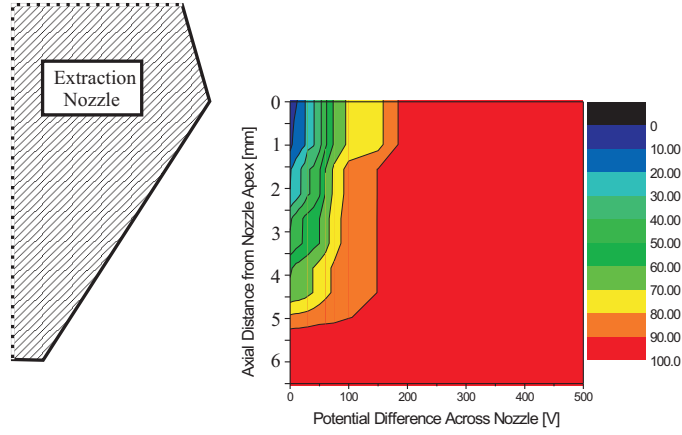
Figure 4.6. Color relief plot of ion survival fraction as a function of distance and potential difference across the nozzle. The hashed figure represents the nozzle in cross-section, to enhance visualization.

This is an appropriate approximation when the charge density of the moving ions is low. In the extraction region of the gas cell, however, the ion density becomes quite large and the electric field is can be greatly modified by space charge. To model such conditions, one must solve the Poisson equation,

$$\nabla \cdot E = 4\pi\rho, \tag{4.5}$$

where ρ is the charge density.

In order to calculate the trajectories of ions under realistic conditions, code was written to determine the space charge effect. The first step is to determine the charge density. This is done using two grids, V_{ij} and N_{ij}, for the z-velocity and number density. The granularity of each is $2\pi r \Delta r \otimes \Delta z$. Ion trajectories for an initial ion distribution are calculated based on the electric field determined from the Laplace solution and used to populate V_{ij} and N_{ij}. Each is then normalized using

$$V'_{ij} = V_{ij}/N \tag{4.6}$$

$$P_{ij} = N_{ij}/N \tag{4.7}$$

$$N = \sum N_{ij}\Delta^3 r, \tag{4.8}$$

where P_{ij} is now the reduced charge density. In cylindrical coordinates $\Delta^3 r$ is given by $2\pi r_{ij}\Delta r$. The charge density is given by

$$\rho_{ij} = \frac{IP_{ij}}{2\pi r \Delta r V'_{ij}}, \tag{4.9}$$

where I is the current.

Once the charge density has been determined, a successive over-relaxation (SOR) technique is used to solve the Poisson equation

$$\nabla^2 \phi = -4\pi\rho \rightarrow \begin{pmatrix} a & b & c & d & e \end{pmatrix} \begin{pmatrix} \phi_{(i+1)j} \\ \phi_{(i-1)j} \\ \phi_{ij} \\ \phi_{i(j-1)} \\ \phi_{i(j+1)} \end{pmatrix} = -4\pi\rho_{ij} \tag{4.10}$$

with

$$\begin{pmatrix} a \\ b \\ c \\ d \\ e \end{pmatrix} = \begin{pmatrix} \frac{1}{\Delta r^2} + \frac{1}{2r\Delta r} \\ \frac{1}{\Delta r^2} - \frac{1}{2r\Delta r} \\ \frac{1}{\Delta z^2} - \frac{2}{\Delta r^2} \\ \frac{1}{\Delta z^2} \\ \frac{1}{\Delta z^2} \end{pmatrix} \tag{4.11}$$

The boundary conditions are given by the electrode potentials. With the electric potential ϕ solved for, the trajectories of the initial ion distribution are calculated for the new electric field. Using the new trajectories, the charge density is re-calculated and the Poisson equation solved for again. This process is repeated until the standard deviation of the change in charge density between successive ion trajectory calculations is less than a preordained value.

In order to expedite the calculation of the electric potential using the method of successive over-relaxation, the residual field technique is used. This technique is based on the assumption that the global nature of the solution is only slightly changed from one charge density iteration to the next. Thus, to prevent the SOR algorithm from wandering too far from the original Laplace solution, after each SOR iteration the solution is combined with the previous iterations solution as such:

$$\phi_{n+1} = R \cdot \phi_{n-1} + (1 - R) \cdot \phi_n, \tag{4.12}$$

where the subscripts refer to the SOR iteration and R is the residual field parameter. For simulations of extraction from the gas cell, a residual field parameter of R = 0.9 was used.

Extraction Calculations
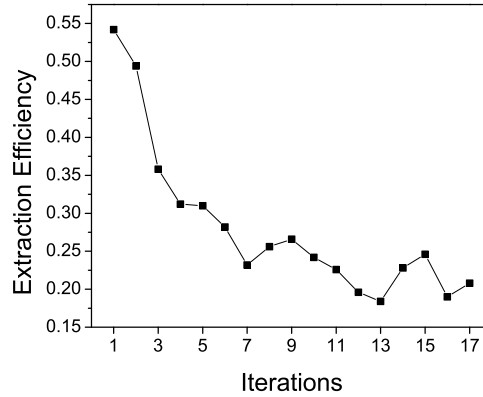
Figure 4.7. Extraction efficiency as a function of iteration number from an extraction simulation with 1 nA ionization current.

Gas cell extraction simulations were performed, using the IonFly code with the extension for space charge described above. These simulations used the same geometry as shown in Fig. 4.5 with the potentials listed in Table 4.1.2. The assumed initial ionization distribution was a radial gaussian distribution of 10 mm FWHM at an axial position of 100 mm from the entrance window.

The extraction efficiency as a function of iteration number from an extraction simulation with 1 nA ionization current is shown in Fig. 4.7. Calculations were performed for ionization currents of 1 pA to 10 nA in decade steps. By multiplying the ionization current by $2 \times 10^7 e$ the equivalent incoming beam rate can be obtained, based on the assumption that each incoming particle creates 10^7 He^{++} ions. Figure

4.8 shows the results of calculations for various ionization currents scaled to incoming beam rates, compared to actual measured extraction efficiencies [86].
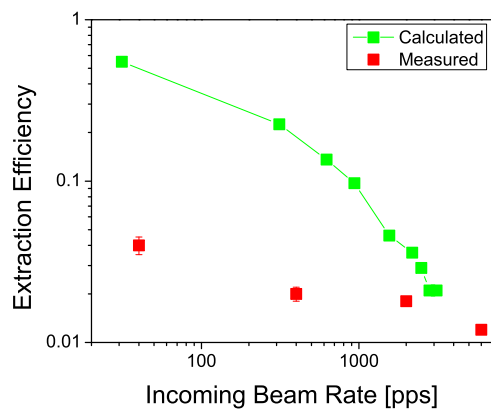
Figure 4.8. Comparison of extraction efficiencies for A=40 ions calculated with space charge effects included and measured extraction efficiencies for ^{38}Ca [86].

4.2 The RFQ Ion Guide System
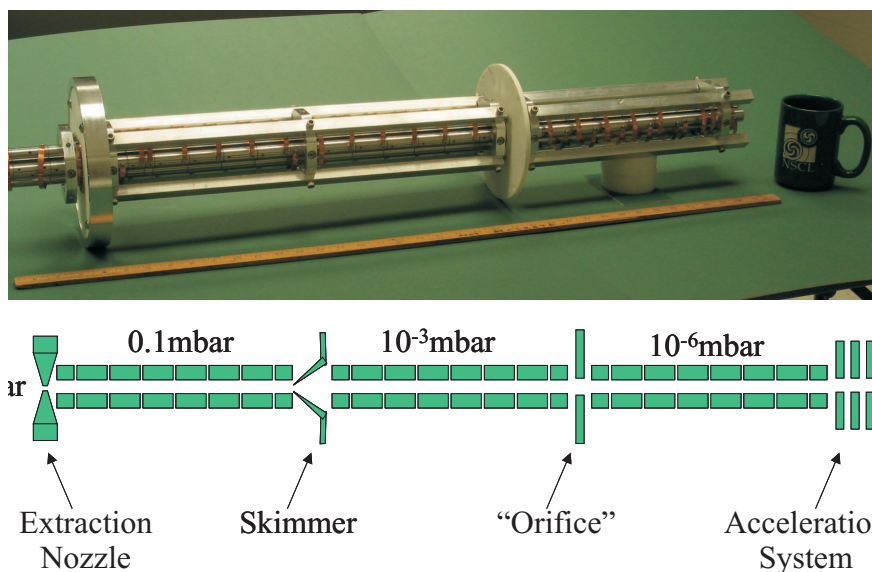
Figure 4.9. (Top) A photograph of the original ion guide system. (Bottom) A cross-sectional sketch of this system.

The original design goals for the LEBIT ion guide system called for a flexible and robust system to transport ions through a differentially pumped region. In order to provide simple beam transport, it was decided to operate the ion guide with square waves. This would allow for easily varying the operational frequency of the ion guides while avoiding the need for tuned circuits and expensive RF power amplifiers required for sinusoidal operation. Square wave operation could also provide simplified mass filtering compared to sinusoidal operation.

A number of computer simulations were performed to study operation of an ion guide with square waves. These simulations indicated that a segmented ion guide operated with square waves would provide efficient transport of ions extracted from the gas cell. Based on the results of the simulations, a segmented RFQ ion guide system, shown in Fig. 4.9, was constructed.

4.2.1   Ion Guiding with Square Waves

In order to provide radial confinement, the quadrupole potential of the ion guides needs to be oscillatory, but not necessarily sinusoidal. The use of square and even sawtooth waveforms was demonstrated by Richards et al. [87] as early as 1973. The use of square waves provides certain advantages over traditional sine waves. One advantage is that many inexpensive integrated circuits exist for the control of digital signals, simplifying electronic design.
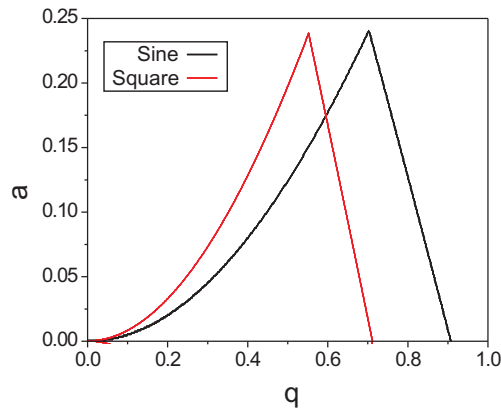
Figure 4.10. Comparison of stability diagrams of square wave and sinusoidal wave operated RFQ ion guides.

A study of the stability diagram for square waves was performed using a small program written in C++. The program simply calculates trajectories of the equation

$$\ddot{u} = [2q_u f(\omega t) - a_u] \cdot u, \tag{4.13}$$

where f(t) is an oscillatory function, u is x or y and

$$a_x = -a_y \tag{4.14}$$

$$q_x = -q_y \tag{4.15}$$

are the standard Mathieu parameters. If ω reaches 1500π without u exceeding unity, the motion is considered stable. The calculation is repeated for a set of (a,q) values, creating a stability diagram. Figure 4.10 shows a comparison between the stability diagram for a square wave and a sinus wave. The stability diagram for the square wave is identical to that of the sinus wave, but with the q-axis compressed by a factor of $\pi/4$. This could be expected as the Fourier expansion of the square wave is given by

$$f(t) \sim \frac{4}{\pi} \sum \frac{1}{n} \sin n\pi t, \tag{4.16}$$

with n odd. The q-parameter for the higher harmonics will always be much lower than for the fundamental harmonic, which therefore determines the shape of the stability diagram.
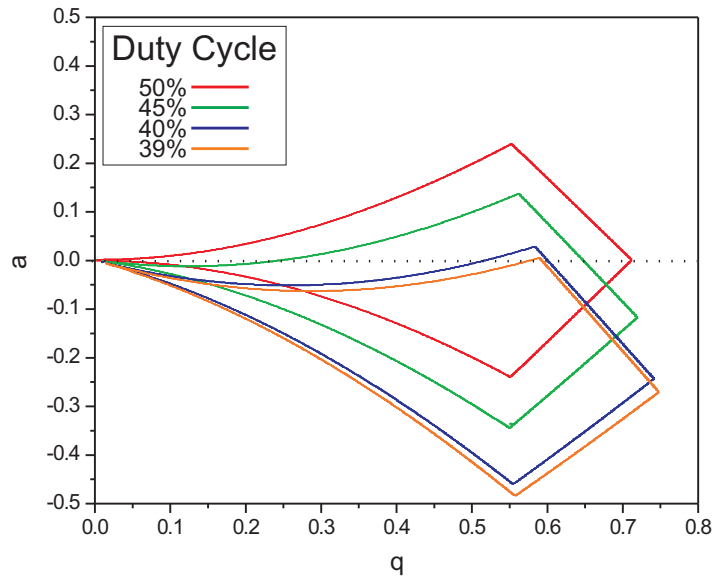
Figure 4.11. Comparison of stability diagrams of square waves for various duty cycles.

Another advantage to using square, pointed out by Richards et al. [87], is that for

square waves with a duty cycle (the ratio of the pulse duration to the pulse period) of less than 50% the stability diagram appears to shrink. Using the same simple program, this was studied as well. In reality, the stability diagram does not shrink, but is rotated in (a,q) space due to an average DC potential from the asymmetry in the duty cycle. For a duty cycle of $\delta \approx 39\%$ the tip of the stability diagram intersects $q = 0$, as shown in Fig. 4.11.

Operated under such conditions, only the duty cycle and the RF-amplitude would need to be accurately maintained to operate as a high-resolution mass filter, while in a traditional system the ratio of DC- to RF- amplitudes needs to be maintained. Also, note that the tip of the stability diagram is located at a lower q-value for square waves than for sinus waves; this implies lower RF-amplitudes would be required.

In order to determine how real square waves would behave, an oscilloscope was used to capture actual output signals from the square wave generator (see next section and appendix). These signals were used for the function $f(\omega t)$ in equation 4.16. Figure 4.12 is the result of this study. The gaps in the stability diagram are likely caused by harmonic components at the secular frequency that are known to cause instabilities [88].

4.2.2 Simulations of Ion Transport Through the Ion Guide System

Prior to construction of the ion guides, ion optical simulations were performed to test the feasibility of using square waves under the conditions which would be present - a high pressure region, large inter-rod gap (required to "catch" ions in the supersonic gas jet) and an electrostatic skimmer required for differential pumping. Computer simulations to compare overall transport efficiency, under realistic conditions, for square wave and sinus wave operated ion guides were also performed.

The simulations were performed using SimIon to calculate the electric fields and

63
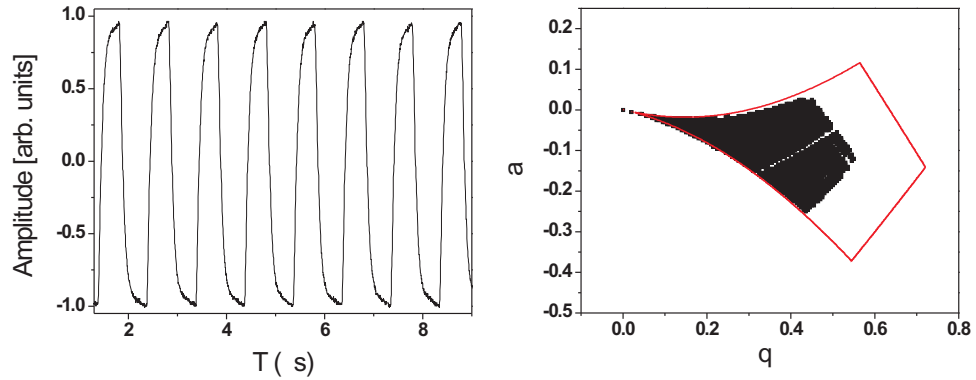
Figure 4.12. (left) Measured output of the square wave generator. The duty cycle of the output is ≈55%. (right) Calculated stability diagram based on square-wave generator output. The envelope represents the stability diagram for a perfect square-wave with a duty cycle of $\delta = 55.2\%$.

the IonFly code to calculate ion trajectories. Simulations were performed neglecting space charge and gas flow, and treating ion-buffer gas collisions through the viscous approximation (see chapter 2.1.3). Simulations of the ion guides operated with sinus and square waves showed similar transport efficiencies in both cases, with calculated efficiencies as high as 60%.

The Skimmer

The primary function for which the ion guide system was designed was to transport ion through a series of differentially pumped vacuum chambers. Efficient differential pumping required that the orifice in the pumping barrier through which the ion could pass needed to be smaller than the open area of the ion guide. To minimize turbulent gas flow near the pumping barrier, Victor Varentsov used his VarJet code to optimize a "gas skimmer" geometry for the orifice in the pumping barrier.

While it was known from Victor Varentsov's simulations that the skimmer would allow for smooth gas flow, it was not clear to what degree it would disturb the

64

ion optical trajectories by distorting the RFQ field. To investigate this, ion optical simulations were performed.

The skimmer, as simulated, was 30 mm in length, with an opening angle of 45°. A 4.5 mm gap between the skimmer and the RFQ existed on either side.

Simulations were performed to determine transport efficiency through the skimmer as functions of RF frequency, pressure and potential difference between the RFQ and skimmer. The simulation used ions starting on a grid, separated by 1 mm, filling the bottom half of the ion guide at a distance of 1 cm from the start of the skimmer.

The transport efficiency was found to be independent of the potential difference between the skimmer and RFQ, so long as the electric field was properly oriented. The calculated transport efficiency for A = 40 ions as a function of RF frequency, with an amplitude of 100 V_{0p}, is shown in Fig. 4.13 for two pressures. For the low pressure scenario, insufficient cooling results in decreased transmission. For the higher pressure scenario, a decreased efficiency was seen at lower frequencies. This may be an effect of the low-mass cut of the ion guides.

4.3 Implementation and Commissioning of the LEBIT Ion Guides

Based on the promising results from simulations, the ion guide structure was designed and assembled as simulated and an RF square wave generator was designed and built. Initial tests of the ion guide system showed transport performance in agreement with simulations.

Figure 4.9 provides both a photograph and sketch of the first ion guide system, which was based upon a segmented ion guide used at ISOLTRAP. The full length of the system was in excess of a meter. For differential pumping, the system incorporated two diaphragms. A skimmer, described earlier, was placed between the 8th and 9th
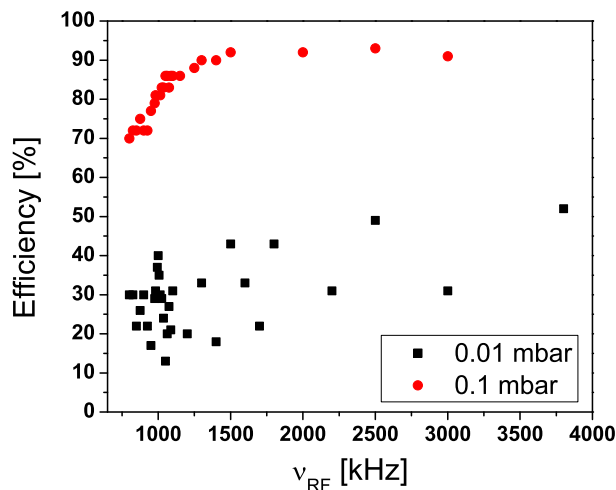
Figure 4.13. Transport efficiency of skimmer as a function of RF frequency. Constant parameters were: δV = 50 V, U_{RF} = 100 V_{0p}, skimmer in center position.

segments and a second diaphragm was placed between the 22nd and 23rd segments. A more detailed description of the mechanical and electrical implementation can be found in Appendix B.

During the online commissioning of the gas cell, strong molecular ion beams were always extracted from the gas cell, requiring mass separation before the beam could be used for Penning trap mass measurements. Mass filter operation of the ion guides was required and implemented. An improved system was later installed and will be discussed in chapter 5. After discussing the results of initial testing, attempts to operate the system in a mass filter mode will be described and their results presented.

4.3.1 Reverse Transport Study of the Square Wave Driven RFQ Ion Guide

To study the ion guides offline, the plasma ion source (see Fig. 3.1) was used to generate ^{40}Ar$^+$ ions. The quadrupole deflector was setup to direct the ion beam

upstream towards the gas cell. The current from the ion source was determined using a Faraday cup in BOB1, the beam observation box nearest the ion guide system. The gas cell nozzle was used in place of a Faraday cup after the ions passed the ion guides to monitor the beam current.

The ion guide efficiency was tested by scanning both amplitude and frequency. Before and after measuring the current on the gas cell extraction nozzle, the current on the BOB1 Faraday cup was measured to account for any drift in the current provided by the ion source. As these tests were not intended to be an exacting study so much as a proof of principle, the measurement uncertainty was determined by visually estimating the fluctuations in the electrometer; the fluctuations tending to be on the level of picoamps, while the beam current was generally several nA.

Figure 4.14 show the results of the reverse transport tests. Figure 4.14a shows measured efficiencies at several RF amplitudes as a function of RF frequency. Figures 4.14b and c compare measured and calculated efficiencies for ^{40}Ar$^+$ with a beam energy of E = 35 eV and the ion guides operated at $U_{RF} = 164$ V$_{0p}$. While the general shape of the calculated transport efficiency curves agrees with measurements, the calculations appear to consistently underestimate by a factor of ≈ 2. These calculations were performed assuming a worst-case scenario of a beam which filled the ion guides, which likely accounts for the disagreement with measurements.
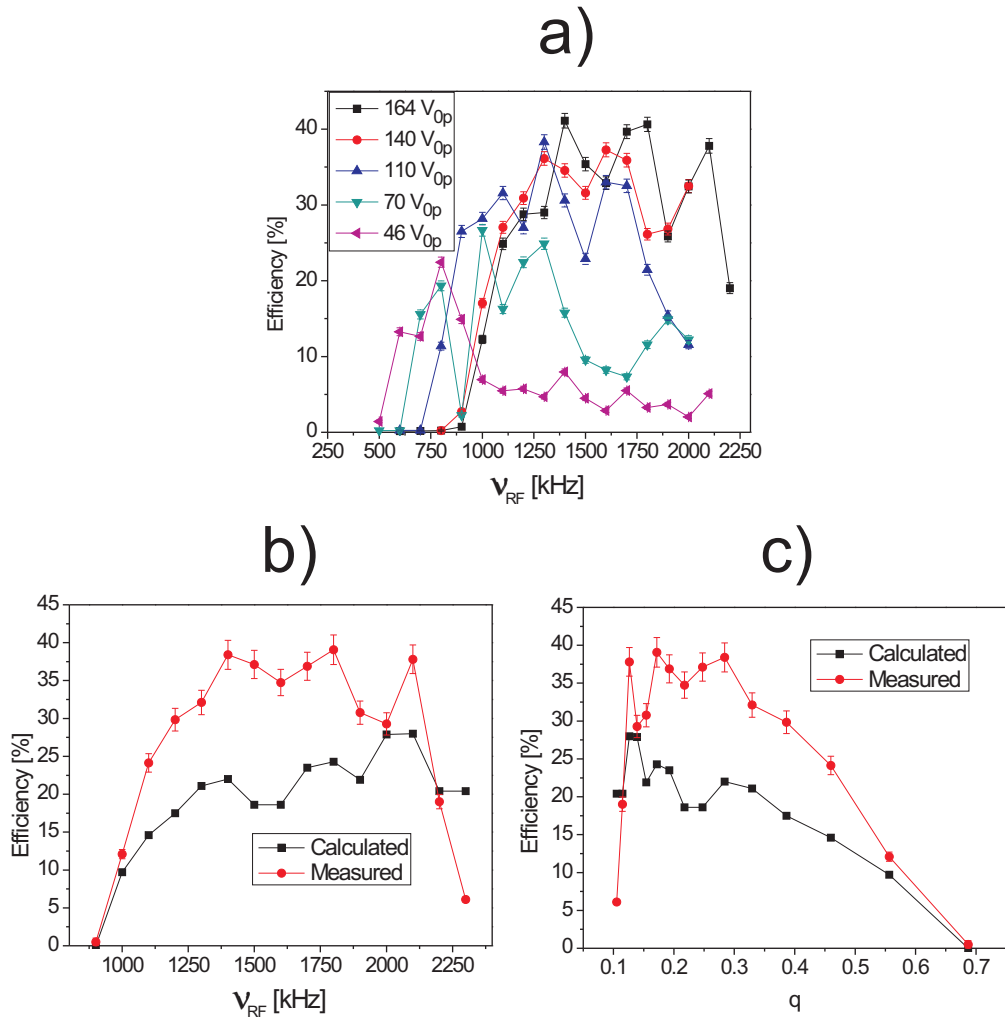
Figure 4.14. a) Measured efficiency as a function of RF frequency for several RF amplitudes. b) Measured and calculated efficiency as a function of RF frequency for a fixed RF amplitude of $U_{RF} = 164$ V$_{0P}$. c) Same as b, but as a function of the Mathieu parameter q. All measurements were performed using ^{40}Ar$^+$ with a beam energy of E = 35 eV.

4.3.2   Ion Guide Mass Filtering – First Implementation

The first attempt at operating the LEBIT ion guide system as a mass filter was to simply add a DC quadrupole potential to the RF square wave quadrupole. This required altering the RF distribution circuit (see Appendix B) and implementing a paired LC circuit as shown in Fig. 4.15. The segments of the RFQ system furthest from the gas cell were used for this purpose, as they were located in a high-vacuum region.
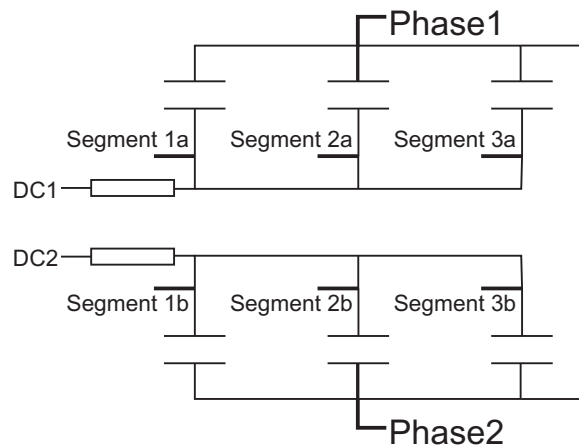
Figure 4.15. Modified RF distribution circuit used for implementing the square wave RFQ as a mass filter.

With the system modified to allow for mass filtration, the system was studied again in reverse transport mode using ^{40}Ar$^+$ from the test ion source. For a fixed frequency and no DC quadrupole potential, the RF amplitude was scanned from about 50 V$_{pp}$ up to about 250 V$_{pp}$. This was done for several frequencies. After each step the current on the gas cell nozzle was recorded. The ion source current was periodically measured, using the BOB1 Faraday cup. The data from this test is shown in Fig. 4.16 in the form of efficiency as a function of Mathieu parameter q for each frequency.

A second test was performed to test the functionality of the mass filter. This was
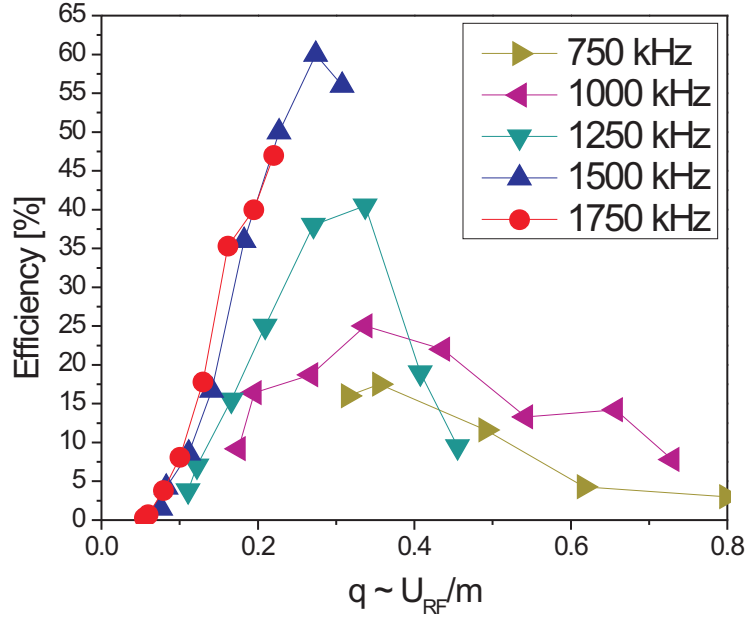
Figure 4.16. Measured efficiency of the ion guide for various square wave frequencies as a function of Mathieu parameter q. For higher frequencies the data range is limited due to limitations in the maximum amplitude which could be achieved.

performed by scanning the frequency for fixed RF and DC quadrupole amplitudes - which is the same as scanning along the mass scan line (see Fig. 2.7). The data provided by such measurements provides a visualization of the stability diagram for the ion guides as well as a test of the mass filter efficiency. These are shown in Fig. 4.17. Figure 4.17a shows no transmission of ions in the tip of stability diagram, indicating that the device was not capable of single mass resolution.

Figure 4.17b shows the same data as 4.17a, but plotted as transmission curves for various scan lines α_{MF}. From Fig. 4.17b we can infer that for a resolution of ≈ 4 u the relative efficiency is $<25\%$. Looking at the data from 4.16, it can be assumed that at least part of this efficiency reduction comes from the low frequency at which the peak is located. Operating the ion guides such that the peak would have been

at a higher frequency may have provided better transmission. However, this would have required higher amplitudes than the RF squarewave generator was capable of providing.
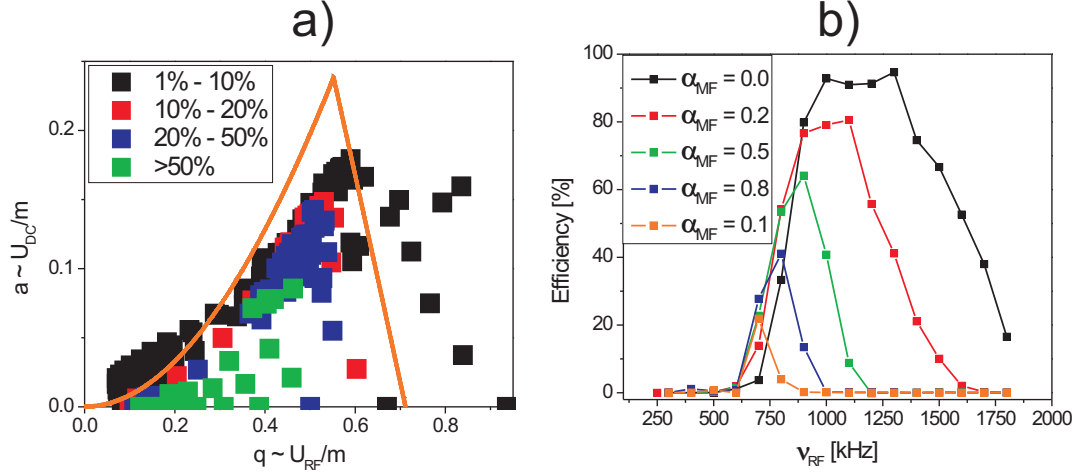
Figure 4.17. a) Measured efficiency for points on the stability diagram of the square wave driven ion guides. The orange curve is the expected theoretical envelope of the stability diagram. b) Cuts through the stability diagram along various scan lines.

In order to overcome the amplitude limitations of the squarewave generator, a tuned circuit was implemented so as to operate the ion guide with sinus waves. As the capacitance of the ion guide system as a whole was more than 1 nF, it was decided to only operate the segments after the "orifice" (see Fig. 4.9) with this tuned circuit to minimize amplifier power requirements. The ion guide system up to the "orifice" was operated with the squarewave generator.

The tuned circuit was operated at 1.2 MHz, for which efficient transport was observed with the square wave ion guide, as seen in Fig. 4.16. Similar tests as for the square wave mass filter were performed. Using the test ion source, $^{40}Ar^+$ ions were sent toward the gas cell and the current on the nozzle was measured. Figure 4.18 shows the results of these tests. In Fig. 4.18, top, the measured data points
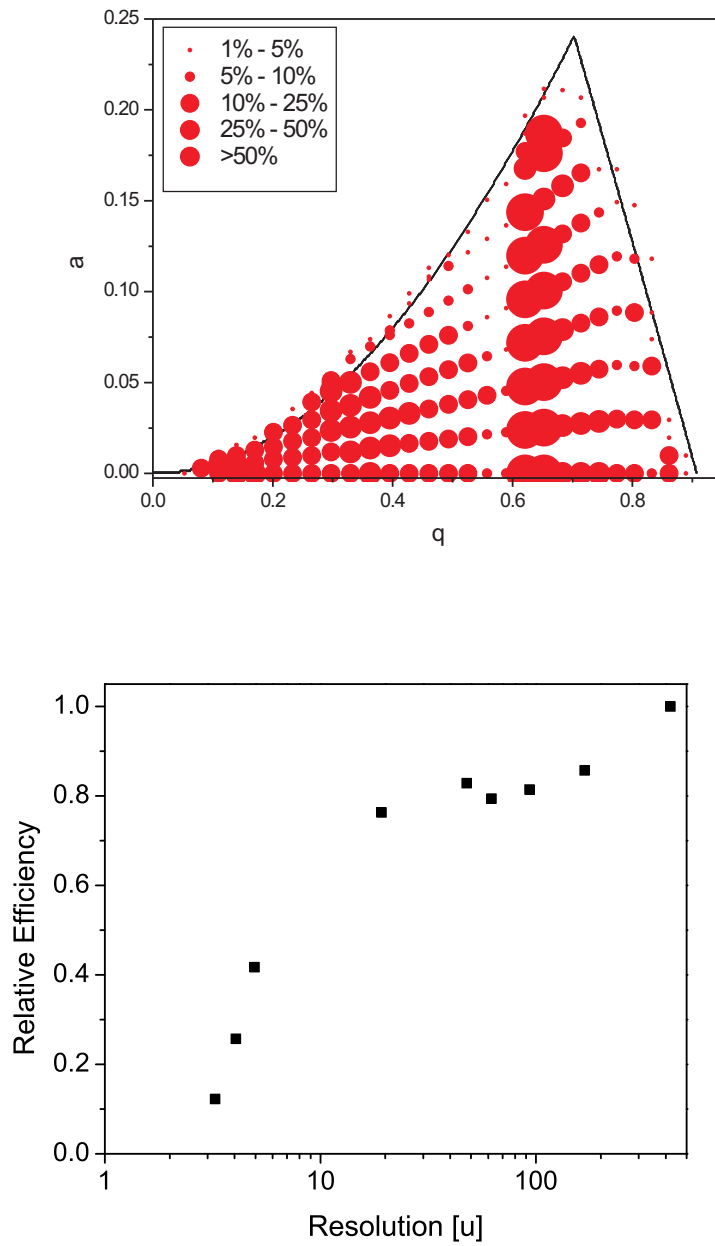
Figure 4.18. (top) Measured stability diagram for the sinus wave driven ion guides. (bottom) Measured relative efficiency of sinus wave driven ion guides as a function of mass resolution.

are plotted in (a,q) space, with points with an efficiency of less than 1% excluded. As can be seen, the shape is approximately as expected, but the efficiency is not uniform. The high efficiency patch near $q = 0.35$ could be associated with $^{40}Ar^{2+}$. Alternatively, the behavior seen could be the effect of a secular resonance near $q=0.55$ resulting in ion loss.

In order to measure the cost of operating the ion guides as a mass filter, the efficiency relative to non-mass filter operation can be plotted a function of resolution, as shown in Fig. 4.18, bottom. This was done by plotting each scan in a way similar to Fig. 4.17b and determining the width and center of the transmission curve for each scan line. The resolution was determined by dividing the scan center by the full width of the curve at half maximum and multiplying by 40 u, the mass of the ions.

Comparing the resolution which could be achieved with the tuned circuit for a given efficiency with that of the square wave system showed roughly a factor of 2 improvement. This was quite sufficient to reduce neighboring contaminants so as to identify them with the Penning trap, but was not sufficient to separate the radioactive ions of interest from the contaminants. Based on the difficulty encountered in converting the original ion guide system into a mass filter, it was decided to completely redesign the ion guide system with an emphasis on mass filtering. This will be discussed in the following chapter.

CHAPTER 5

Beam Purification at LEBIT

The first attempts to perform mass measurements on thermalized fragmentation beams using the LEBIT Penning trap mass spectrometer were unsuccessful. The beam extracted from the gas cell in the first online test using the full LEBIT facility measured in excess of 10 pA, indicating the extraction of a large amount of non-radioactive (stable) ions from the gas cell. This stable ion beam was analyzed via time-of-flight of the ion pulse ejected from the buncher. An example time-of-flight spectrum is given in Fig. 5.1. Using the Penning trap mass spectrometer for un-ambiguous identification, the stable beam was found to be essentially composed of hydrocarbon molecular ions.

In order to be able to perform mass measurements on rare isotope ions extracted from gas cell, the level of stable molecular ions needed to be reduced significantly. The first step toward reducing the intensity of the stable beam extracted from the gas cell was to thoroughly clean the gas cell. The gas cell was disassembled and each part was cleaned using ultra-pure acetone, methanol and deionized water in a class 10000 clean room. It was then reassembled, evacuated and baked at 150 °C for several weeks. While this improved the situation, typical stable beam currents still exceeded 1 pA. With a typical rate of extracted rare isotopes on the order of 10 /s,
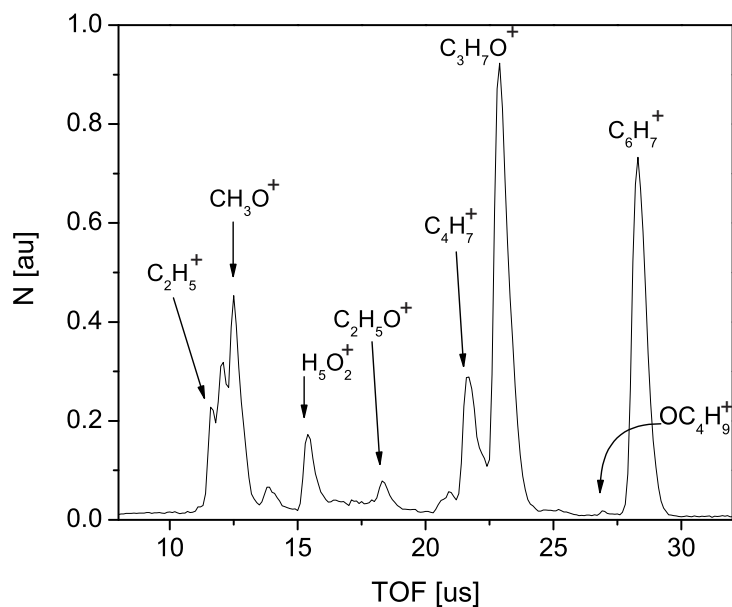
Figure 5.1. Typical time-of-flight mass spectrum after ejection from the buncher of ions extracted from the gas cell before major cleaning of the gas cell and prior to implementation of the beam purification system. The rare isotope ions of interest would have a relative intensity of $< 10^{-5}$ under these conditions.

the situation remained a veritable case of finding a needle in a haystack!

As discussed in the previous chapter, the initial design of the ion guide system following the gas cell was optimized for efficient transport with square wave operation. For reasons outlined in the previous chapter, the mass resolving power of the original ion guide system was not adequate to achieve single mass resolution without a considerable efficiency loss.

A much more powerful beam purification system was needed. Installation of an magnetic isobar separator or a purification Penning trap [48] was not an option due to space constraints. Instead, a suite of beam purification techniques which did not require extending the beam-line were developed and implemented. The first purification is performed with an improved, newly designed RFQ ion guide mass filter.

Isobaric molecular ion contaminants remaining after the mass filter were reduced by means of collision induced dissociation (CID) in the beam cooler. The break-up products can be separated from the ions of interest by means of a time-of-flight mass filter prior to the Penning trap. Any remaining isobaric contaminants are selectively removed from the Penning trap via excitation of their reduced cyclotron motions. This multi-step beam purification scheme has been found to be effective at separating the "needle" of rare isotopes from the "haystack" of stable molecular ions extracted from the LEBIT gas cell.

5.1 Improved RFQ Ion Guide and Mass Filter System
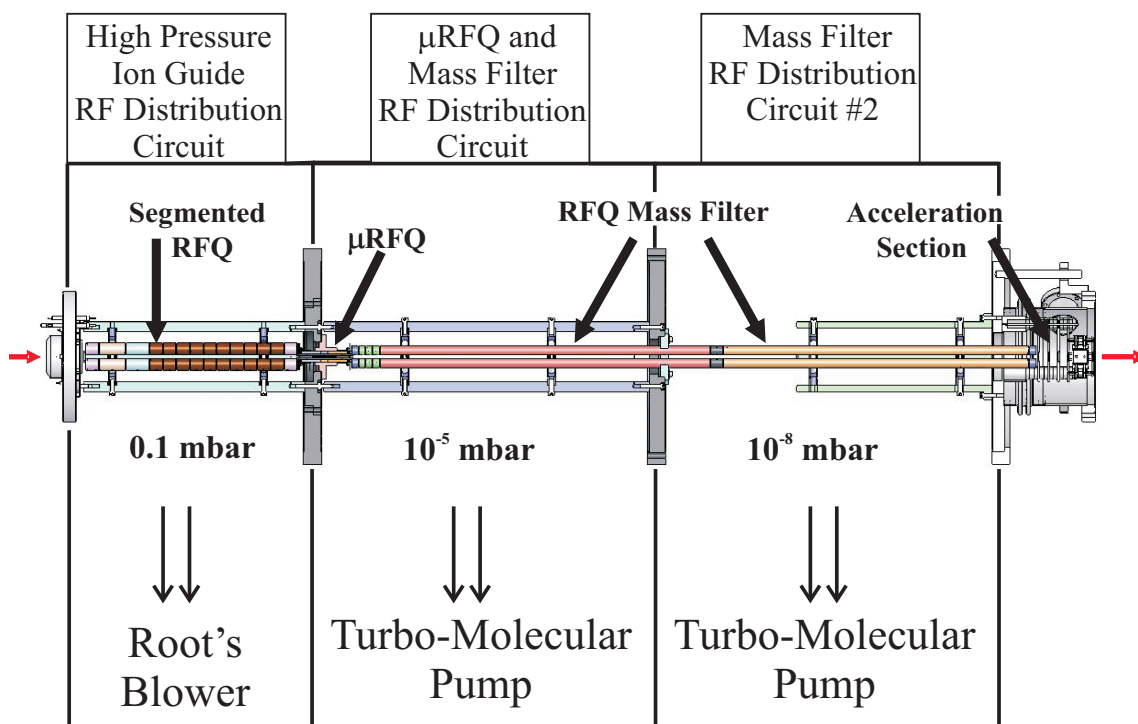
Figure 5.2. Schematic of LEBIT ion guide system

As discussed in the previous chapter, the original RFQ ion guide could not achieve

single mass resolution without an enormous decrease in transmission efficiency (see Fig. 4.18). Therefore the ion guide system was completely redesigned with an emphasis on achieving both high mass resolution and transport efficiency.

5.1.1   Physical Implementation

The redesigned ion guide system is shown in Fig. 5.2. The major changes compared to the original design are the implementation of a μRFQ instead the skimmer and the use of an only modestly segmented ion guide operated as a mass filter. As in the original system, the high-pressure ion guide has the purpose of guiding the ions through the high-pressure region directly after the gas cell. The μRFQ acts as a differential pumping barrier while transporting ions to the mass filter ion guide. The mass filter ion guide has the purpose of providing suppression of non-isobaric molecular ions.

High Pressure Ion Guide

While the mechanical construction of the high-pressure ion guide was not changed in the upgrade, the wiring scheme was improved. The segments along each rod are now connected in-vacuo using resistors[1] which are rated for use in UHV systems and certified to contain no organic materials. The final three segments are wired to allow superposition of a high frequency (HF) dipole field perpendicular to the ion guide axis. This could allow the possibility of selective CID via excitation of an ion's secular motion. If the rare isotopes are extracted as several molecular sidebands, this could provide a means to reduce them to a single molecular sideband.

μRFQ Ion Guide

The μRFQ ion guide replaces the electrostatic skimmer used in the original ion guide system. As a long tube, it provides a better pumping barrier than the skimmer.

---

[1]**RG1/4S 1M J** from Japan Hydrazine

Unlike the skimmer, the μRFQ ensures ion confinement along the entire length of the ion guide.

This μRFQ is identical in construction to the one installed between the cooler and trap sections of the beam cooler-and-buncher [45]. It has an inter-rod separation of $r_0 = 0.3$ mm and uses wedged electrodes to supply an electric gradient for dragging ions through it.

The RFQ Ion Guide Mass Filter

The new mass filter consists of only 6 segments: four 10.5 mm segments followed by a 95 cm segment which in turn is followed by another 10.5 mm segment. The inter-rod separation is $r_0 = 6$ mm, with a ratio of the radius of the rods to the inter-rod separation of $\frac{r}{r_0} = 1.148$. This ratio is known to give the best approximation to a hyperbolic field [61].

To further improve efficiency when operated at higher resolving powers, a delayed-DC field approach has been implemented, similar to that of Brubaker [89]. By using a series of segments with increasing DC quadrupole amplitudes, the ions are eased into the top of the stability diagram, without passing through any regions of instability. This is illustrated in Fig 5.3.

The mass filter compresses the beam along the focussing axis of the DC quadrupole while stretching the beam along its defocussing axis. Such beam asymmetry could lead to increased optical abberations in one dimension in the electrostatic transport system. In order to gradually restore the symmetry of the ion beam, the final segment of the system is operated at 25% of the DC quadrupole amplitude of the mass filter, acting much as a quadrupole lens.
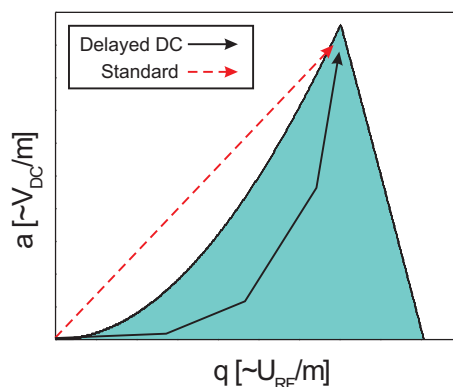
Figure 5.3. Illustration of the advantage of using the Delayed DC-field approach. Without the delayed field, an ion entering the mass filter would pass through a region of instability. By slowly increasing the DC-quadrupole strength, the ion can avoid the region of instability.

5.1.2 The RF Control System for the RFQ Ion Guide

Control of the ion guide system is achieved with a multilayered system of electronics; many of the details will be given in Appendix C and only an overview will be provided here. The system consists of a low-voltage RF driver, RF power amplifiers, tunable resonant LC circuits, a set of specially designed RF amplitude monitors and distribution circuits. The system can be controlled through a PLC system connected to a control computer. A flowchart of the RFQ ion guide electronics system is given in Fig. 5.4.

The components inside the large box in Fig. 5.4 comprise the low-voltage driver system, which provides a set of phase-locked RF signals. The amplitude and relative phase of each signal can be set via analog voltages from the PLC system. The frequency can be set using an internal frequency generator controlled with the PLC system; alternatively, the system can be phase-locked to an external RF source.

The low-voltage signals are sent to RF power amplifiers whose outputs are con-
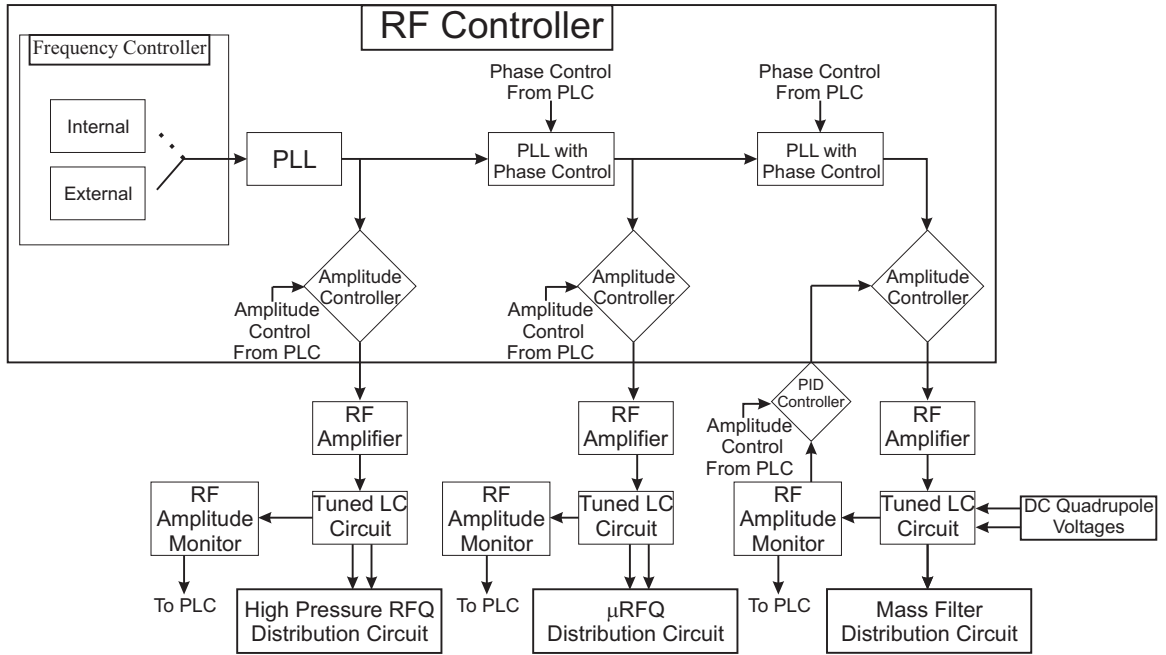
Figure 5.4. Flowchart illustrating the ion guide RF system developed in this thesis work.

nected to the ion guides through a set of tunable resonant LC circuits. The RF amplitude of each ion guide is monitored by means of specially designed RF monitor circuits (see Appendix D.1) connected to the PLC system. The RF amplitude of the mass filter is stabilized at the 100 mV level by means of a computer controlled PID loop.

5.1.3 Commissioning Tests

A number of tests were performed to study the performance of the upgraded ion guide system. The system was tested for overall efficiency, maximum resolving power and relative efficiency as a function of resolving power. A series of tests were also performed to study the use of CID in the high-pressure ion guide.

Overall Transport Efficiency

In order to study the overall efficiency, two tests were performed using ions created in the gas cell. For the first test, the ions were created via electric discharge; for the other test ions were created using a rubidium ion source temporarily installed inside the gas cell. For both tests, all electrodes of the high-pressure ion guide were initially tied together and connected to a Keithley model 6514 electrometer to measure the ion current extracted from the gas cell and entering the high pressure ion guides. The RF system was then reconnected to the high pressure ion guides and the ion current transported through the entire ion guide system was measured on the Faraday cup at BOB1.

In the first test, a discharge inside the gas cell was used to ionize the helium buffer gas; the helium ions charge exchange with contaminants in the gas to create ions which can be transmitted through the ion guides. The extracted ion current measured was $I_0 = 80$ pA. The transmitted current measured was $I_{BOB1} = 18$ pA. The difficulty here is the unknown composition of the beam extracted from the gas cell. Helium ions, for instance, would be extracted from the gas cell and contribute to the measured I_0, however they would not be transmitted through the RFQ system. This test placed a lower limit on the efficiency of $\epsilon = \frac{I_{BOB1}}{I_0} = 23\%$.

In the second test, a Rubidium surface ionization source was used to create ions in the gas cell. The use of the Rubidium source has the advantage that is does not create Helium ions. The Helium pressure required for extracting ion from the gas cell also cooled the Rubidium source and it was difficult to heat it enough to create very many Rubidium ions. The extracted ion current was measured to be $I_0 = 1.2$ pA, and a transmitted ion current of $I_{BOB1} = 0.7$ pA was measured at BOB1. As the readings tended to fluctuate by ≈ 0.2 pA, this results in an efficiency of $\epsilon = 60^{+30}_{-20}\%$. While this is not a precise measurement of the ion guide efficiency, it agrees with the lower limit of $\epsilon = 23\%$ from the discharge test and indicates that the ion guide system

does not pose a large loss mechanism.

Mass Separation

In order to determine the performance of the mass filter mode of the new RFQ ion guide, a series of studies were performed. These included determining the maximum resolving power of the mass filter and measuring the relative efficiency at various resolving powers. Again, ions produced via electric discharge in the gas cell were used for these tests.

"Mass scans" were performed with the ion guide mass filter along several scan lines, $\alpha_{MF} = \frac{U_{DC}}{V_{RF}}$. Figure 5.5 is the result of a mass scan near A = 32 along the scan line $\alpha_{MF} = 15.2\%$. From this scan, it is clear that the mass filter is capable of achieving single mass resolution, which was one of the design goals.
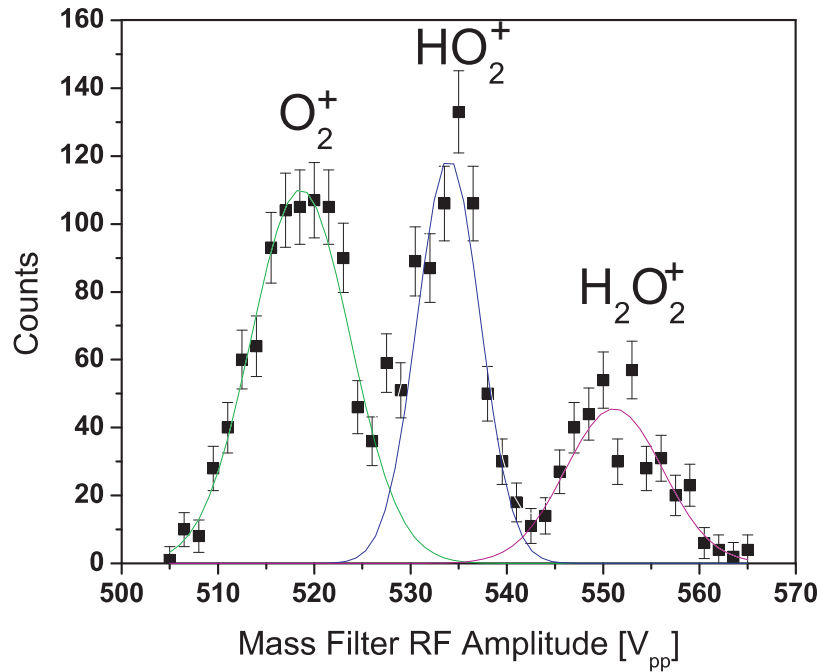
Figure 5.5. Mass scan along the scan line $\alpha_{MF} = 15.2\%$, performed with the LEBIT ion guide mass filter, demonstrating single mass resolution. The mass peaks were unambiguously identified with the Penning trap mass spectrometer.

A systematic investigation of the transport efficiency as a function of the ion guide mass resolution would be straight forward if only one ion species were delivered by the gas cell. Because of the large range of molecular ions in the beam delivered from the gas cell, an additional ion identification is needed. This can be achieved with the help of the Penning trap and the time-of-flight cyclotron resonance detection technique.

The Penning trap mass spectrometer was used to assist in accurately determining the relative efficiency of a given resolving power. As described in 2.2.3, ions which are "resonantly excited" are measured to have a shorter time-of-flight. A software gate can be applied to the time-of-flight of ions detected on the MCP after the ion trap. Using this software gate on the results of a mass scan allows for the separation of "good" ions from "bad".
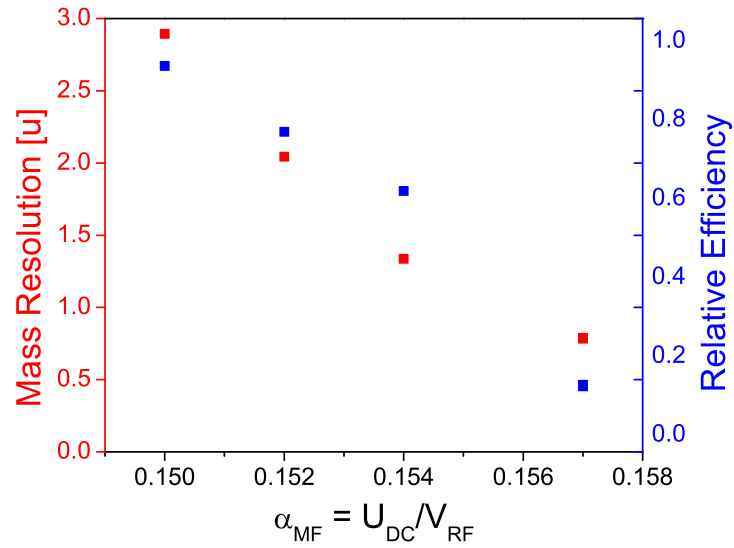
Figure 5.6. Relative efficiency and mass resolution for the LEBIT ion guide mass filter as a function of the mass scan line α_{MF}. These results were obtained using CF_3^+.

A series of mass scans were performed near A = 69 along various scan lines.

For each step along the mass scan, the ions were sent through the LEBIT system and captured in the Penning trap. An RF field with a frequency corresponding to CF_3^+ was applied. The ions were then ejected and the time-of-flight measured. Any CF_3^+ ions captured in the trap would have their cyclotron motion excited by the RF field, resulting in a significantly reduced time-of-flight. Through the application of a software gate applied to the time-of-flight spectrum measured for ions ejected from the Penning trap, it is possible to extract transmission profiles for CF_3^+ along each scan line. The mass resolution for each scan line is then determined by $\Delta m = A \cdot \Delta V / V_{Peak}$, where Δ is the full width of the transmission curve at half maximum and V_{Peak} is the centroid of the highest resolution scan line. The relative efficiency for each scan line is determined by $\epsilon_{Rel} = r_{Peak}/r_{\alpha=0}$ where r_{Peak} is the rate of CF_3^+ detected at V_{Peak} along a given scan line and $r_{\alpha=0}$ is the rate of CF_3^+ detected at V_{Peak} along the $\alpha_{MF} = 0\%$ scan line.

The results of these measurements are presented in Fig. 5.6, as resolving power and relative efficiency as functions of α_{MF}. Based on this data, it is clear that the new ion guide system's performance as a mass filter is greatly enhanced over the original system. Operating the new ion guides at single mass unit resolution results in a relative transmission efficiency of $\approx 50\%$, which is acceptable.

5.2 Beam Purification by Collision Induced Dissociation

After using the mass filter to reduce the contaminants to an ensemble of isobaric molecules, collision induced dissociation (CID) can be used to "reshuffle the deck". CID is a widely applied [90, 91, 92] process in which a collision between an ion and a neutral species results in the conversion of part of the translational energy into internal energy of the ion and subsequent fragmentation of the ion. At LEBIT this

is done using the beam cooler-and-buncher, where the buffer gas in the cooler acts as a gas target.

As the molecular excitation is related to the center-of-mass energy of the collision, it could be assumed that heavier buffer gases would yield improved results. Unfortunately, this must be balanced against possible ion loss from larger recoil energies and RF heating (see chapter 2.1.3). Another means of increasing the center-of-mass energy of the collision is to increase the energy of the ion beam. This can be accomplished by raising the base potential of the LEBIT ion guide system.

In order to study the energy dependence of CID the following test was performed. HCO_2^+ ions were extracted from the gas cell and selected by the mass filter. They were then sent into the beam cooler-and-buncher and subsequently captured in the Penning trap. As in the measurement of mass resolution described earlier, the Penning trap was used to assist in identifying the ions. This was repeated for different ion energies, achieved by adjusting the base potential of the entire ion guide system. Such measurements were performed using both helium and neon as buffer gases in the cooler, in both cases using a pressure of $P \approx 2 \times 10^{-2}$ mbar. As a reference for an ion which does not undergo CID, $^{40}Ar^+$ was chosen and a similar measurement series was performed with neon as the buffer gas in the cooler. The results of these measurements are given in Fig. 5.7.

The count reductions seen above 60 V are likely due to ion guide potential being above the gas cell potential and blocking the ions from entering the ion guides. The loss below 0 V is from the ion guide potential being below the cooler-buncher potential, preventing injection into that system. The data show similar transmission curves for $^{40}Ar^+$ into neon and HCO_2^+ into helium. From the transmission curve for HCO_2^+ into neon, however, it is clear that HCO_2^+ begins to undergo CID when the ion guide base potential is increased above 10 V. At an ion guide base potential of 50 V no reduction is seen in the rate of $^{40}Ar^+$, yet the rate of HCO_2^+ becomes vanishingly small. From

these data it is concluded that by using neon in the cooler and operating the ion guide at a base potential of 60 V a strong reduction of isobaric molecular ions can be expected.
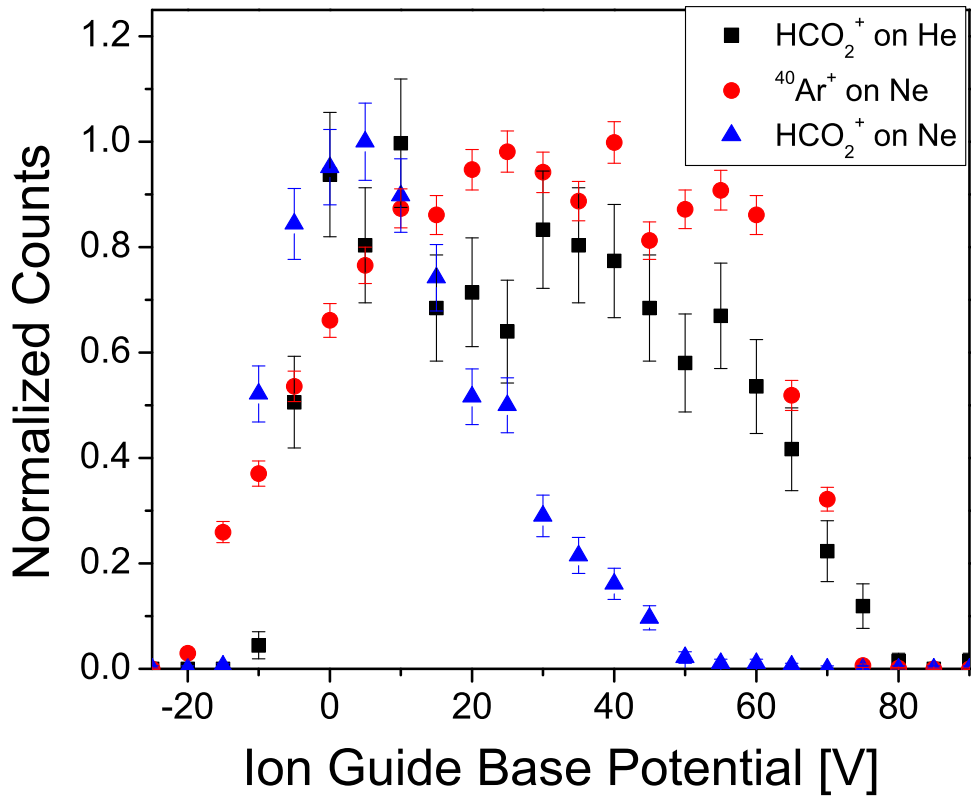
Figure 5.7. Ion transmission through the beam cooler-and-buncher for ^{40}Ar$^+$ and HCO$_2^+$ as a function of ion guide base potential. The trend for ^{40}Ar$^+$ when the beam cooler was operated with neon compared to those for HCO$_2^+$ with the cooler operated with neon and with helium indicate the when using neon, HCO$_2^+$ undergoes CID for sufficiently large ion guide base potential, while when using helium in the beam cooler there is no evidence for HCO$_2^+$ undergoing CID.

A powerful technique for studying CID which is often employed in RFQ mass spectrometry is the so-called MS-MS or MS^n scan. In the LEBIT system, a similar technique can be used – MS-TOFMS. The mass filter is scanned and at each step the time-of-flight spectra after the buncher is recorded.
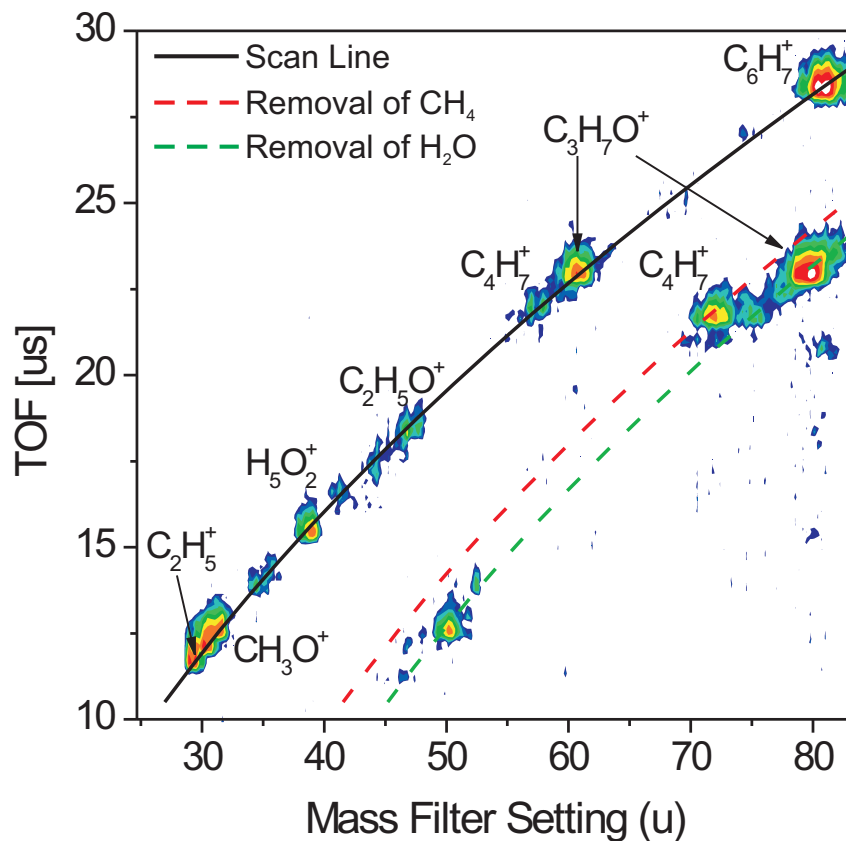
Figure 5.8. Time of flight versus mass scan obtained using helium as a "target" in the LEBIT ion cooler. The solid curve is the scan line, the two dashed curves show where peaks would be if CH_4 or H_2O were lost from the primary ion.

Figure 5.8 shows data from an MS-TOFMS measurement. The ion guides were scanned from A = 30 to A = 100 with a resolution of $\Delta m \approx 2$ u. The beam cooler

was operated with helium. The peaks along the solid curve are molecules which did not dissociate; the peaks along one of the dashed lines have undergone CID and lost a methane or water molecule. The labeled peaks were unambiguously identified using the Penning trap mass spectrometer.

5.3 Time-of-Flight Mass Analysis and Separation

In order to make optimal use of the break-up of molecular ions via CID performed in the beam cooler requires an additional mass filter. While the Penning trap provides a limited mass acceptance, roughly ± 5 u, this is not sufficient to always suppress unwanted CID products. To make optimal usage of CID in the beam cooler, a time-of-flight mass filter was implemented prior to the Penning trap.

The time-of-flight mass filter uses the fact that the beam cooler-and-buncher system is capable of delivering very short ion pulses. This is illustrated in Fig. 5.9, which shows a time-of-flight spectrum measured ≈ 2.5 m after the buncher, with a time of flight resolving power of more than 400.

In order to make use of this time-of-flight separation, an existing beam deflector in the beam line to the Penning trap was used. The deflector consists of a vertical and horizontal pair of short deflection plates used to fine tune the injection into the Penning trap. For realizing a time-of-flight mass separator, one plate is used as a beam gate. It is pulsed using a fast high voltage switch (see Appendix D.4). The nominal deflector voltage of several hundred volts deflects ions such that they are not transported to the Penning trap. When the desired ions pass the deflector, the voltage is reduced to a few ten volts for ≈ 300 ns and the ions are transported to the trap. Figure 5.10 shows normalized transmission curves for several ion species as a function of the time at which the beam gate is opened. As can be seen, the time of flight mass filter effectively suppresses non-isobaric contaminants.
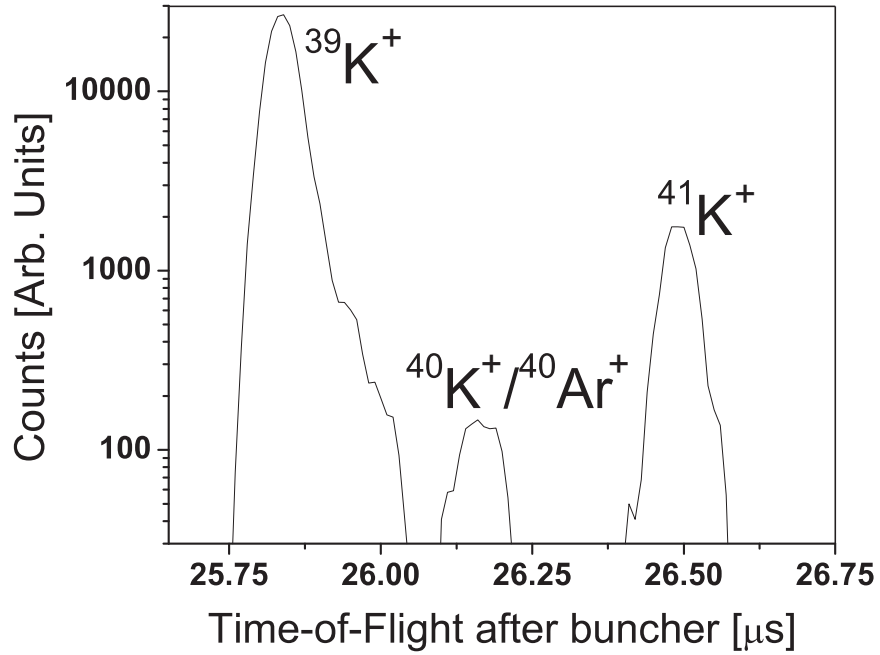
Figure 5.9. Time-of-flight spectrum observed at the beam observation box $\approx$2.5 m after the LEBIT cooler-buncher. The time-of-flight resolving power shown is R> 400.

To test the efficacy of the time-of-flight mass filter for suppressing neighboring masses, Penning trap mass measurements were performed for ^{38}Ar and ^{40}K. Typical resonance curves are given in Fig. 5.11. It is important to note that ^{38}Ar has a natural abundance of only 0.063%, while ^{40}K has a natural abundance of a mere 0.012% of natural Potassium. Being able to obtain these resonance curves demonstrates that the time-of-flight gate provides near complete suppression of non-isobaric ions.
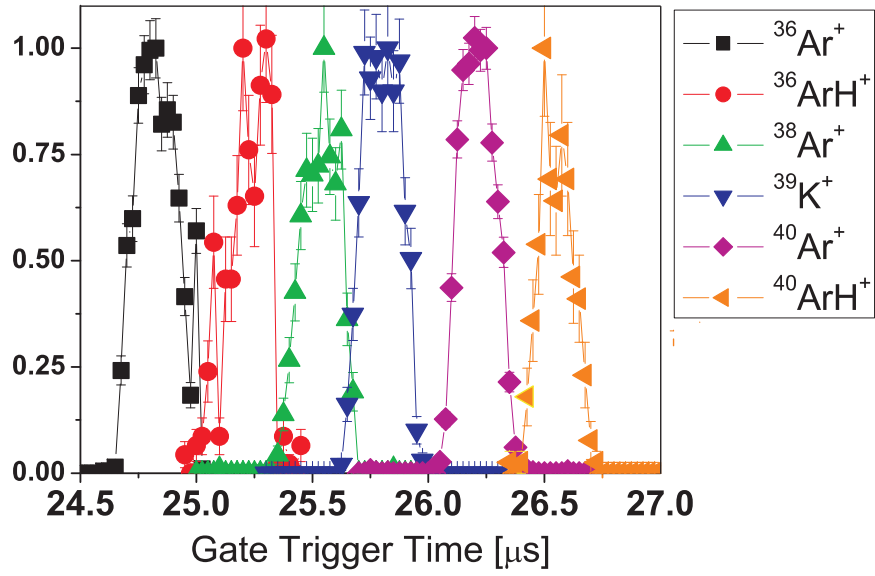
Figure 5.10. Transmission curves for several ion species as a function of time-of-flight mass filter timing.
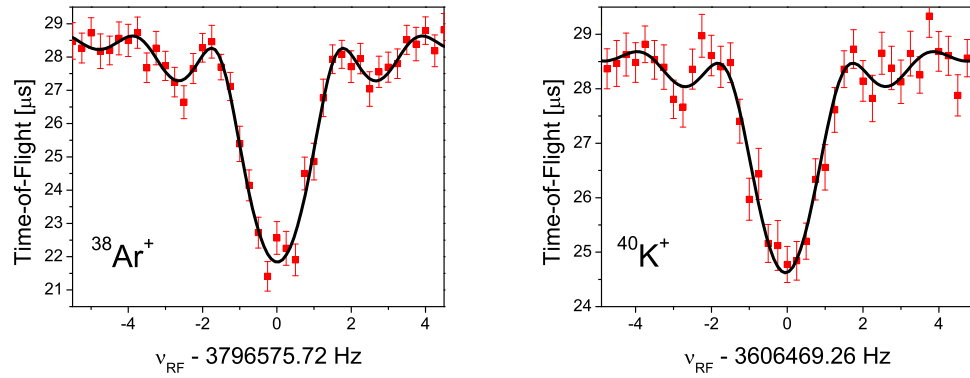
Figure 5.11. Cyclotron resonance curves measured for ^{38}Ar and ^{40}K. Each has a natural abundance of less than 0.1%. Especially in the case of ^{40}K, these measurements would not be possible without mass suppression by the time-of-flight filter.

5.4   In-Trap Contaminant Removal

Any remaining isobaric contaminants can be selectively removed from the Penning trap by the dipole excitation of their ion motion. In this technique, the reduced cyclotron motion of a known contaminant is excited by application of an azimuthal RF dipole field at the ion's reduced cyclotron frequency. With sufficient RF field strength this drives the contaminant ions to large orbits where they no longer interact with the ions of interest and into a region from which they will not be ejected from the trap.

To demonstrate the use of this technique, Fig. 5.12a and b show ions detected after ejection from the Penning trap as a function of frequency of the dipolar RF-field. The scans were made while capturing ions with A = 64. For Fig 5.12a the scan width is $\approx \pm 0.5$ u, centered at the reduced cyclotron frequency for $^{64}\text{Co}^+$. In Fig 5.12b the scan width is $\approx \pm 0.05$ u, centered at the frequency of maximum count reduction found in Fig. 5.12a.

Once the reduced cyclotron frequency of a contaminant is determined with an uncertainty of $\delta\nu < 150$ Hz, quadrupolar excitation can be used to precisely determine the true cyclotron frequency of the contaminant, as shown in Fig. 5.12c. The identity of the contaminant can then be unambiguously determined. Based on the measured cyclotron frequency of the contaminant, in conjunction with a previously determined cyclotron frequency for HC_2F_2^+, the contaminant was determined to be $^{36}\text{ArN}_2^+$.
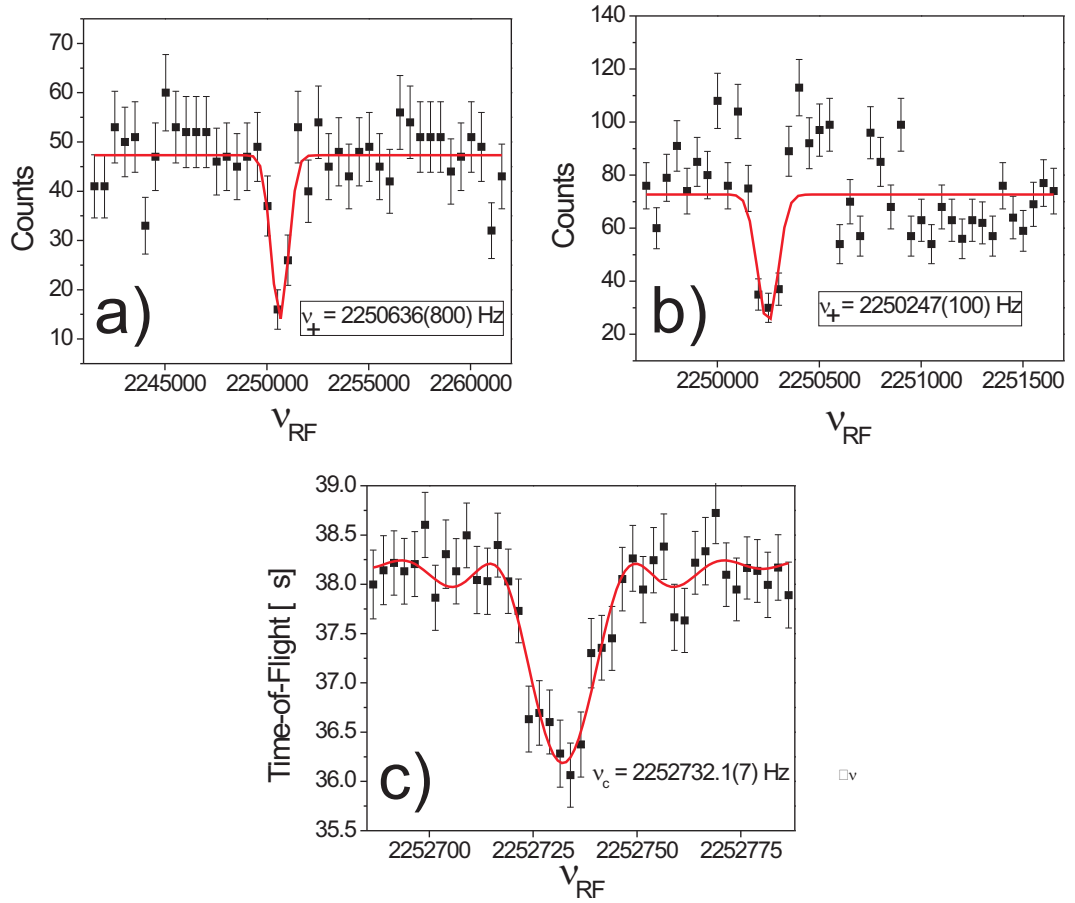
Figure 5.12. (top) Count rate of detected ions ejected from the Penning trap after dipolar excitation as a function of applied RF frequency, ν_{RF}. The left plot centered at the reduced cyclotron frequency of ^{64}Co$^+$ and has a range of $\approx \pm 0.5$ u. The right plot has a range of $\approx \pm 0.05$ u. (bottom) Time-of-flight of ions ejected from the Penning trap after quadrupolar excitation as function of applied RF frequency. The measured cyclotron frequency was found to correspond to ^{36}ArN$_2^+$.

CHAPTER 6

Mass Measurements of Isotopes Near N=Z=33

In the study of nuclear structure along the N=Z line, it is an open question whether there exists a mid-shell restoration [16] of the Wigner energy associated with T=0 n-p pairing [14]. In nuclear astrophysics, the effective stellar lifetimes of the waiting point nuclei ^{64}Ge, ^{68}Se and ^{72}Kr play a large role in determining the rp-process pathway and the composition of neutron star crusts. The precise determination of masses of atomic nuclei with equal and nearly equal numbers of neutrons and protons can be used to determine the effective lifetimes of waiting point nuclei in the rp-process as well as to improve the understanding of neutron-proton pairing.

Prior to the mass measurements performed in this work, the masses of nuclei near N=Z=33 had typical uncertainties of 100 keV or more. Due to the difficulty in obtaining isotopes of Ge, As and Se at ISOL facilities, this region was particular well suited for using the LEBIT facility. In a series of online experiments performed between August 2005 and June 2006, precision mass measurements were performed on ^{63,64}Ga, ^{64,65,66}Ge, ^{66,67,68}As and ^{69}Se. These LEBIT results have been recently published [11].

6.1 Experimental Procedure

Many steps are required in order to perform mass measurements at the LEBIT facility. The isotope of interest must be selected using the A1900 fragment separator, then thermalized in the gas cell. The ion beam extracted from the gas stopping cell is guided through a differentially pumped region and then transported to the beam cooler-and-buncher. Cold ion bunches are transported from the cooler-and-buncher to the Penning trap where mass measurements are performed. Along the way from the gas cell to the Penning trap, the ion beam undergoes multi-step beam purification as described in the previous chapter.

6.1.1 Rare Isotope Production and Stopping

Fast projectile fragmentation of ^{78}Kr at 140 MeV/A was used to create neutron-deficient isotopes near N=Z=33. The A1900 fragment separator [43] was used to select the isotopes of interest for each measurement. The A1900 generally provides isotonic "cocktail" beams. Three such cocktail beams have been used for these measurements: (^{66}As, ^{65}Ge, ^{64}Ga), (^{67}As, ^{66}Ge, ^{65}Ga), and (^{69}Se, ^{68}As, ^{67}Ge).

As discussed in chapter 3, the energy of the beams are initially degraded using flat, rotatable glass degraders before being thermalized in the gas cell. Based upon the Z-dependence of the stopping power, the degrader thickness was adjusted to provide optimized stopping for each isotope, verified through stopping range measurements and subsequent activity measurements of the extracted beam. The procedure is described in detail in [75].

6.1.2 Radio-Molecular Identification

In previous experiments it was found that ^{38}Ca formed water adduct molecular side-bands of $[^{38}Ca(H_2O)_n]^{2+}$ with n = {1,2,3,4} [9]. Therefore, after optimizing beam

stopping and extraction from the gas cell, the molecular form of the desired isotope needed to be determined. Using the mass filter and one of the β-detectors, activity measurements were performed at a number of points along a scan line. Figure 6.1 shows the results of mass-versus-activity scans for ^{65}Ge and ^{67}As. For ^{65}Ge, the activity peaked at A/Q = 66, while for ^{67}As the activity peaked near A/Q = 71.
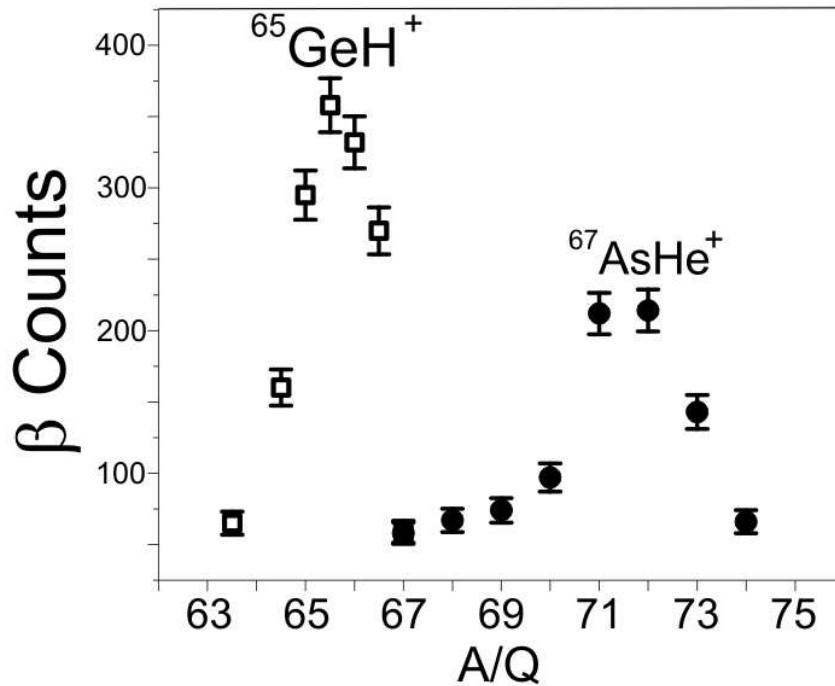
Figure 6.1. Counts recorded with a β-detector after the ion guide mass filter as a function of A/Q. See text for explanation of molecular assignment.

With the Penning trap operated in a direct transmission mode, the molecular state of the rare isotopes after ejection from the beam cooler-and-buncher can be determined by measuring activity at the β-detector following the Penning trap as a function of the time-of-flight mass filter setting. From activity scans with this scheme, it was found that ^{65}Ge was ejected from the buncher with A/Q = 66, while ^{67}As was

ejected with $A/Q = 67$. With the Penning trap mass spectrometer it was verified that ^{65}Ge was provided after the buncher as ^{65}GeH$^+$ while ^{67}As arrived as ^{67}As$^+$. It is inferred that the arsenic was extracted from the gas cell with a helium adduct and probably not as AsH$_4^+$. In similar measurements, Se and Ga were found to be delivered from the gas cell as Se$^+$ and Ga$^+$.

6.1.3 Beam Purification

As has been discussed in chapter 5, before Penning trap mass spectrometry can be performed on rare isotopes extracted from the gas cell, a multi-step beam purification system must be used to remove contaminant ions. The first step is to set the mass filter to the A/Q at which the rare isotopes are extracted from the gas cell.

The second beam purification step is CID in the beam cooler. For arsenic isotopes, which were determined to be extracted with a weakly bound helium adduct, the cooler was operated with helium, which was found to be sufficient for removing the adduct while minimizing CID of other molecules. For the other isotopes, neon was used in the buncher to provide maximum CID of contaminant molecular ions. In this way, maximum separation of the rare isotope ion from contaminants is achieved. In the third step, the time-of-flight mass separator is set to allow transmission of the A/Q at which the rare isotopes are ejected from the buncher.

The final step in the beam purification process is the determination of any isobaric contaminants yet remaining after TOFMS. The high resolving power of the LEBIT Penning trap system allows for unambiguous determination of contaminants, as discussed in chapter 5.4. After the contaminants are identified, they are removed from the trap via excitation of their cyclotron motion at ν_+, the reduced cyclotron frequency.

Table 6.1. Contaminant ions removed in-trap prior to cyclotron frequency measurements. No atomic mass is given for the most abundant stable isotope of an element.

Species	Contaminants				
$^{63}\mathrm{Ga}^+$	$\mathrm{C}_4^{13}\mathrm{CH}_3^+$	$\mathrm{C}_4^{13}\mathrm{CH}_2^+$	$\mathrm{C}_5\mathrm{H}_2^+$	$\mathrm{C}_5\mathrm{H}_3^+$	$\mathrm{C}_5\mathrm{H}_4^+$
$^{64}\mathrm{Ga}^+$	$\mathrm{C}_4^{13}\mathrm{CH}_3^+$	$\mathrm{C}_4^{13}\mathrm{CH}_2^+$	$\mathrm{C}_5\mathrm{H}_3^+$	$\mathrm{C}_5\mathrm{H}_4^+$	$\mathrm{C}_5\mathrm{H}_5^+$
$^{64}\mathrm{GeH}^+$	$^{65}\mathrm{Cu}^+$	$\mathrm{C}_2\mathrm{F}_2\mathrm{H}_3^+$	$\mathrm{C}_4^{13}\mathrm{CH}_3^+$	HSO_2^+	$\mathrm{C}_5\mathrm{H}_6^+$
$^{65}\mathrm{GeH}^+$	$\mathrm{C}_5\mathrm{H}_5^+$	HSO_2^+	$\mathrm{C}_5\mathrm{H}_7^+$	$\mathrm{C}_5\mathrm{H}_6^+$	$\mathrm{C}_4^{13}\mathrm{CH}_3^+$
$^{66}\mathrm{GeH}^+$	$\mathrm{C}_5\mathrm{H}_6^+$	$\mathrm{C}_5\mathrm{H}_7^+$	$\mathrm{C}_5\mathrm{H}_8^+$	$\mathrm{C}_4^{13}\mathrm{CH}_6^+$	HSO_2^+
$^{66}\mathrm{As}^+$	$\mathrm{C}_5\mathrm{H}_5^+$	$\mathrm{C}_5\mathrm{H}_6^+$	$\mathrm{C}_5\mathrm{H}_7^+$	CF_3^+	HSO_2^+
$^{67}\mathrm{As}^+$	CF_3^+	$\mathrm{C}_5\mathrm{H}_5^+$	HSO_2^+	$\mathrm{C}_5\mathrm{H}_7^+$	
$^{68}\mathrm{As}^+$	$^{69}\mathrm{Se}^+$	CF_3^+	$\mathrm{C}_5\mathrm{H}_6^+$	$\mathrm{C}_5\mathrm{H}_7^+$	$\mathrm{C}_5\mathrm{H}_7^+$
$^{69}\mathrm{Se}^+$	$\mathrm{C}_5\mathrm{H}_7^+$	$\mathrm{C}_5\mathrm{H}_8^+$	$\mathrm{C}_5\mathrm{H}_9^+$	CF_3^+	
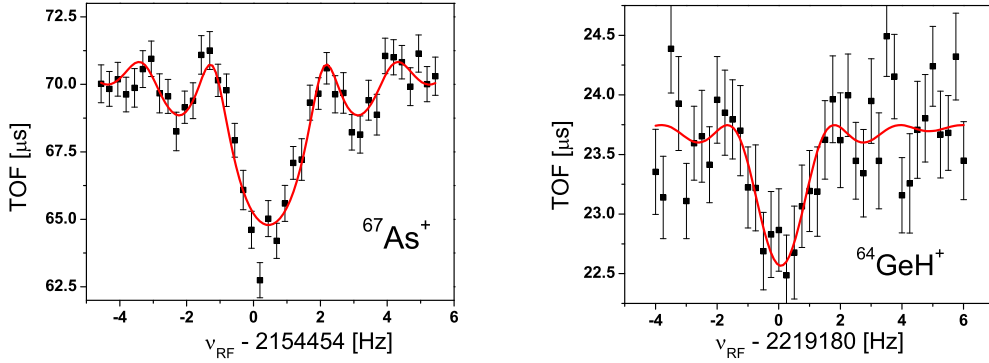
Figure 6.2. Left: Time of flight versus excitation frequency for $^{67}\mathrm{As}^+$ ions ejected from the Penning trap after a 500 ms quadrupolar excitation. The solid line is a fit of the theoretical line shape [66] to the data. Right: Similarly for $^{64}\mathrm{GeH}^+$ ions.

6.1.4   Determination of the Ion Cyclotron Frequency

After being captured in the trap, ions are initially exposed to an azimuthal dipole RF-field for, typically, 10 - 20 ms. This dipolar RF-field is generated by the superposition of the signals from up to six frequency generators, each operated at the reduced cyclotron frequency of a known (or suspected) contaminant. This selectively removes those contaminant ions from the trap by increasing the amplitudes of the their cyclotron motion [64]. The ions are then exposed to a quadrupolar RF-field

of frequency ν_{RF} for a duration T_{RF} before being ejected from the trap. The mean time-of-flight of ejected ions to an MCP detector is plotted as a function of ν_{RF} to determine the ion's cyclotron frequency.

For these measurements, excitation times in the range of $T_{RF} = 200$ ms to 500 ms were generally used. As an exception, due to its short half-live ($T_{1/2} = 96$ ms), an excitation time of 50 ms was used for ^{66}As. In order to minimize systematic effects from ion-ion interactions, the number of ions in the trap was kept low, in nearly all cases less than 5 detected ions per trapping cycle. Table 6.2 lists the isotopes studied in the five different beam times, together with the reference ion and the mean number of ions detected per cycle for each isotope measured.

Figure 6.2 shows typical cyclotron resonance curves obtained for ^{67}As$^+$ and ^{64}GeH$^+$. From the fit of the theoretical curve [66], the center frequency is obtained, which corresponds to the cyclotron frequency, ν_c, of the ion. A total of 62 resonance curves were obtained for rare isotopes in the course of this work.

For the determination of the magnitude of the magnetic field cyclotron resonance curves were obtained for an ion species with well-known mass before and after obtaining each cyclotron resonance curve for the species of interest and interpolating the value of the magnetic field during the measurement of the species of interest. In the measurements reported herein, a number of different reference ions were used. Krypton and rubidium isotopes were obtained from the test ion source, while the other molecular ions were obtained from the gas cell.

6.2 Data Evaluation

The primary data from Penning trap mass measurements are the cyclotron frequency ratios, $R = \nu_c/\nu_{c,ref}$, where ν_c is the cyclotron frequency of the species of interest and $\nu_{c,ref}$ is the cyclotron frequency of the reference species. For each measurement,

Table 6.2. Isotopes studied, references ions used, mean number of ions detected per cycle and total number of resonance curves measured during 5 online experiments.

Experiment Run #	Species	Reference	$\overline{ions}$/cycle	Number of Measurements
1	$^{67}\text{As}^+$	$^{86}\text{Kr}^+$	1.2	5
2	$^{67}\text{As}^+$	$^{86}\text{Kr}^+$	0.6	1
3	$^{67}\text{As}^+$	$^{85}\text{Rb}^+$	0.5	15
2	$^{65}\text{GeH}^+$	C_5H_5^+	2.3	14
3	$^{65}\text{GeH}^+$	$^{85}\text{Rb}^+$	0.6	3
4	$^{65}\text{GeH}^+$	C_5H_2^+	0.6	1
3	$^{66}\text{As}^+$	$^{85}\text{Rb}^+$	0.002	4
5	$^{66}\text{GeH}^+$	C_5H_5^+	0.8	4
5	$^{68}\text{As}^+$	CF_3^+	0.2	3
5	$^{69}\text{Se}^+$	CF_3^+	0.6	5
5	$^{64}\text{GeH}^+$	HSO_2^+	0.5	3
5	$^{64}\text{Ga}^+$	C_5H_2^+	2.4	3
5	$^{63}\text{Ga}^+$	C_5H_2^+	2.0	1

the cyclotron frequency is determined by fitting the analytical time-of-flight cyclotron resonance line shape [66] to the data. The mass of the species of interest is extracted from the cyclotron frequency ratio using $M = R \cdot (M_{ref} - m_e) + m_e$, where m_e is the mass of an electron. The values for m_e and M_{ref} are taken from the 2003 Atomic Mass Evaluation (AME'03) [93]. In principle, the difference in ionization potentials of the reference and species of interest should be taken into account, but within the uncertainties of the measurements presented herein they were all negligible.

In order to account for decay of the magnetic field between measurements, each measurement of the species of interest was bracketed by two reference measurements. The reference frequency used for the frequency ratio, $\nu_{c,ref}$, was interpolated from the references taken before, $\nu_{c,ref1}$, and after, $\nu_{c,ref2}$, the measurement of the species of interest. The reference frequency is calculated with a linear interpolation as:

$$\nu_{c,ref} = \nu_{c,ref1} - (\nu_{c,ref1} - \nu_{c,ref2}) * \frac{t_m - t_1}{t_1 - t_2} \qquad (6.1)$$

where t_1, t_2, and t_m are the mean time of the anterior reference, posterior reference

and measurement, respectively. The mean time refers to the time halfway between the start and end of a measurement. The statistical uncertainty associated with the frequency ratio is given by standard propagation of errors techniques.

Sources of systematic error include nonlinear decay of the magnetic field, cyclotron frequency shifts from ion-ion interactions [94] and mass dependent effects due to trap imperfections [68]. Data taken during the measurement of ^{38}Ca [9] demonstrated that the nonlinear decay of the magnetic field of the LEBIT spectrometer was negligible on the 10 ppb level when reference measurements are performed at intervals of less than 2 hours. In that measurement it was determined that the largest non-linear effect was associated with fluctuations in the cryostat pressure. Since that time, a PID loop to regulate the cryostat pressure has been implemented, further reducing non-linear changes in the magnetic field. Thus any effects from a non-linear term in the decay were ignored, since reference measurements were taken on intervals of, typically, 30 - 60 minutes except in the case of ^{66}As, where the typical intervals were 3 - 4 hours. A statistical uncertainty of $\delta m/m \approx 10^{-7}$ was achieved, compared to which any systematic uncertainty from non-linear field decay is negligible.

To probe possible mass dependent systematic effects, during one of the runs a set of three mass measurements of ^{39}K$^+$ was made using ^{85}Rb$^+$ as a reference. The results from these data indicate a mass dependent systematic error term of $\delta m/m = 5(5)\text{x}10^{-10}/\Delta u$, where Δu is the mass difference between measured and reference ions in atomic mass units. For use in the data analysis, a value of $\delta m/m = 5\text{x}10^{-10}/\Delta u$ has been adopted as the maximum mass dependent systematic uncertainty.

Frequency shifts that may be caused by ion-ion interactions were investigated by performing a counting rate analysis. For each data set with a sufficient distribution of counting rates, including reference measurements, the data were sorted into bins by number of detected ions. Cyclotron frequencies were determined for each counting rate bin. Using a linear fit to these data, and taking the detector efficiency into

Table 6.3. Mean frequency ratios obtained for each set of measurements presented in this thesis. Values were derived from counting rate analyzed data (see text) wherever possible. Listed uncertainties are statistical. In the case of ^{66,68}As the listed uncertainty has been increased to account for a large Birge ratio (see text).

Nuclide	Reference	Frequency Ratio
^{63}Ga	^{12}C$_5$H$_2$	1.01489389(11)
^{64}Ga	^{12}C$_5$H$_2$	1.030979398(44)
^{64}GeH	H^{32}S^{16}O$_2$	0.99688922(62)
^{65}GeH	^{12}C$_5$H$_5$	1.013961997(66)
^{65}GeH	^{12}C$_5$H$_2$	1.063396513(69)
^{65}GeH	^{85}Rb	0.776653759(73)
^{66}GeH	^{12}C$_5$H$_5$	1.029252824(40)
^{66}As	^{85}Rb	0.77661811(38)
^{67}As	^{86}Kr	0.779171859(34)
^{67}As	^{86}Kr	0.77917095(35)
^{67}As	^{85}Rb	0.788337366(20)
^{68}As	^{12}C^{19}F$_3$	0.984659141(81)
^{69}Se	^{12}C^{19}F$_3$	0.999191318(23)

account, the cyclotron frequency of a single trapped ion was determined. In some cases with insufficient statistics, this analysis could not be performed. Such was the case for all measurements of ^{66}As and ^{68}As as well as all measurements from the second run with ^{67}As and most measurements of ^{69}Se.

While there is no clear evidence that these measurements suffer any frequency shifts due to ion-ion interactions, to be conservative the count-rate adjusted data, which have a somewhat larger statistical uncertainty, have been used when available. Table 6.3 lists the mean frequency ratio for each set of measurements, with the statistical uncertainty listed in parenthesis.

In the cases of ^{66,68}As, the Birge ratios [95] – the ratio of outer error to inner error – were found to be 1.7(2) and 1.8(3), respectively, indicating that the uncertainties of the individual measurements were underestimated. In all other cases the data sets had Birge ratios of $\lesssim$ 1. To be conservative, in the case ^{66,68}As the outer error is used instead of the inner error, i.e. the uncertainties listed in Table 6.3 is increased by a factor equal to the Birge ratio.
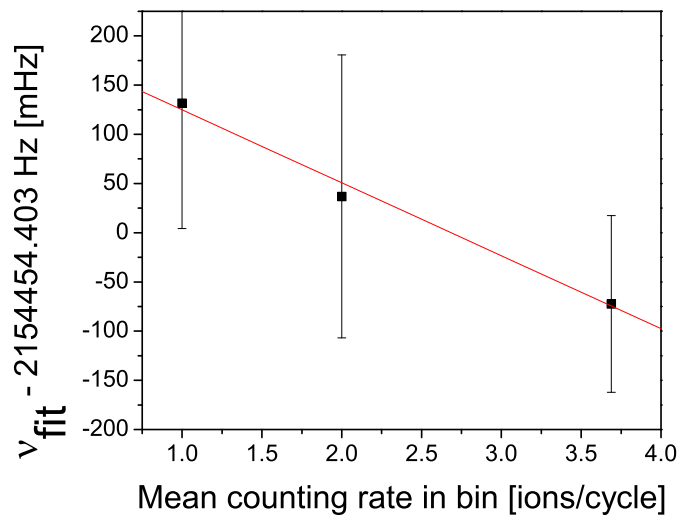
Figure 6.3. Example of count rate analysis of ^{67}As$^+$ cyclotron frequency measurement. In this example, the fit to the raw data yielded $\nu_C = 2154454.403(65)$ Hz, while extrapolation to one detected ion yielded $\nu_C = 2154454.54(13)$ Hz.

Table 6.4. Mass excess values obtained in this work. The values from the 2003 Atomic Mass Evaluation and their deviation from values obtained in this work are listed for comparison. The column ME_{Other} lists measurements from other groups which were not included in the 2003 Atomic Mass Evaluation. All values are given in keV.

Species	ME_{LEBIT}	$ME_{AME'03}$	ME_{Other}		ME_{LEBIT} - $ME_{AME'03}$
^{63}Ga	-56545.4(6.3)	-56547.1(1.3)			1.7(6.4)
^{64}Ga	-58832.6(2.5)	-58834.3(2.0)	-58832.5(3.9)	[96]	1.7(3.2)
^{64}Ge	-54315.7(3.8)	-54350(30)	-54344(30)	[96]	-34(30)
^{65}Ge	-56480.6(1.2)	-56410(100)			71(100)
^{66}Ge	-61607.0(2.4)	-61620(30)			-13(30)
^{66}As	-52018(30)	-51500(680)	-52057(50)	[97]	518(681)
^{67}As	-56586.0(1.1)	-56650(100)			-64(100)
^{68}As	-58896.2(5.3)	-58900(40)	-58894.4(3.1)	[98]	-4(40)
^{69}Se	-56434.6(1.5)	-56300(30)			135(30)

6.3 Results and discussion

6.3.1 Atomic Masses

In order to simplify discussions of atomic masses is it common to make use of the "mass excess." The mass excess, ME, is given by

$$ME = M(^A Z) - A \cdot \frac{M(^{12}C)}{12}, \qquad (6.2)$$

where M is the atomic mass.

The mass excesses determined in the present work for ^{63,64}Ga, ^{64,65,66}Ge, ^{66,67,68}As and ^{69}Se are given in Table 6.4. These are based on the weighted mean of the mass excesses obtained from the individual frequency ratios given in Table 6.3. An additional error of $\delta m/m = 5 \times 10^{-10}$/u was included in cases with non-isobaric reference ions to account for possible mass dependent effects. The mass value for the reference ions are based on values listed in the 2003 Atomic Mass Evaluation (AME'03) [93]. For the Ge isotopes, which were measured as GeH$^+$, the mass excess values listed have been obtained by subtracting the hydrogen mass excess from the molecular mass excess, $ME(^A\text{Ge}) = ME(^A\text{GeH})$ - $ME(\text{H})$.

The new measurements are within 1-σ deviation of the values listed in AME'03, with the exception of ^{69}Se (-4.5σ) and ^{64}Ge (+1.1σ). In particular, the new values are in excellent agreement with recent Penning trap measurements from other facilities. For instance, mass measurements of ^{63,64}Ga [99] recently performed at ISOLDE/CERN with ISOLTRAP [32] and already included in AME'03 agree with our values. Also, while our value for the mass of ^{64}Ge has a much higher precision than previous measurements it agrees with recent measurements made with the CPT at Argonne National Lab [100], as does our value for ^{68}As [98].

The isotopes ^{64,65}Ge, and ^{66,67}As have previously been measured via time-of-flight mass spectrometry using SPEG at GANIL [25]. Figure 6.4 (top) compares our mass excess values for these four isotopes with values from SPEG. Figure 6.4 (bottom) compares the mass excess values presented in this work with values from the literature. The data are divided into two graphs to simplify comparisons, as the scale of uncertainties, and the deviations from our measured values, for the four data points from SPEG [25] are larger in comparison to the rest of the data.
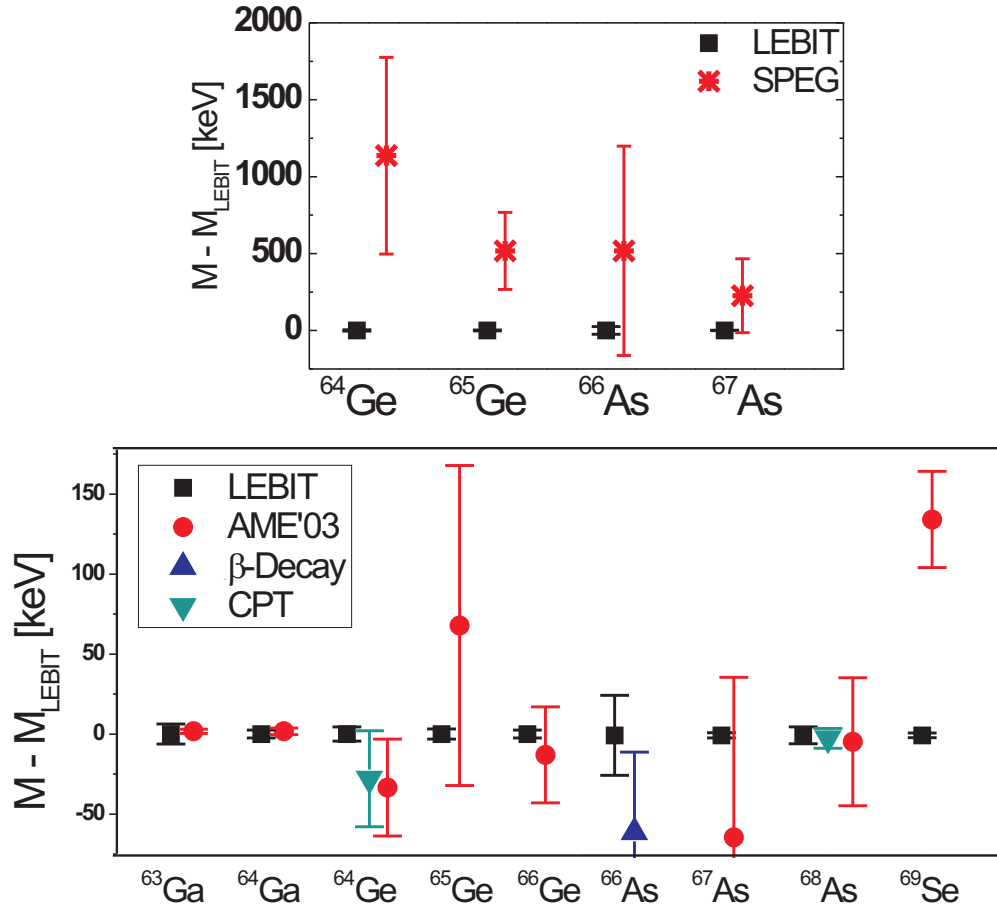
Figure 6.4. Comparison of mass values obtained in this work with literature values from AME'03 [93], time-of-flight measurements with SPEG [25], Penning trap measurements from CPT [100] and a β end-point measurement [97].

Table 6.5. Mass excess values for select N<Z nuclei as calculated using Coulomb displacement energies [19] and the mass excess values of mirror nuclei, compared with Audi-Wapstra extrapolations from AME'03 [93]. All values are in keV.

Species	$ME_{This\ Work}$	$ME_{AME'03}$	Deviation
^{63}Ge	-46948(100)	-46910(200)	38(224)
^{64}As	-39517(100)	-39520(360)	-3(374)
^{65}As	-46772(100)	-46980(300)	-208(316)
^{66}Se	-41833(100)	-41720(300)	113(316)
^{67}Se	-46548(100)	-46490(200)	58(224)
^{68}Br	-38624(100)	-38640(360)	-16(374)
^{69}Br	-46264(100)	-46480(110)	-216(149)

As can be seen from Fig. 6.4, the SPEG values overlap the present values for the heavier isotopes, but not for the lighter ones. It appears that the SPEG masses may suffer from a systematic bias. This may be related to their use of ^{69}Se as a reference mass. The mass of ^{69}Se was previously determined in two ^{69}Se$(\varepsilon p)^{68}$Ge decay studies [101, 102]. While they are consistent with each other, they differ from our mass excess values by more than 4σ. Also, it is worth noting that the ^{66}As β-decay study of Davids et al. [97], which has been disregarded in previous editions of the Atomic Mass Evaluation due to discrepancies with expected S_{2n} values, agrees with the Q_β value derived from the present measurements.

6.3.2 Mass Predictions from Coulomb Displacement Energies

New predictions for the masses of the nuclei ^{63}Ge, ^{64,65}As, ^{66,67}Se and ^{68,69}Br, as shown in Table 6.5, were obtained using Coulomb displacement energy calculations from Brown et al. [19] with mass values for the mirror nuclei obtained in this work. The uncertainty of the Coulomb displacement is estimated to be 100 keV, which makes the present experimental mass measurement uncertainties negligible in making these estimates.

6.3.3   Neutron-Proton Pairing Energy: V_{np}

Neutron-proton (np) pairing effects are expected to be maximized in N=Z nuclei, due to the fact that the valence neutrons and protons occupy the same shell model orbits. Interest in np pairing has grown in recent years as radioactive ion facilities have been able to reach ever heavier N=Z nuclei. An open question is how the np pairing energy behaves beyond Z=28. It has been suggested by Jänecke [103] that the pairing energy should be a function of $\sqrt{A}$, while Van Isacker [16] suggested that the pairing energy should be broken by large angular momenta and Coulomb interactions in heavier sd-shell nuclei, but could possibly be restored in nuclei beyond ^{56}Ni by a pseudo-SU(4) symmetry in the pf-shell.

The np pairing energy, V_{np}, for N=Z nuclei can be extracted from nuclear binding energies, B, of a set of neighboring nuclei using the empirical formula [16]

$$V_{np} = [B_{N,Z} - B_{N-1,Z}] - [B_{N,Z-1} - B_{N-1,Z-1}] \qquad (6.3)$$

For N=Z nuclei beyond ^{74}Rb, the mass values required for calculating V_{np} have not been measured. For ^{66}As and ^{70}Br the necessary mass values have had very large uncertainties or were only estimates. The new mass measurements can be used to reduce the uncertainty in V_{np} for both of these nuclei.

Table 6.6 lists the calculated np pairing energy based on mass values presented in this work compared with those calculated from literature values. The masses of Z = N+1 nuclei required for eq. 6.3 were calculated using Coulomb displacement energies and measured mirror nuclei masses. $V_{np}(^{70}$Br) was calculated using the Audi-Wapstra extrapolated mass value of ^{70}Br [93] in the first two columns of Table 6.6. It is found that the Wigner energy for ^{66}As is shifted by -620 keV, but still within the large uncertainty of the prior value while the value of $V_{np}(^{70}$Br) is shifted by -100(550) keV.

A measurement of the β-decay Q-value of ^{70}Br reported by Davids et al. [97] has

Table 6.6. Neutron-proton pairing energies for ^{66}As and ^{70}Br. In the first column, values are calculated using mass values from AME'03. In the second column, values presented in this work when available, otherwise using AME'03. In the third column, values are calculated as in column two except the mass of ^{70}Br is from Davids et al. [97]. All values are in keV.

	AME'03	This Work + AME'03	This Work + AME'03 + Davids
^{66}As	-2460(750)	-3080(100)	–
^{70}Br	-2860(450)	-2960(330)	-3610(210)

long been excluded from the Atomic Mass Evaluation based on disagreement with the expected two-neutron separation energies. As no other data on the mass of ^{70}Br has been published, the result from [97] is included for completeness. Doing so, it is found that $V_{np}({}^{70}\text{Br})$ shifts by -750(490).

Figure 6.5 shows the neutron pairing energy for odd-odd N=Z nuclei up to ^{74}Rb. As this figure demonstrates, based on our new data, there is an indication of a trend towards the re-strengthening of V_{np}. Mass measurements of heavier N=Z nuclei are required to clarify this trend.

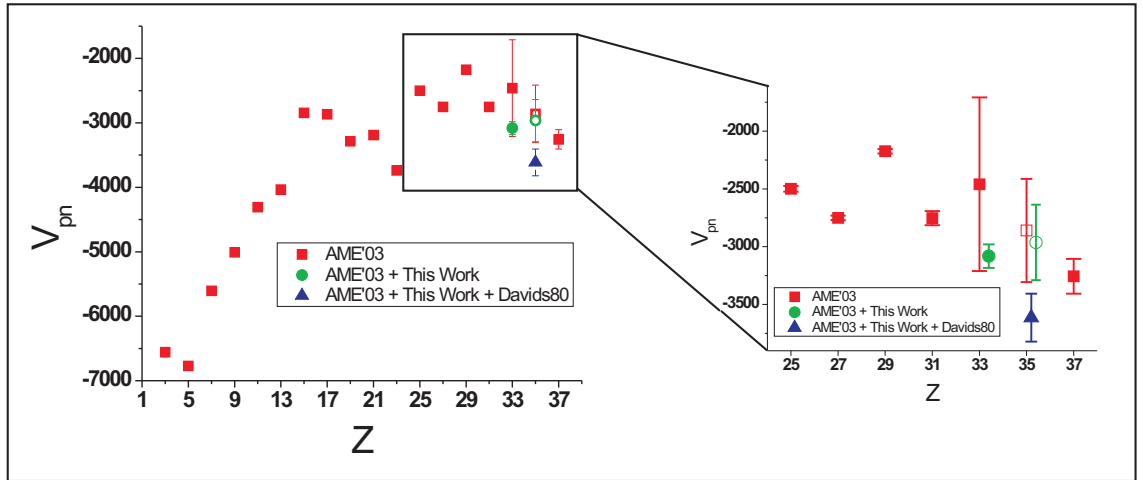Figure 6.5. Neutron-proton pairing energies as function of Z for odd-odd N=Z nuclei up to ^{74}Rb. Open points incorporate AME'03 systematics. Closed points use only experimental data and Coulomb Displacement Energy calculations. Davids80 refers to [97].

Table 6.7. Reaction Q-values used for network calculations to determine the effective lifetimes of ^{64}Ge and ^{68}Se. Values were derived from mass measurements and Coulomb displacement energies reported herein or derived from AME'03 [93] values as noted. All values in keV.

Reaction	This work	AME'03
^{64}Ge(p,γ)^{65}As	-255(104)	-354(172)
^{65}As(p,γ)^{66}Se	2350(200)	2433(246)
^{68}Se(p,γ)^{69}Br	-679(119)	-463(129)
^{69}Br(p,γ)^{70}Kr	2450(216)	2234(227)

6.3.4 rp-Process

The even-even N=Z nuclei ^{64}Ge,^{68}Se and ^{72}Kr could be important waiting point nuclei in the astrophysical rp-process. The reasons are their relatively long half-lives as compared to the rp-process timescale of 10 - 100 s and the reduced proton binding energies of the odd-Z nuclei ^{65}As, ^{69}Br and ^{73}Rb. However, depending on the actual proton capture Q-values, the delay caused by these waiting points can be decreased below their β-decay lifetimes by sequential 2p capture [4, 20].

Using the present mass measurements, along with the mass estimates from the Coulomb Displacement Energy, the proton capture Q-value uncertainties can be reduced for some of the nuclei which determine the effective lifetimes of the waiting point nuclei ^{64}Ge and ^{68}Se. For ^{64}Ge, the data yield a proton capture Q value, $Q_p = $ M(^{64}Ge) + M(p) - M(^{65}As), of -255(104)keV. Similarly, ^{69}Br is found to be 216(150) keV more unbound than the value used in [98], further weakening proton capture on ^{68}Se. Table 6.7 provides a comparison of the Q-values from the present mass measurements with previous values.

The reaction networks shown in Fig. 6.6 were used in determining the effective lifetimes of the waiting point nuclei ^{64}Ge and ^{68}Se. Network calculations were performed using code written by Hendrik Schatz. For these calculations a starting abundance of only the waiting point nuclide and protons, with the protons accounting for 70.5% of

the mass fraction, corresponding to the solar value, was used. Furthermore a density of 10^6 g/cm^3 was held constant in the calculations. Forward - (p,γ) - reaction rates were taken from [104], while reverse - (γ,p) - reaction rates were determined through detailed balance using the new Q-values presented. The change in the calculated forward rates due to the new Q-values were neglected as such changes are small compared to typical uncertainties in the Hauser-Feshbach reaction rate calculations. The temperature range used in these calculations was chosen to be $T_9 = 0.5$, 2.2 GK since proton capture is ineffective for the high-Z nuclei considered here at temperatures below about 1 GK, while proton emission via photodisintegration inhibits proton capture at temperatures above 1.8 GK [20]. The effective lifetime was defined as the time required to convert 50% of the initial seed nuclei beyond its one-proton capture product.
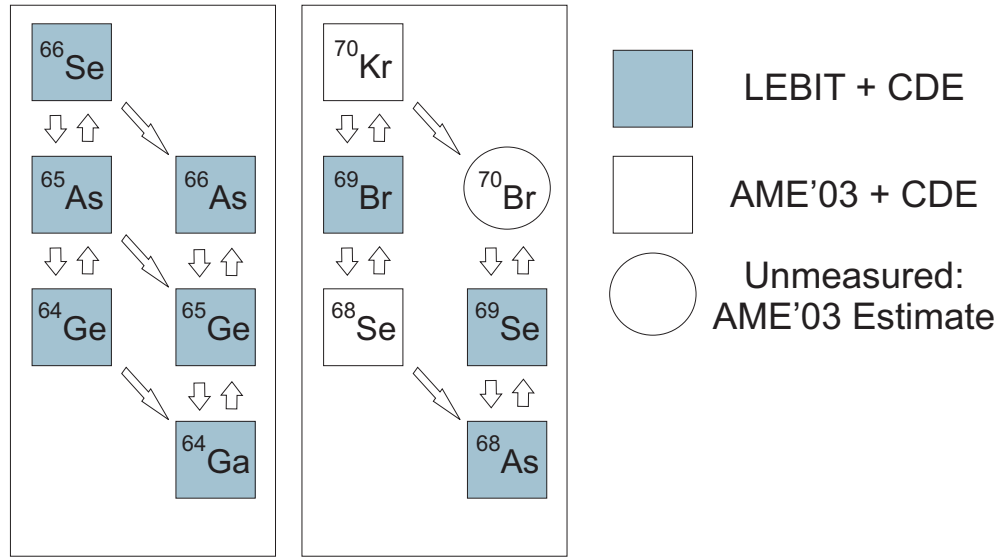
Figure 6.6. Reaction networks used for the calculations of effective lifetimes for ^{64}Ge (left) and ^{68}Se (right). Also indicated is the source of the mass excess values used in the calculation. CDE refers to Coulomb displacement energy.

The results of these calculations are shown in Fig. 6.7. The open envelope represents the temperature dependance of the effective lifetimes based on 1-σ indepen-

dent variations of all masses involved in the network using AME'03 values and CPT [98, 100] data for ^{64}Ge and ^{68}Se. The filled area similarly depicts lifetimes using AME'03 and LEBIT data. Clearly, the LEBIT results considerably reduce the uncertainty in the effective lifetime of the two major waiting points, ^{64}Ge and ^{68}Se, in the rp-process. For ^{64}Ge the LEBIT results suggest that the waiting point can be bridged for a wider temperature range than previously believed. On the other hand, ^{68}Se causes a greater delay than previous data would have suggested. The significant shift in the temperature dependance of the lifetime of ^{68}Se is due to a 134 keV discrepancy found in the mass of ^{69}Se, resulting in the correspondingly large shift in $Q_p(^{69}$Br$)$ as shown in Table 6.7. These calculations also depend on the proton capture rates of ^{65}As and ^{69}Br, currently based on Hauser-Feshbach calculations [104] which can be very uncertain near the proton drip-line.
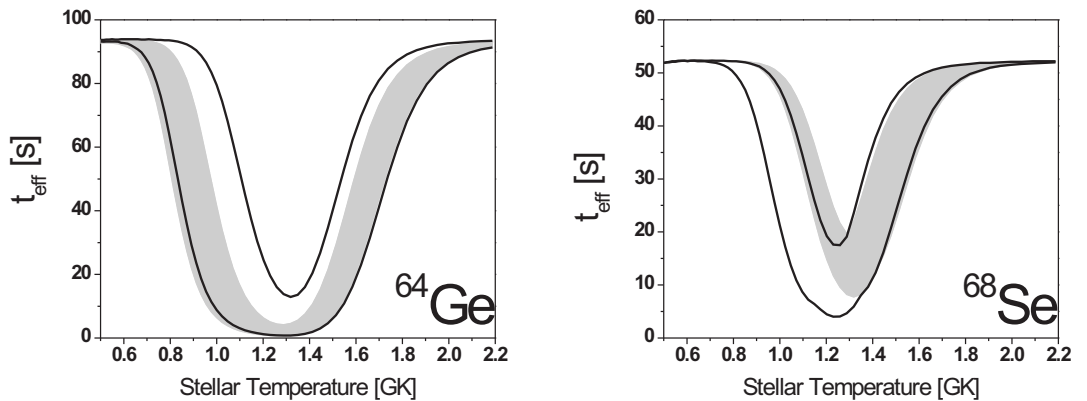
Figure 6.7. Envelope of calculations of the effective lifetimes for ^{64}Ge (left) and ^{68}Se (right) for 1-σ variations of the atomic masses. The filled area results from LEBIT data, while the open envelope results from previous literature mass values.

The factors dominating the uncertainty in the effective lifetime of ^{64}Ge are the unknown masses of ^{65}As and ^{66}Se, which had to be calculated via Coulomb shift energies. The uncertainty in the effective lifetime of ^{68}Se is dominated by the un-

known mass of ^{70}Kr, which also had to be calculated via Coulomb shift energy using the mass of ^{70}Se. The mass of ^{70}Se listed in 2003 Atomic Mass Evaluation is the weighted average of four independent mass measurements [105, 106, 107, 108] which are inconsistent.

CHAPTER 7

Summary

The LEBIT facility is so far the only system in the world capable of utilizing rare isotope beams created via fast projectile fragmentation to perform Penning trap mass spectrometry. Through the use of fragmentation beams, the LEBIT Penning trap mass spectrometer has access to isotopes not available elsewhere, such as short-lived isotopes of refractory elements.

In the design phase of the LEBIT facility, an emphasis was given to the simulation of all components. As part of this thesis, a number of computer simulations for the gas stopping station were performed. They included calculations both with and without the consideration of space charge effects. The ion guide system used to transport ions from the high-pressure region following the gas cell into a high-vacuum region was simulated as well. Offline tests of the ion guide system showed high-efficiency in agreement with calculations.

In order to be able to utilize the radioactive ions extracted from the gas cell for mass measurements, an advanced beam purification system was implemented. Through a combination of an RFQ mass filter, a gas target for molecular dissociation, a time-of-flight mass separator and in-trap contaminant removal, the rare isotope ions are removed from a background of stable molecular ions millions of times more intense.

Since the implementation of this purification system, more than 30 isotopes have been measured at the LEBIT facility. As of April 2007 they are: ^{37,38}Ca, ^{64,65,66}Ge, ^{40,41,42,43,44}S, ^{66,67,68,80}As, ^{29,34}P, ^{63,64}Ga, ^{68,69,70,81m,81g}Se, ^{33}Si, ^{70,71m}Br, ^{64,65,66}Co and ^{63,64,65}Fe.

In this thesis mass measurements of nine isotopes near N=Z have been presented: ^{63,64}Ga, ^{64,65,66}Ge, ^{66,67,68}As and ^{69}Se. ^{66}As, with a half-life of 96 ms, is one of the shortest-lived isotopes yet studied with a Penning trap. The mass measurement of ^{66}As, with an uncertainty of $\delta m/m = 4.1 \times 10^{-7}$, represents a 30-fold improvement in precision over previous measurements. In the case of ^{69}Se, the mirror of the unbound nucleus ^{69}Br, a 4σ deviation from earlier measurements has been found.

In combination with these mass measurements, calculated Coulomb displacement energies were used to estimate the masses of ^{63}Ge, ^{64,65}As, ^{66,67}Se and ^{68,69}Br using the measured masses of their mirror nuclei, leading to a considerable reduction in mass uncertainties in this region. The reduction in these uncertainties has lead to improvements of neutron-proton pairing energies for ^{66}As and ^{70}Br. The results may support a trend toward increased np pairing strength with heavier N=Z nuclei.

Using recent mass measurements from ISOLTRAP along with those presented in this work, provides further support for a restrengthening of the neutron-proton interaction strength. To investigate this trend, mass measurements of heavier N=Z nuclei at LEBIT are planned. Such measurements will hopefully provide further insight into neutron-proton pairing energies.

Astrophysical network calculations were performed with improved mass values. They indicate an enhanced waiting point nature for ^{68}Se and a decrease in the waiting point nature of ^{64}Ge. The new mass values are therefore likely to impact some existing x-ray burst models and should be used in future x-ray burst studies.

Penning trap mass measurements of ^{68,70}Se have only recently been performed at the LEBIT facility. When analysis of these new measurements is complete, the

uncertainty in the effective lifetime of ^{68}Se will yet further be reduced.

Based on experience with ^{64}Ge, ^{66}As and ^{68}Se it is planned to measure the masses of ^{63}Ge, ^{65}As and ^{67}Se at the LEBIT facility. These measurements will further reduce uncertainties in the effective lifetimes of ^{64}Ge and ^{68}Se. A remeasurement of the mass of ^{66}As to a precision of $\delta m/m \leq 1\text{x}10^{-8}$, which would make it a candidate for testing the Conserved Vector Current hypothesis [1], is also planned in the near future.

In conclusion, the installation of a Penning trap mass spectrometer facility at a rare isotope beam facility using fast projectile fragmentation has been highly successful. The facility has been able to access short-lived isotopes of refractory elements which are difficult or impossible to produce elsewhere and has successfully performed high precision mass measurements with them. In many cases the improvement in mass precision over previous values has been more than a factor of 10. High precision mass measurements of nuclei near N=Z=33 performed at the LEBIT facility have been used to calculate the effective lifetimes of the important rp-process waiting point nuclei ^{64}Ge and ^{68}Se. The same mass measurements have shown an indication for a restrengthening of the Wigner energy of N=Z nuclei in this region.

APPENDIX A

Details of Mass Evaluations

This Appendix contains the full set of data used for the mass determinations in chapter 6. The data consists of series of frequency ratios for each isotope studied, both with and without count rate analysis. The data was analyzed using the SOMA software, developed by Ryan Ringle, which is discussed in [79].

Table A.1. Distribution of excitation times for all sets of measurements. $\overline{ions}$ refers to the mean number of ions detected per excitation cycle across each data set. All ions are singly charged.

Date	Species	Reference	50 ms	200 ms	250 ms	300 ms	500 ms	$\overline{ions}$
Aug-05	^{67}As	^{86}Kr	1	-	-	-	4	1.2
Oct-05	^{67}As	^{86}Kr	1	-	-	-	-	0.6
Nov-05	^{67}As	^{85}Rb	-	1	-	14	-	0.5
Oct-05	^{65}GeH	C_5H_5	3	-	10	-	-	2.3
Nov-05	^{65}GeH	^{85}Rb	-	-	-	2	-	0.6
May-06	^{65}GeH	C_5H_2	-	-	-	-	1	0.6
Nov-05	^{66}As	^{85}Rb	4	-	-	-	-	0.002
Jun-06	^{66}GeH	C_5H_5	-	-	-	-	4	0.8
Jun-06	^{68}As	CF_3	-	-	-	-	3	0.2
Jun-06	^{69}Se	CF_3	-	-	-	-	5	0.6
Jun-06	^{64}GeH	HSO_2	-	-	-	-	3	0.5

A.1 Frequency Ratios from Raw Data

Table A.2. Measured frequency ratios for each set of mass measurements based on raw data.

Reference:	$^{86}Kr^+$	$^{86}Kr^+$	$^{85}Rb^+$
$^{67}As^+$	0.77917229(28) 0.779171967(33) 0.779171875(39) 0.779171856(38) 0.779171911(51)	0.77917095(35)	0.788337307(57) 0.788337343(45) 0.788337306(46) 0.788337390(48) 0.788337330(40) 0.788337353(36) 0.788337293(35) 0.788337312(38) 0.788337362(36) 0.788337439(46) 0.788337303(29) 0.788337425(32) 0.788337475(62) 0.788337320(47) 0.788337347(42)
Weighted Mean:	0.779171909(19)	0.77917095(35)	0.788337347(11)
Reference:	$C_5H_5^+$	$^{85}Rb^+$	$C_5H_2^+$
$^{65}GeH^+$	1.01396109(84) 1.01396203(16) 1.01396214(12) 1.013962221(98) 1.01396202(12) 1.01396193(14) 1.01396196(18) 1.01396205(12) 1.01396197(12) 1.01396203(13) 1.01396190(12) 1.01396178(43) 1.01396269(66) 1.01396232(19)	0.776653854(80) 0.776653896(96) 0.77665362(13)	1.063396520(57)
Weighted Mean:	1.013962053(39)	0.776653825(56)	1.063396520(57)

Table A.3. Continuation of measured frequency ratios for each set of mass measurements based on raw data.

Reference:	^{85}Rb$^+$		
^{66}As$^+$	0.77661698(78) 0.77661827(32) 0.77661925(57) 0.77661745(46)		
Weighted Mean:	0.77661811(23)		
Reference:	$C_5H_5^+$		
^{66}GeH$^+$	1.029252660(55) 1.029252772(56) 1.029252871(64) 1.029252805(80)		
Weighted Mean:	1.029252765(31)		
Reference:	CF_3^+		
^{68}As$^+$	0.98465893(14) 0.984659249(63) 0.984659048(74)		
Weighted Mean:	0.984659141(45)		
Reference:	CF_3^+		
^{69}Se$^+$	0.999191289(75) 0.999191277(41) 0.999191324(40) 0.999191354(46) 0.999191312(48)		
Weighted Mean:	0.999191313(21)		
Reference:	HSO_2^+		
^{64}GeH$^+$	0.999688870(98) 0.999689074(74) 0.999688839(50)		
Weighted Mean:	0.999688906(38)		

A.2 Frequency Ratios from Count Rate Adjusted Data

Table A.4. Measured frequency ratios for each set of mass measurements based on count rate analyzed data.

Reference:	^{86}Kr$^+$	^{86}Kr$^+$	^{85}Rb$^+$
^{67}As$^+$	0.77917245(65) 0.779171892(86) 0.779171842(65) 0.779171827(59) 0.779171896(70)	0.77917051(73)	0.788337372(81) 0.788337373(64) 0.788337344(74) 0.788337254(85) 0.788337279(76) 0.788337336(62) 0.788337265(56) 0.788337351(49) 0.788337394(63) 0.788337439(61) 0.788337349(58) 0.788337483(63) 0.788337516(73) 0.788337346(71) 0.788337383(70)
Weighted Mean:	0.779171859(34)	0.77917051(73)	0.788337366(17)
Reference:	C$_5$H$_5^+$	^{85}Rb$^+$	C$_5$H$_2^+$
^{65}GeH$^+$	1.0139610(16) 1.01396209(26) 1.01396195(19) 1.01396233(20) 1.01396173(27) 1.01396126(38) 1.01396173(50) 1.01396215(22) 1.01396204(15) 1.01396192(16) 1.01396197(17) 1.0139623(10) 1.0139621(11) 1.01396203(50)	0.776653743(99) 0.77665375(15) 0.77665380(15)	1.063396513(69)
Weighted Mean:	1.013961997(65)	0.776653759(73)	1.063396513(69)

Table A.5. Continuation of measured frequency ratios for each set of mass measurements based on count rate analyzed data.

Reference:	$C_5H_5^+$		
$^{66}GeH^+$	0.77661698(78)		
	0.77661826(32)		
	0.77661926(58)		
	0.77661746(46)		
Weighted Mean:	0.77661811(23)		
Reference:	$C_5H_5^+$		
$^{66}GeH^+$	1.029252756(69)		
	1.029252788(65)		
	1.029252939(96)		
	1.02925295(11)		
Weighted Mean:	1.029252824(40)		
Reference:	CF_3^+		
$^{69}Se^+$	0.999191277(85)		
	0.999191271(61)		
	0.999191324(40)		
	0.999191354(46)		
	0.999191312(48)		
Weighted Mean:	0.999191318(23)		
Reference:	HSO_2^+		
$^{64}GeH^+$	0.99968887(10)		
	0.99968917(16)		
	0.999688878(88)		
Weighted Mean:	0.999688922(62)		

APPENDIX B

Original Ion Guide System

B.1 Mechanical Details

The original ion guide system was based upon a segmented ion guide design used at ISOLTRAP. The ion guide contained 30 RFQ segments, consisting of a two pairs of 17 mm diameter rods. Each segment had an inscribed opening of 12 mm diameter. The full length of the system was $\approx$150 cm.

The electrode pairs were connected by copper ribbons which were arched around adjacent rods. The segments were hollow and supported by a long stainless steel threaded rod, isolated by ceramic washers.

The system incorporated two differential pumping diaphragms. A skimmer was placed between the 8th and 9th set of segments and a second diaphragm was placed between the 22nd and 23rd set of segments. Due to the low pressure in this region, the second diaphragm was a simple orifice.

B.2 RF Distribution

Each segment was individually biased using a distribution circuit as illustrated in Fig. B.1. The distribution circuit uses capacitors and inductors to combine an RF signals

(labeled Phase1 and Phase2) with the DC voltage used to supply an axial electric field for dragging ions through the buffer gas. The DC voltage is supplied by means of a voltage divider.

63 Kapton coated wires connected the pairs of segments, nozzle, skimmer and orifice to a set of vacuum feedthroughs which attach to the distribution circuits. The "cable spaghetti" from the wires resulted in a rod-to-ground capacitance of ≈ 10 nF and an inter-rod capacitance on the order of 1 nF.
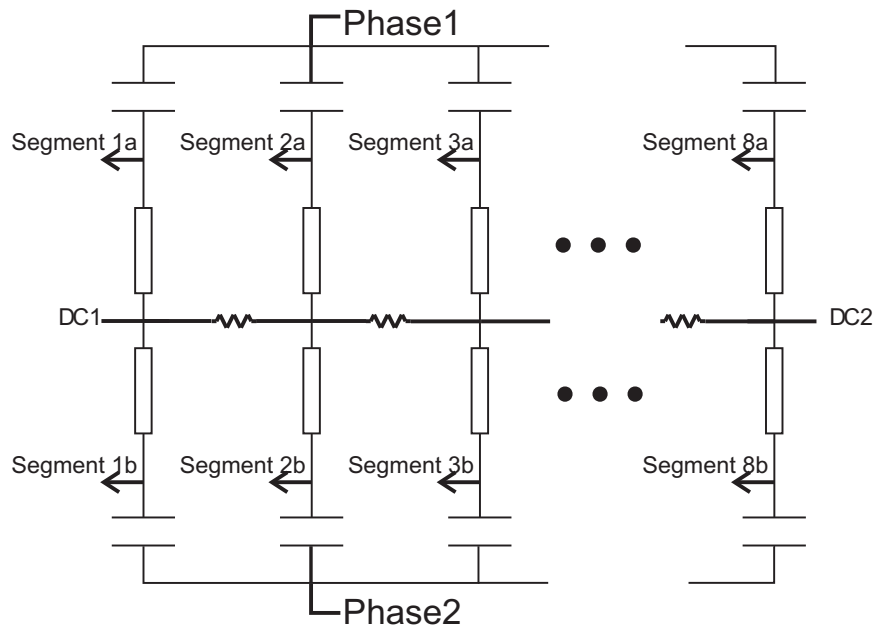
Figure B.1. Illustration of RF distribution circuit used in original LEBIT ion guide system.

B.3 Square Wave Generator

The square wave generator drives the radio-frequency quadrupole (RFQ) ion guides, which transport ions from the gas cell nozzle into the high vacuum portion of the LEBIT beam line. The driver is designed to provide two square wave outputs that are 180° out of phase (i.e. when one is high, the other is low.) The driver provides an

output of up to 600V peak at frequencies from 300kHz up to 2.25MHz. For amplitude
control, circuitry for controlling an UltraVolt power supply is built into the design,
however alternate external high voltage power supplies may also be used.

B.3.1 Design
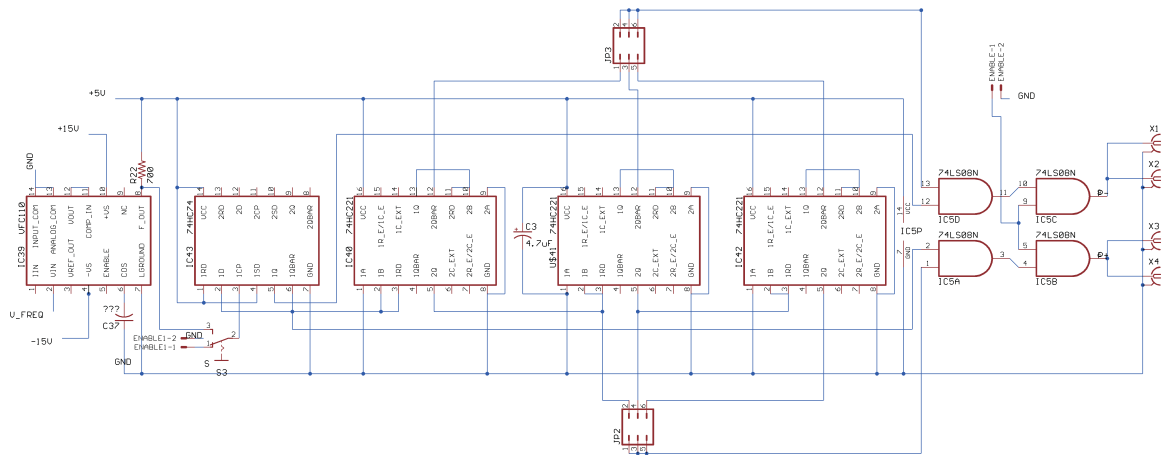
Figure B.2. Low-voltage driver circuit schematic.

Fig. B.2 shows the circuit schematic for the low voltage signal generator. The
first component from the left is a voltage-to-frequency converter (VFC) (Burr-Brown
VFC110). The VFC110 linearly converts [0V, 10V] to [0Hz, 4MHz]. After the VFC,
a flip-flop (74HC74), which converts the spiked output of the VFC into a pair of com-
plementary square waves. The three chips after this are non-retriggerable monostable
multivibrators (74HC221), used as a delay line. Jumpers are provided to select the
delay time by changing the number of active gates. The final component is a quad
logical AND gate (74LS08). The first set of gates, A and D, AND the delayed signals
with their non-delayed counterparts. This cuts out a small portion of the signal to
ensure that only one signal is high at any given moment. The second set, B and
C, AND the output from A and D, respectively, with the enable signal, allowing for

123

remote disabling of the device. Each signal is made available at a pair of SMA connectors. SMA cables take the signals to a pair of secondary boards, where the low voltage square waves are "amplified".
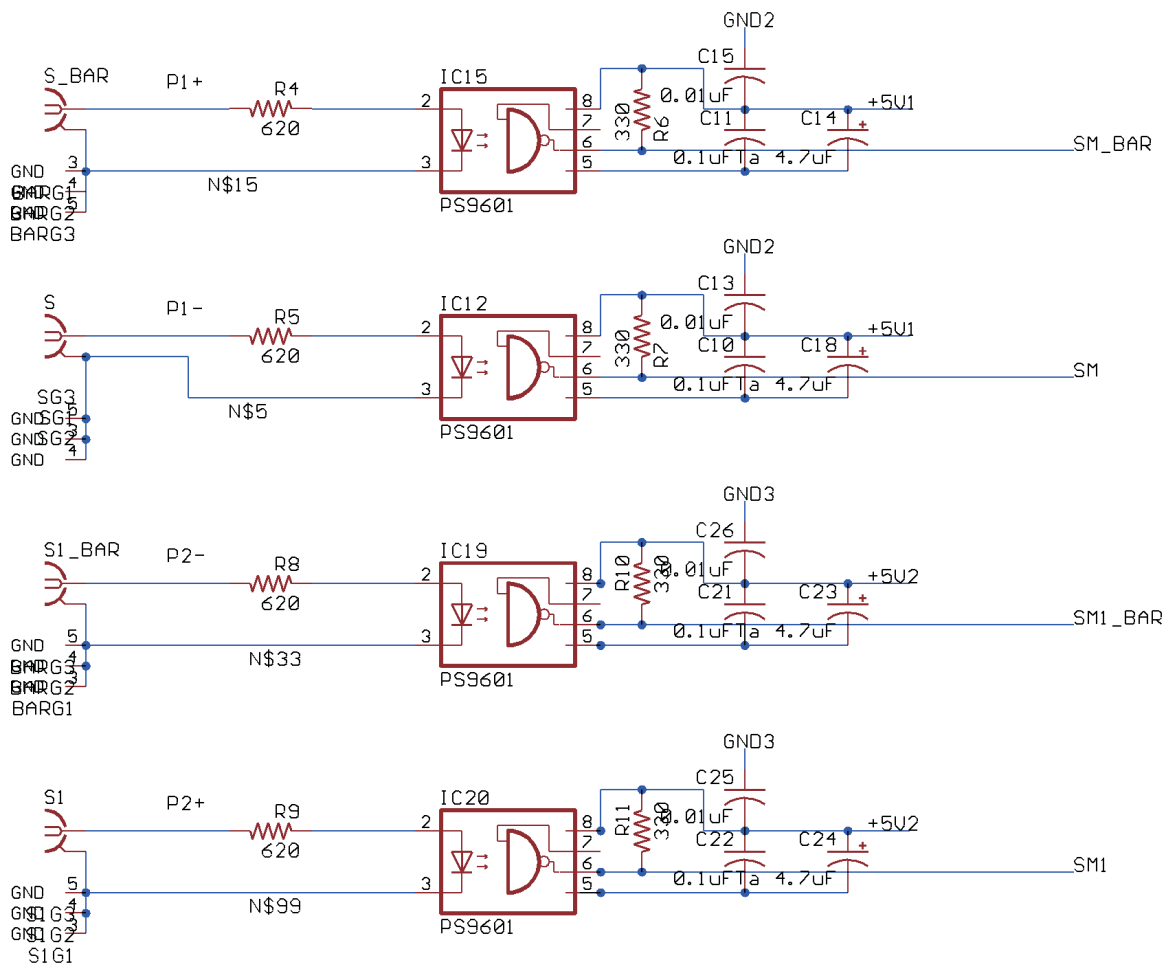
Figure B.3. Circuit schematic of the low-voltage to High-voltage opto-coupler.

Fig. B.3 shows the opto-coupling circuitry that helps to eliminate ground loops. These opto-couplers also protect the low voltage RF components from high voltage in the case that the pulse transformers (discussed later) suffer catastrophic failure.

Fig. B.4 shows the high voltage portion of the driver. This portion of schematic, although only shown once, is used twice - one for each output channel. The left side inputs of B.3 connect to the right side outputs in Fig. B.4.
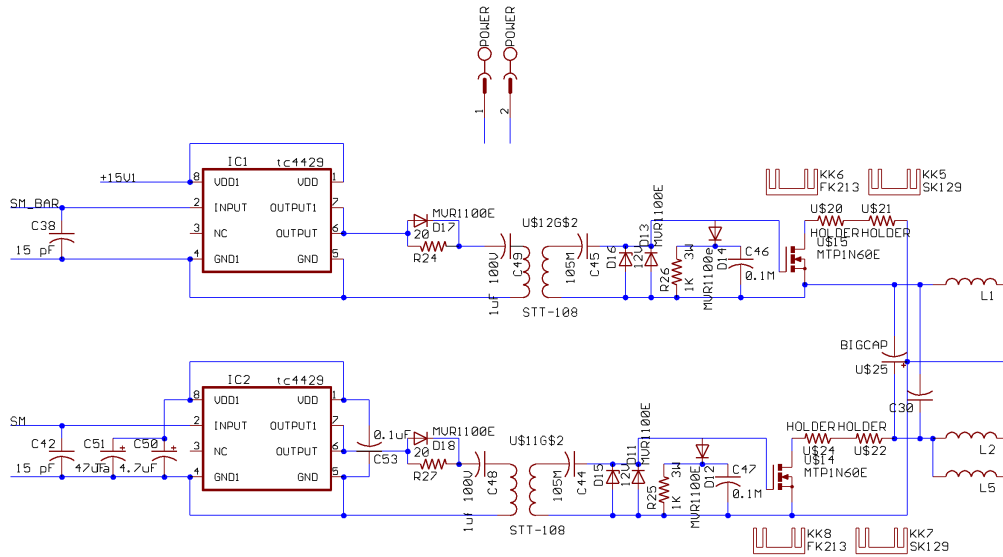
Figure B.4. High-voltage "amplification" circuit schematic.

In order to discuss the operation of this circuit let us designate one of the low voltage square waves the signal and the other the complement, the same will hold for the output - one is the output signal, the other is the output complement. The output signal is connected to MOSFET driver, and the complement is connected to an inverting MOSFET driver. When the signal is high, the MOSFET driver opens the MOSFET on high voltage. When the complement is high, the inverting MOSFET driver opens the MOSFET on ground. If the signal and complement are truly complementary, only one MOSFET will be on at a time and will make a high voltage square wave with the same frequency as the low voltage signal. For the complementary output we just switch the signal and complement.

In Fig. B.4, IC6 and IC7 are MOSFET drivers (TC4420 and TC4429 [inverting]). The Tamura STT-108 pulse transformers chosen by experimentally testing several pulse transformers allow the MOSFET trigger signal to be floated onto HV without floating the MOSFET driver supply, isolating the low voltage from the high voltage. The pulse transformers feed the high voltage, high current MOSFETs. These are

125

MTP3N60, rated for 600V and 5A. They can be replaced with STP20N60 (20A MOSFET) transistors should more output power be needed. The last components to be mentioned are the Ohmite resistors. These are special low inductance alumina resistors rated for 35W each. They are used to give a low output impedance (48Ω). With higher output impedance, large signal degradation is seen on the RFQ structure from RC charging/discharging.

B.3.2 Operational Limits

The lower frequency limit of 300kHz is a set by the pulse transformers. The upper limit on frequency is largely from the TC442X MOSFET drivers, which do not operate well above 2.25 MHz. The upper limit for the square wave amplitude comes from a combination of issues. The MOSFETs are only rated for 600V. Also, the power drawn at higher frequencies can severely limit the maximum amplitude, see Fig. B.5.
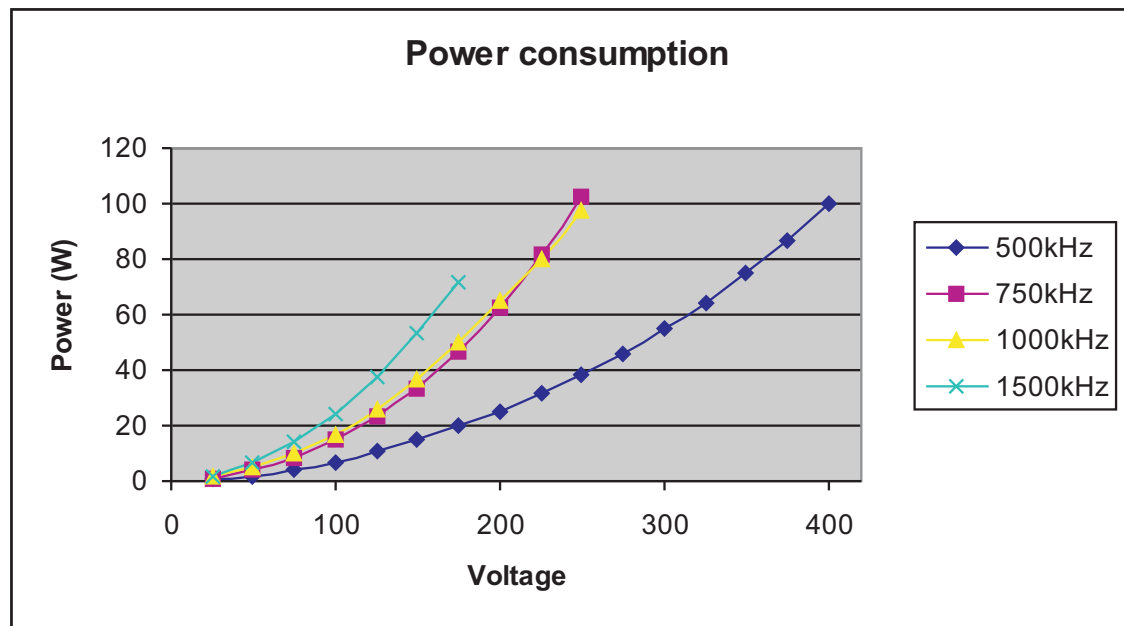
Figure B.5. Power drawn by the sRFQ circuit as a function of amplitude at several frequencies.

The system is designed to make use of an UltraVolt model 1/2C24-NP250 dual polarity, high voltage power supply. It can deliver up to 400mA from each polarity, for a total of 250 watts at full voltage. At lower voltages, however, the unit can still deliver only 400mA. If the 400mA limit is exceeded, the voltage drops by 33% so as to fall below 400mA current. This voltage drop does not appear to be documented in the UltraVolt datasheet, but was experimentally noticed.

B.3.3   Construction and Operation

Figure B.6. The assembled sRFQ driver with (right) and without (left) fans installed.

The assembled unit is placed into a 5.25"×17"×19" rack-mount box with ventilated top and bottom. The Newark part numbers are:

<div align="center">

Chassis 90F6951

Chassis Cover 90F6960

</div>

The assembled unit with and without fans is shown in Fig. B.6. In the lower left can be seen the Cosel power supply that delivers the +/-15V and the 5V. In the upper left is the UltraVolt 1/2 C24 PN250 high voltage power supply. The copper cages on the two sub-boards help reduce noise pick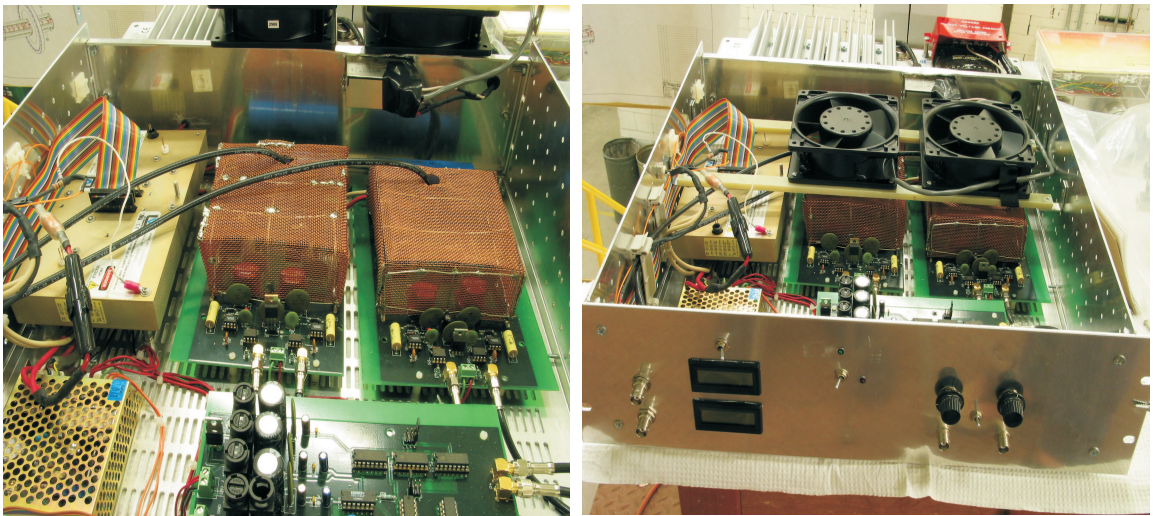-up in the control signals, as well as reducing high frequency noise induced onto the AC mains ground. The cages are hand-made using copper screen and 18 AWG wire. The transistors and the resistors dissipate a great deal of heat, so large fans need to be used to avoid runaway heating. The fans shown are P/N 28-175, from MCM Electronics, which displace 105 CFM each. Attached to the rear of the box is a large 24V linear power supply for powering the UltraVolt HV power supply.

On the front panel are a number of controls. On the far left are two BNC connectors stacked vertically. These are the two high voltage square wave outputs. Care must be taken to avoid accidental grounding or cross-connection of the outputs, especially when using the UltraVolt power supply; either of these conditions will destroy the UltraVolt power supply! To the right of the outputs is a pair of panel meters. The bottom one displays the output frequency in MHz. The top panel can be switched between displaying output voltage and HV current consumption using the switch above the panel meters. The switch in the very center of the front panel enables the high voltage output. When the green light above this switch is on, the box is receiving AC power - in general this means there is high voltage in the box. When the red light to the right of the switch is on, the high voltage square wave output is on. On the right hand side of the front panel is a pair of knobs above a pair of BNC connectors. The knob/BNC on the left of the switch controls the high voltage amplitude; the knob/BNC on the right controls the frequency. The switch allows the user to choose manual (knob) control or remote (BNC in) control.

APPENDIX C

Improved Ion Guide System

As described in chapter 5.1, the improved ion guide system consists of a highly segmented ion guide, a μRFQ ion guide and a modestly segmented ion guide mass filter. This appendix provides details as to the electronic implementation of the improved ion guide system.

The RF amplitude for each component ion guide is individually controlled. The electronics used to control the RF signals will be described in the first section of this appendix, followed by a brief discussion of the use of resonant LC circuits. Wiring details and descriptions of the circuitry used to distribute the RF signals will be described in the final section of this appendix.

C.1   Ion Guide Driver Circuit

The LEBIT ion guides consist of three separate ion guides. In order to efficiently transport ions from the gas cell, we need to have a flexible control system for the ion guides. We must have the ability to control the frequency, amplitude and relative phase of three RF signals, one for each ion guide.

A set of low voltage RF signals, intended to be connected to the inputs of a set of RF amplifiers, a created using the ion guide control circuit described herein. The

amplifier outputs are then connected to a set of tuned LC circuits which in turn connect to the RF distribution circuits.

C.2 Circuitry

Figure 5.4 shows a flowchart illustrating the design of the ion guide RF control circuit. The first component seen in the flowchart is a switch between PLC and PLL frequency control. PLC control refers using using MAX038 frequency generator as a voltage controlled oscillator controlled via an analog voltage from the PLC system. PLL control refers to using the phase locked loop (PLL) function of the MAX038 with an external arbitrary function generator (AFG). For PLL functionality, the AFG must be operated in TTL output mode.

The MAX038 has two outputs, a $2V_{pp}$ sinusoidal output and a TTL sync output. The sinusoidal output is sent to an AD835 fast 4-quadrant multiplier. The AD835 multiplies the output of the MAX038 with a programmable voltage. The AD835 can only handle inputs between -1V and 1V, so the amplitude control voltage (from either the PLC or a manually set voltage) is reduced by a factor of ten using an op-amp (LF347). The final output to the RF amplifier is turned on and off by use of an RF-relay (G5Y), labeled "Enable" in the flowchart.

Phase control is provided through the use of a programmable delay line. The sync out from the MAX038 is sent to an 8-bit programmable delay line (DS1023) capable of delaying a TTL signal by as much as 1 μs. The delayed signal is used for the PLL input for the next MAX038.

The delay time is programmed by a 0-10V programming voltage. An ADC (MAX160) converts this voltage to an 8-bit digital signal for programming the delay line. In order to utilize the MAX160 ADC a 74LS90 decade counter is used as a divide by 10 to reduce a 1MHZ crystal oscillator to 100kHz, the highest frequency at

which the MAX160 can be run.

The μRFQ control block after the MAX038 is identical to the HPIG control block, with the exception that the AD811 output op-amp is unity gain because the μRFQ RF amplifier only accepts $1V_{rms}$ input. The mass filter control block is identical to the μRFQ control block.

The front panel has an on/off switch for the main power, as well as enable/disable switches for each ion guide RF. On the front panel there are also local/remote switches for controlling the frequency, relative phases of three RF signals, and the amplitude of each RF signal. The local control for all signals is provided by potentiometers with -12V and 12V connected at the ends.

The low voltage RF signal output is found on the rear of the control box, along with connections for PLL in and TTL sync out. The sync out is for monitoring the RF frequency.
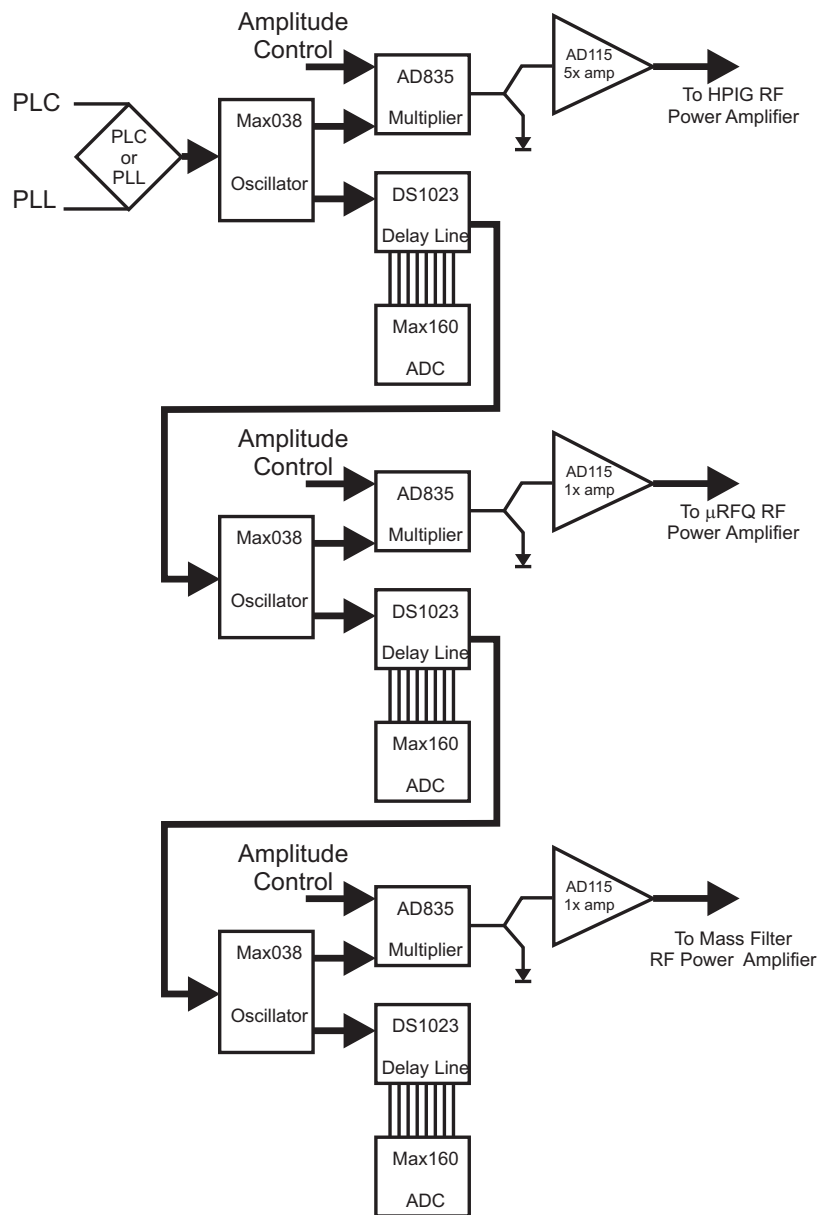
Figure C.1. Flowchart illustrating the low voltage RF control system.

C.3 Resonant LC Circuits for RF Amplifiers

The resonant LC circuits mentioned in Fig. 5.4 are simply an inductor and capacitor in series. The circuit response is dependent on the applied signal frequency, ω. The impedance of the inductor is $Z_L = -\imath\omega L$, while the capacitor impedance is $Z_C = \frac{\imath}{\omega C}$. As the applied signal frequency approaches $\omega = \sqrt{\frac{1}{LC}}$, the circuit impedance becomes vanishingly small. This frequency is the resonant frequency of the circuit. For a signal at the resonant frequency the only resistance seen in the circuit is that from the wires which connect the components. A detailed analysis of such circuits can be found in any decent electronics textbook.

An RF power amplifier behaves as the RF equivalent of a constant current source. These amplifiers are commonly used with resonant LC circuits, such as shown in Fig. C.2. When the power amplifier is operated at the resonant frequency of the circuit, where the impedance is extremely low, the RF amplitude (at the node between capacitor and inductor) becomes large in accordance with Ohm's law.

Two slightly different types of resonant LC circuits are used in the LEBIT ion guide system. The first type, illustrated by Fig. C.2a, is used for the HPIG and the μRFQ; the second type, illustrated by Fig. C.2b, is used for the mass filter ion guide. Both circuits use a ferrite core transformer to match the 50Ω output impedance of the amplifier to the low resonant impedance of the LC circuit. An air-core wire coil (resembling a bed spring) forms the inductor. The capacitance comes from the combination of an air-gap variable capacitor and the capacitance of the RFQ system (labeled C_L). The use of a variable capacitor provides the ability to adjust the resonant frequency of the circuit.

The circuit for the mass filter employs a split winding on the secondary side of the impedance matching transformer. By applying the DC voltages MFDC1 and MFDC2 to the ends of the windings, the potentials used to form the mass filter's DC quadrupole field can be added to the RF signals. This provides a distinct advantage

133
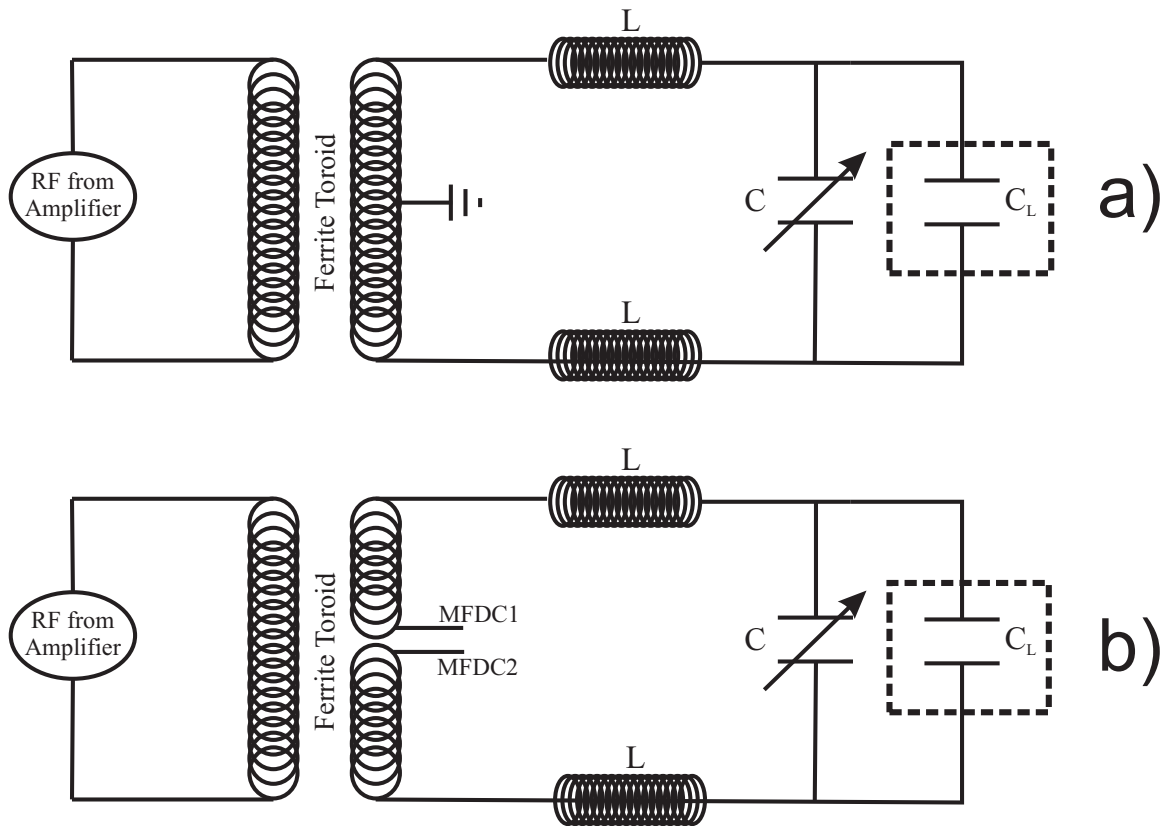
Figure C.2. Illustration of the two types of resonant LC circuits used for the LEBIT ion guide RF system.

over the scheme shown in Fig. 4.15, where the inductors dissipated a large amount of RF power.

C.4   RF Distribution

A number of changes were made to the RF distribution system used in the improved ion guide system, based on the experience gained with the original system. This section will describe the distribution of RF and DC signals for the improved ion guide system.

C.4.1 High Pressure Ion Guide

The high pressure ion guide (HPIG) consists of 7 RFQ segments. The segments along each rod are resistively connected in-vacuo. In the first 4 segments, identical voltages are applied to non-adjacent rods. In the last 3 segments, one pair of non-adjacent rods is wired as in the first 4 segments, while the other pair is decoupled to allow for superposing a high frequency (HF) dipole field.

Segments #1 and #4 each connect to the distribution circuit using two wires, one for each RF phase, while segment #7 is connected using three wires. The signals applied to each segment using this wiring scheme is illustrated in Fig. C.3.
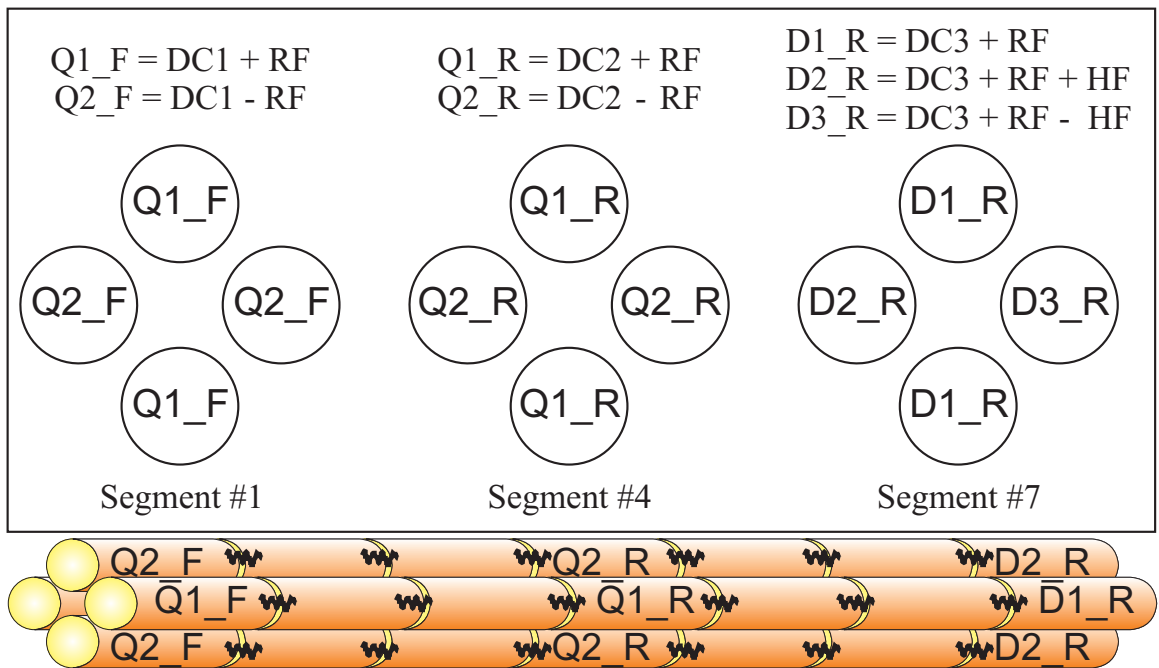
Figure C.3. Signals applied to segments #1, #4 and #7 of the high-pressure ion guides. RF refers the quadrupole RF signal, while HF refers to the dipole signal. The segments along each rod are connected in-vacuo using UHV resistors.

In order to allow for the option of selective CID prior to the mass filter, the last segments of the high pressure ion guide are wired to allow for superposition of an HF dipole field. The HF signal is added to the RF signal by means of a ferrite toroid

transformer, as shown in figure C.4.

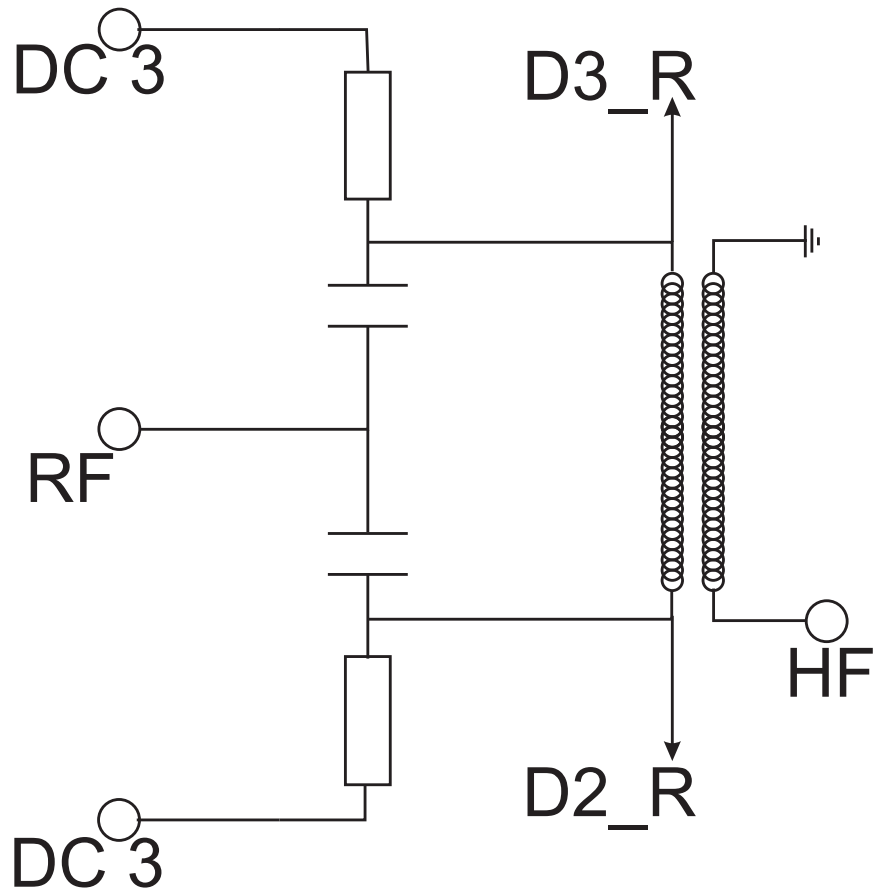Figure C.4. Schematic illustrating the implementation of the HF dipole in the high-pressure ion guide. A ferrite toroid transformer allows the addition of an HF signal on top of the RF signal applied to D3_R and D2_R (see Fig. C.3).

C.4.2   Mass Filter Ion Guide

Resistive chains are not used to supply the DC offset potentials in the mass filter RF distribution circuitry; each of the segments before and after the primary mass filter segment instead has a dedicated DC power supply. This is necessary for fine tuning the injection into the mass filter.

As discussed in chapter 5.1, the mass filter system employs a delayed DC-field, whereby the a fraction, x, of the DC quadrupole potential, V_{DC}, is applied to each segment in the system. The fraction which is applied to each section is shown in Fig. C.5a.

In order to reduce the number of power supplies needed for the mass filter system, the DC quadrupole potentials required for the delayed DC-field are supplied using resistor chains, as shown in Fig. C.5b.
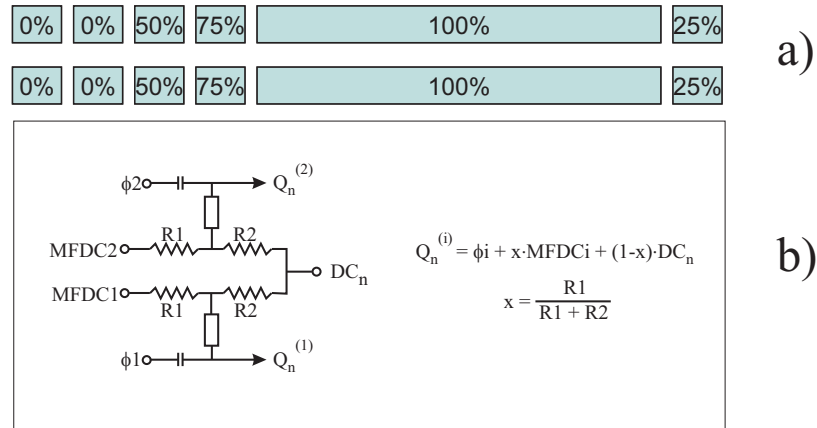
Figure C.5. (TOP) Fraction of DC-quadrupole potential applied to each segment in the implementation of a delayed DC-field for the ion guides. (Bottom) Circuit schematic used to create Delayed DC field potentails.

In Fig. C.5 MFDCi represent the two voltages which are used to create the DC quadrupole field for the mass filter, ϕi are the two RF signal which are used to create the RF quadrupole field, DC$_n$ is the DC offset potential for the nth RFQ segment, and Q$_n^{(i)}$ is the total potential applied to pair of rods in the nth segment; the i refers

to one of the pairs of rods. As noted in the figure, the total voltage, $Q_n^{(i)}$, applied to a pair of rods is equal to the RF signal plus a fraction of the DC quadrupole potential plus a fraction of the DC offset potential.

APPENDIX D

Electronic Designs

D.1 RF Monitor Circuit
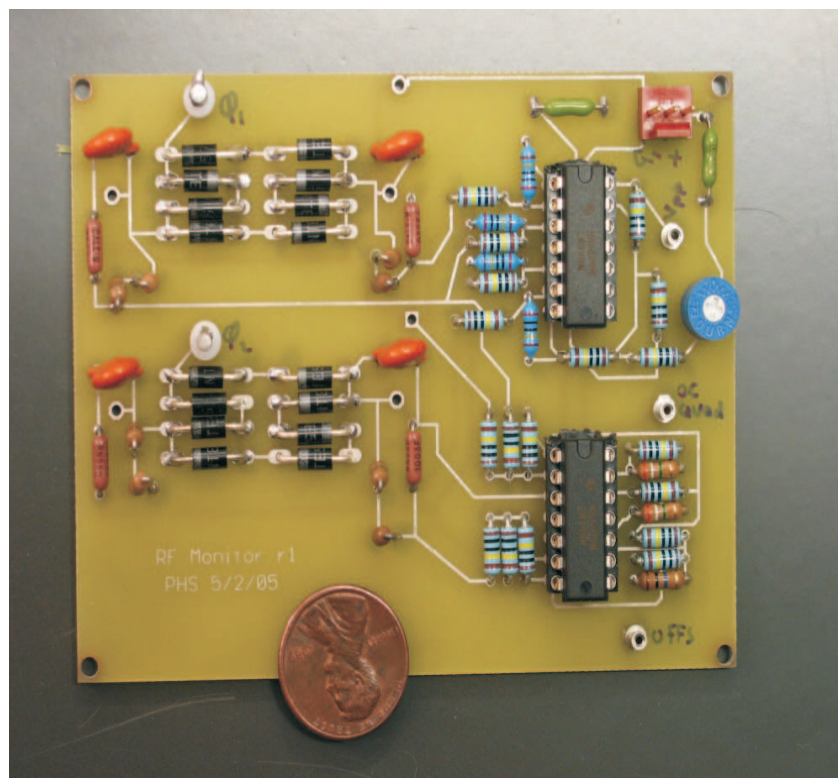
Figure D.1. Photograph of assembled RF monitor circuit board.

Knowledge of the RF amplitudes in the LEBIT ion guide system is very important, particular so for the mass filter. While these amplitudes can be monitored using oscilloscopes, this is undesirable – it is expensive and oscilloscopes are designed for accuracy in the time domain more so than in the voltage domain. Furthermore, the oscilloscope probes add a unnecessary capacitive load to the RF system. To monitor the RF amplitude without using oscilloscopes, a high-speed RF rectifier with op-amps was built which allows readout of the average amplitude of the two RF phases (which is what is truly important) as well as the DC quadrupole amplitude and the average DC level.

D.2 Schematic

Figure D.2. (top) RF rectification circuit schematic for up to 1 kV RF amplitudes. (bottom) Op-Amp circuit schematic for the RF monitor.

141

Figure 2 show the RF rectifier scheme used for the monitor. A high-speed high-voltage diode (NTE575), rated for 1000V with a typical recovery time of 72ns, is used to rectify the RF signals. In order to safely measure amplitudes up to 2kV, the monitor circuit "doubles-up" on the diodes so that no single diode has more than 1 kV across it. The rectified signal is then reduced by a 1:200 voltage divider network, to achieve a signal that can be used by the op-amps. For use up to 2 kV, 50kΩ resistors should replace the 100kΩ resistors shown. All resistors should be 1% tolerance or better. The op-amps require a ±12 V DC power supply.

In Fig. D.2, the designations "pin" and "pip" refer to "phase i negative" and "phase i positive," respectively, where the two RF signals are designated "phase 1" and "phase 2". pin is the negative half amplitude of the phase called phase i, and vice versa. As an example, if phase i is 100Vpp and has a DC level of +20V, then pip is 70V and pin is 30V (less the diode voltage drops, of course) at the test points and a factor of 200 or 400 less at the signal branch. These signals are the input for the op-amps. The op-amps perform simple addition and subtraction. (p1p+p1n) should equal the dc level of phase 1. (p1p-p1n) is the peak-peak amplitude of phase 1. All the op-amps do is perform the following operations:

$$V_{Quad} = (p1p + p1n) + (p2p + p2n) \qquad (D.1)$$

$$V_{Offs} = (p1p + p1n) - (p2p + p2n) \qquad (D.2)$$

$$V_{pp} = (p1p - p1n) + (p2p - p2n), \qquad (D.3)$$

where V_{Quad} is the DC quadrupole potential, V_{DC}, V_{Offs} is the DC offset potential and V_{pp} is the RF quadrupole potential, U_{RF}.

These three quantities fully characterize the RF signal.

One flaw in the circuit is that if the DC quadrupole potential U_{DC} is greater than the RF quadrupole potential V_{RF} then the calculated V_{pp} does not properly represent

142

the RF quadrupole potential. In order to achieve the best resolution when reading V_{pp} via an ADC, R64 (Fig. D.2) can be adjusted so as to set the output to a scale of (-5V,5V) or (-10V,10V) instead of (0,10V).

N.B. To make full use of the monitor, the RF must be connected directly, not capacitively! A capacitive connection will disable the V_{Quad} **and** V_{Offs} **outputs.**

D.3   Calibration

Calibration of the monitor is simple. For calibration of the DC levels, simply connect a pair of lab power supplies to the phase 1 and phase 2 inputs. Measure V_{Quad} and V_{Offs} as a function of the inputs. For obtaining a rough calibration for the V_{pp} output of the RF monitor, a pair of AFG's capable of 20Vpp is sufficient; use of an RF amplifier is preferable, however, so as to calibrate in the range not dominated by the diode drops. For the calibrations given below, a tunable resonant circuit was used in conjunction with a 10W amplifier. The method is to simply connect the two RF phases and measure both with an oscilloscope while measuring the Vpp output, then do the math. As is shown in Fig. D.3, the calibration curves for frequencies from <1MHz up to ≈2MHz are nearly identical. To improve high frequency results, smaller valued capacitors could be used.
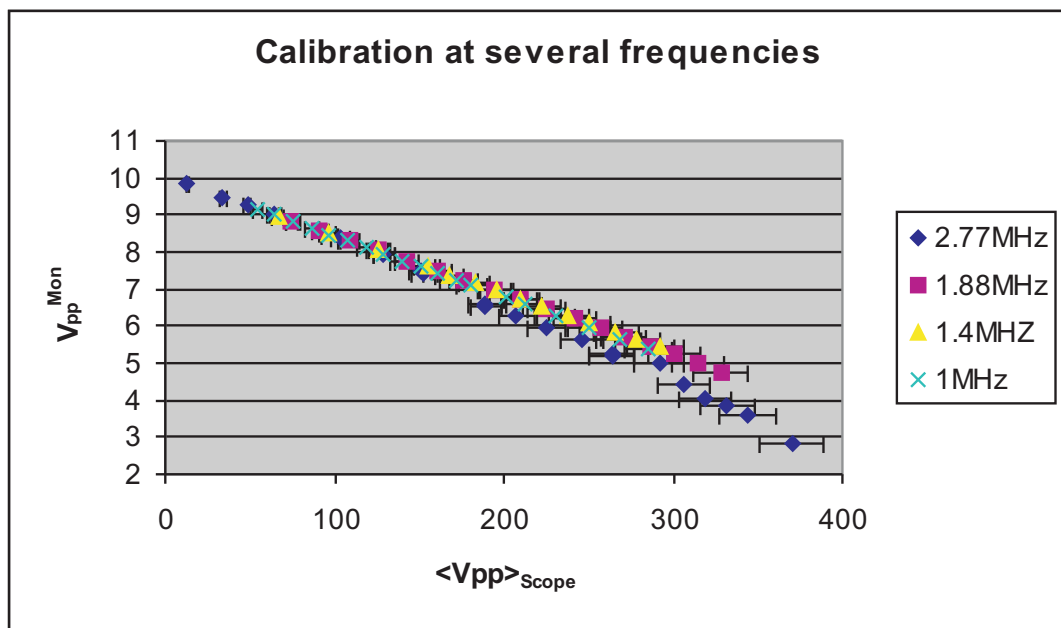
143

Figure D.3. RF monitor calibration curves, showing V_{pp} output as a function of RF amplitude, for several RF frequecies. For RF frequencies from <1MHz up to ≈2MHz, the calibration curves are nearly identical.

D.4 Fast High-Voltage Switch

This MOSFET-based switch provides fast switching of voltage levels with a maximum swing of 1200 V. These multi-purpose switches are used throughout the LEBIT facility for *e.g.* beam gates and in the fast ejection of ions from the beam cooler-and-buncher.
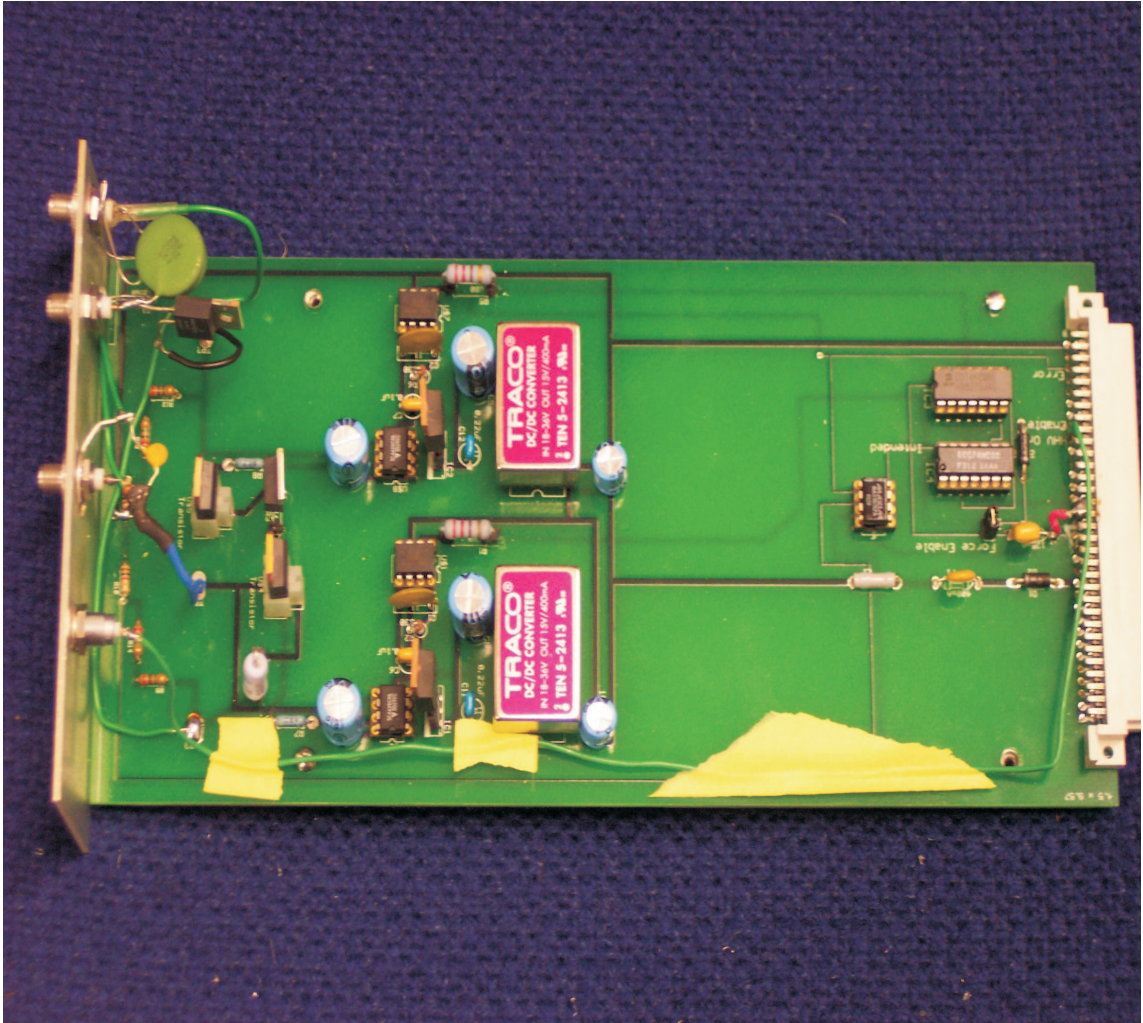

Figure D.4. Photograph of fully implemented high-voltage switch.

145

D.4.1 Design

This device is a two-state switch capable of a total swing of up to 1200 V. The two states will be referred to as HHV and LHV for higher high voltage and lower high voltage. HHV and LHV need not be of opposite polarity, however HHV must be at a greater potential than LHV. Power is supplied by the LEBIT bus.

Figure D.5 shows the circuit schematic for the switch. The switch works by lifting logic signals onto high voltage to signal MOSFET drivers and turn on one MOSFET at a time. PWS1 and PWS2 are DC-DC converters. The output of PWS1 floats on LHV, while that of PWS2 floats on the OUTPUT signal - LHV when the switch is closed, HHV when the switch is open, GND when ENABLE is low. These DC-DCs power U$2 and U$8, which are TC442x MOSFET drivers that turn MOSFETs U$4 and U$5, respectively, on or off. The signals for doing such are the signals LOW SIGNAL and HIGH SIGNAL, which are lifted onto high voltages by use of U$1 and U$7, which are PS9601 optocouplers. As a safety measure, comparator IC5 will disable switching if the voltage polarity is incorrect. Resistors R9 through R14 form a pair of 1:4000 voltage dividers. HHV and LHV, after being reduced by a factor of 4000, are the inputs for comparator IC5, the MAX907. D3 is an LED which can be employed to display an error condition.

D.4.2 Operational Limits

The MOSFETs to be used in the switch are designed for 600V, implying maximum switching capability of 1200V. In practice the switch was tested with no more than 650V potential difference without issue. At 600V potential difference, with switching rates below 5kHz, there was negligible (<1mA) current draw on the high voltage line. At 20 kHz, the current draw begins to increase near exponentially with frequency, exceeding the 10W rating of the push-pull resistors near 100 kHz. With a 10% duty cycle at 100 kHz, however, a HV current draw of 2.3mA was found at 600V operation.

The rise and fall times have been measured to be <200 ns when loaded with a $\approx$1 m 50Ω cable.
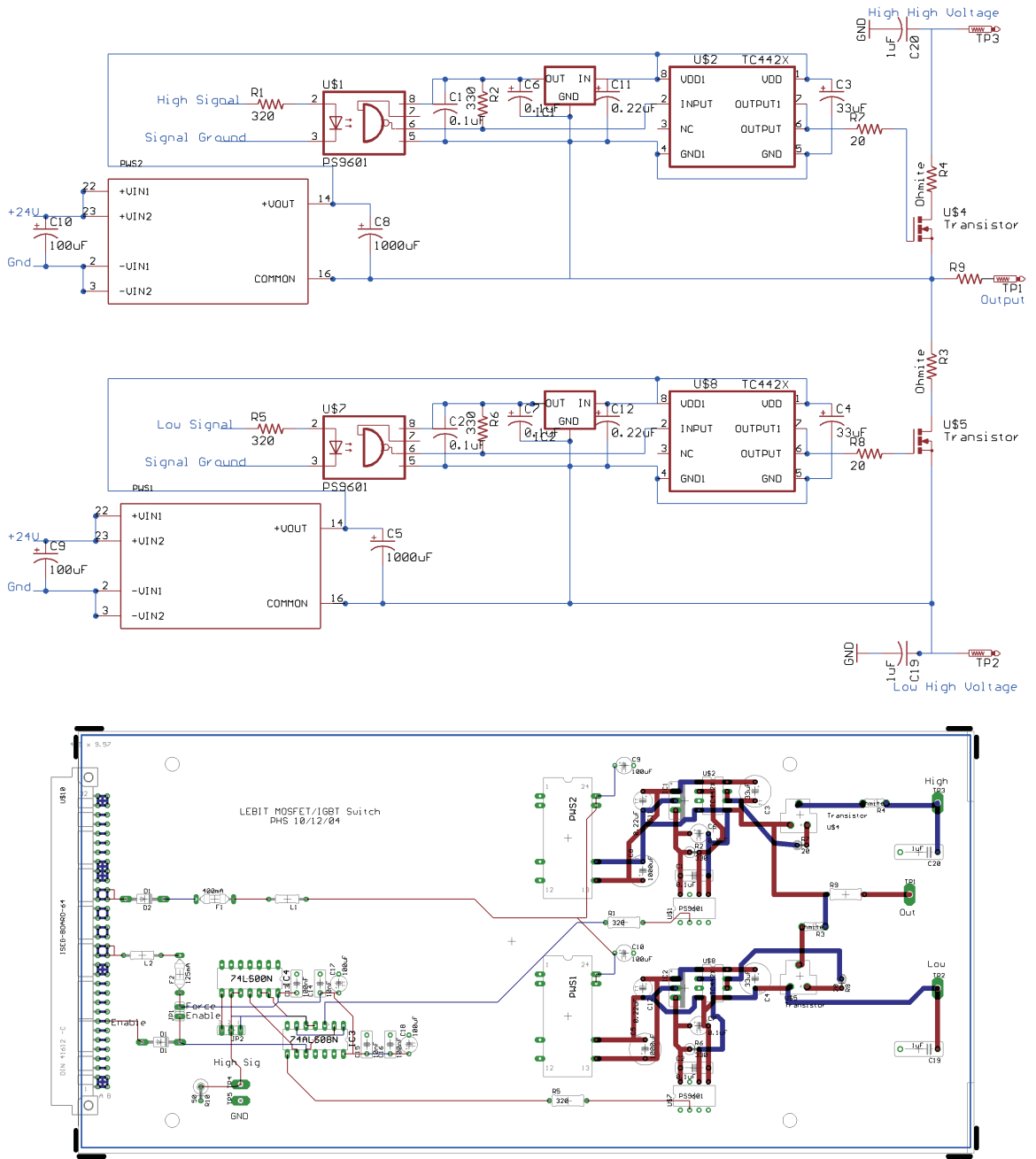
Figure D.5. Schematic and printed circuit layout for the high-voltage switch.

D.5 Fibre Optic MCP Readout

In order to transfer signals from MCP ion detectors and β-detectors located along the high-voltage transport lines to computer system on ground potential, a fibre optic system is used. The signals from the detectors are sent to a fibre optic transmitter circuit; the optical signal is converted back to an electronic signal by a fibre optic receiver on ground potential. The circuit schematics for the transmitter and receiver are provided in Fig. D.6.
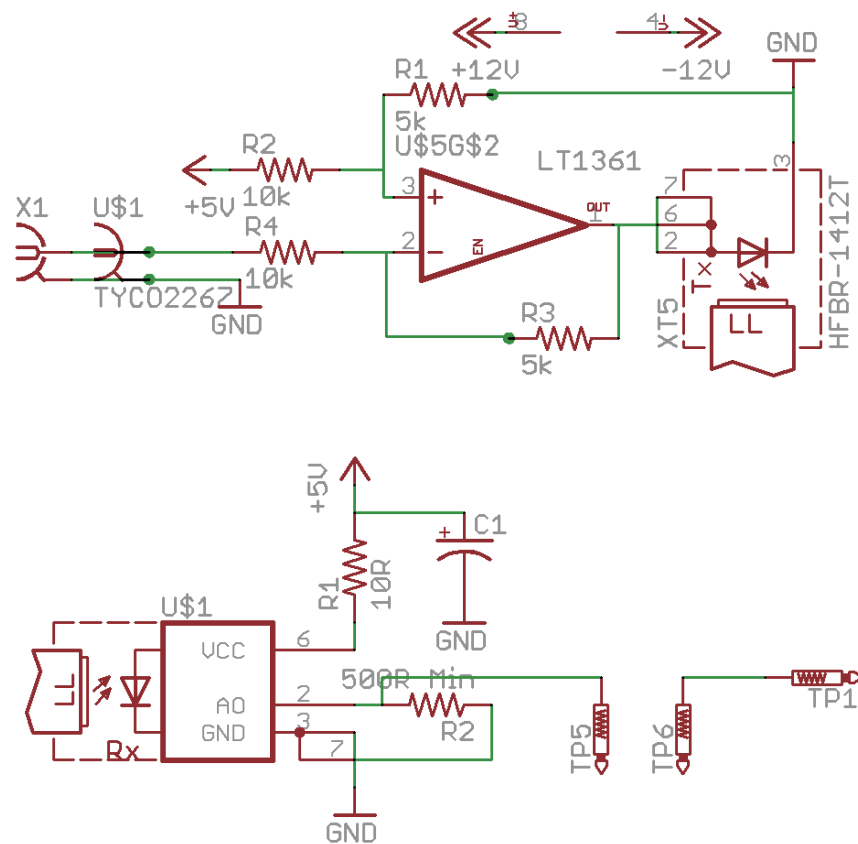

Figure D.6. (top) Circuit schematic for analog fibre optic transmitter. (bottom) Circuit schematic for analog fibre optic receiver.

The fibre optic transceiver, Agilent model HFBR-1412, is essentially a light emitting diode. The transmitter circuit uses a fast op-amp (LT1361) to add 5 V to the signal. In this way, it is possible to convert electronic signals from -4.4V (from the

149

diode drop) to +5V into optical signals. The receiver, Agilent model HFBR-2412, acts much like a common emitter amplifier, with the optical intensity playing the role of voltage applied to the base.

Figure D.7 shows a photograph of an oscilloscope display from a test of the transmitter and receiver circuits. A 10 V$_{pp}$, 2 MHz sine wave was sent into the transmitter circuit. The figure shows this signal as well as the output from the receiver. The distortion seen in the output of the receiver is due to the lower level of the input signal being below the diode drop voltage for the transmitter.
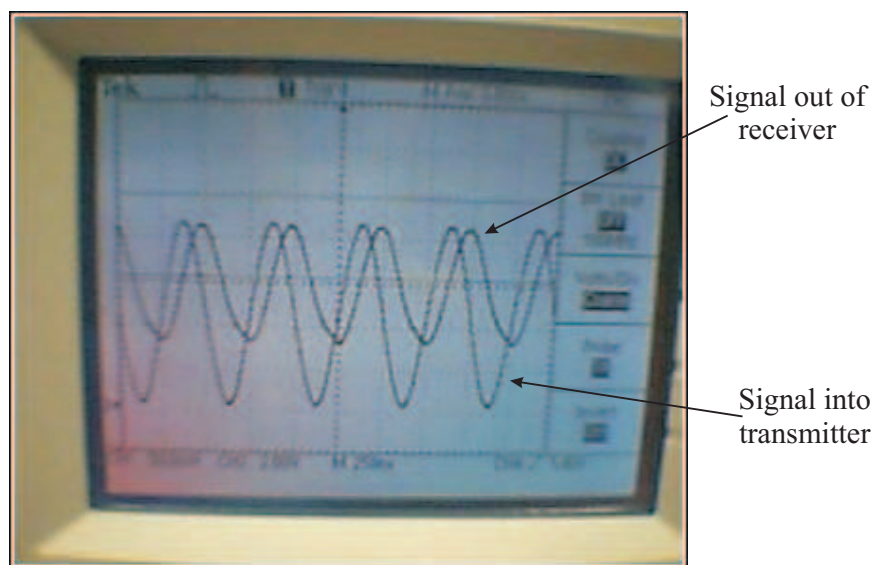

Figure D.7. Photograph of oscilloscope display demonstrating the functionality of the analog fibre optic system. The input signal was a 2 MHz sine wave with 10 V$_{pp}$ amplitude.

BIBLIOGRAPHY

[1] J. Hardy and I. Towner, Phys. Rev. C **71**, 055501 (2005).

[2] W.-M. Y. et al., J. Phys. G **33**, 1 (2006).

[3] I. Talmi, Rev. Mod. Phys. **34**, 704 (1962).

[4] H. Schatz, A. Aprahamian, J. Görres, et al., Phys. Rep. **294**, 167 (1998).

[5] R. Wallace and S. Woosley, Astrophys. J. Suppl. Ser. **45**, 389 (1981).

[6] F. Aston, Proc. Royal. Soc. A **115**, 487 (1927).

[7] K. Blaum, Phys. Rep. **425**, 1 (2006).

[8] G. Bollen, D. Davies, M. Facina, et al., Phys. Rev. Lett. **96**, 152501 (2006).

[9] R. Ringle, T. Sun, G. Bollen, et al., Phys. Rev. C (Accepted for publication).

[10] W. E. Ormand and B. A. Brown, Phys. Rev. C **52**, 2455 (1995).

[11] P. Schury, C. Bachelet, B. Block, et al., Phys. Rev. C (Accepted for publication).

[12] C. Thibault, R. Klapisch, C. Rigaud, et al., Phys. Rev. C **12**, 644 (1975).

[13] E. Wigner, Phys. Rev. **51**, 106 (1937).

[14] P. Vogel, Nucl. Phys. A **662**, 148 (1999).

[15] M. Chartier, G. Auger, W. Mittig, et al., Phys. Rev. Lett. **77**, 2400 (1996).

[16] P. V. Isacker, D. D. Warner, and D. S. Brenner, Phys. Rev. Lett. **74**, 4607 (1995).

[17] O. Koike, M. Hashimoto, K. Arai, et al., Astron. Astrophys. **342**, 464 (1999).

[18] H. Schatz, A. Aprahamian, V. Barnard, et al., Phys. Rev. Lett. **86**, 3471 (2001).

[19] B. A. Brown, R. R. C. Clement, W. Richter, et al., Phys. Rev. C **65**, 045802 (2002).

[20] H. Schatz, Int. J. Mass Spectrom. **251**, 293 (2006).

[21] D. Lunney, J. Peasron, and C. Thibault, Rev. Mod. Phys. **75**, 1021 (2003).

[22] G. Audi, M. Epherre, C. Thibault, et al., Nucl. Phys. A **378**, 443 (1982).

[23] H. Savajols, Hyperfine Int. **132**, 243 (2001).

[24] D. Bazin, J. A. Caggiano, B. M. Sherrill, et al., Nucl. Instr. and Meth. in Phys. Res. B **204**, 629 (2000).

[25] G. F. Lima, A. Lépine-Szily, G. Audi, et al., Phys. Rev. C **65**, 044618 (2002).

[26] B. Franzke, Nucl. Instr. and Meth. in Phys. Res. B **24**, 18 (1987).

[27] J. Stadlmann, M. Hausmann, F. Attallah, et al., Phys. Lett. B **586**, 27 (2004).

[28] Y. A. Litvinov, H. Geissel, T. Radon, et al., Nucl. Phys. A **756**, 3 (2005).

[29] M. de Saint-Simon, Phys. Sci. T. **59**, 406 (1995).

[30] C. Bachelet, G. Audi, C. Gaulard, et al., Euro. Phys. J. A **25sup1**, 31 (2005).

[31] W. Shi, M. Redshaw, and E. G. Myers, Phys. Rev. A **72**, 022510 (2005).

[32] G. Bollen, S. Becker, H.-J. Kluge, et al., Nucl. Instr. and Meth. A **368**, 675 (1996).

[33] R. Ringle, G. Bollen, D. Lawton, et al., Eur. Phys. J. A **25sup1**, 59 (2004).

[34] J. Dilling, R. Baartman, P. Bricault, et al., Int. J. Mass Spectrom. **251**, 198 (2006).

[35] S. Hofmann and G. Münzenberg, Rev. Mod. Phys. **72**, 733 (2000).

[36] G. Savard, R. C. Barber, D. Beeching, et al., Nucl. Phys. A **626**, 353 (1997).

[37] G. Sikler, D. Ackermann, G. Bollen, et al., Nucl. Instr. and Meth. B **204**, 482 (2002).

[38] P. Dendooven, Nucl. Instr. and Meth. in Phys. Res. B **126**, 182 (1997).

[39] V. S. Kolhinen, T. Eronen, J. Hakala, et al., Nucl. Instr. and Meth. in Phys. Res. B **204**, 502 (2003).

[40] W. Mittig, Nucl. Phys. News **1**, 30 (1990).

[41] H. Geissel, P. Armbruster, K. Behr, et al., Nucl. Instr. and Meth. in Phys. Res. B **70**, 286 (1992).

[42] T. Motobayashi, Nucl. Instr. and Meth. in Phys. Res. B **204**, 736 (2003).

[43] D. J. Morrissey, B. M. Sherrill, M. Steiner, et al., Nucl. Instr. and Meth. B **204**, 90 (2003).

[44] J. Verdú, T. Beier, S. Djekic, et al., Phys. Rev. Lett. **92**, 093002 (2004).

[45] S. Schwarz, G. Bollen, D. Lawton, et al., Nucl. Instr. and Meth. B **540**, 474 (2003).

[46] F. Herfurth, J. Dilling, A. Kellerbauer, et al., Nucl. Instr. and Meth. A **469**, 254 (2001).

[47] F. Ames, G. Bollen, P. Delahaye, et al., Nucl. Instr. and Meth. in Phys. Res. **538**, 17 (2005).

[48] G. Savard, S. Becker, G. Bollen, et al., Phys. Lett. A **158**, 247 (1991).

[49] W. Paul, Rev. Mod. Phys. **62**, 531 (1990).

[50] H. Dehmelt, Rev. Mod. Phys. **62**, 525 (1990).

[51] C. Hao and R. E. March, Int. J. Mass Spectrom. **212**, 337 (2001).

[52] V. I. Baranov and S. D. Tanner, J. Anal. At. Spectrom. **14**, 1133 (1999).

[53] Y. Guo and K. W. M. Siu, J. Am. Soc. Mass Spectrom. **16**, 957 (2005).

[54] M. G. Raizen, J. M. Gilligan, J. C. Bergquist, et al., Phys. Rev. A **45**, 6493 (1992).

[55] K. Kingdon, Physical Review **21**, 408 (1923).

[56] H. Dehmelt, Advan. At. Mol. Phys. **3**, 53 (1967).

[57] W. Paul, O. Osberghaus, and E. Fischer, Forschungsberichte des Wirtschafts- und Verkehrsministeriums Norderhein-Westfalen **415**, 1 (1956).

[58] A. Polyanin and V. F. Zaitsev, *Handbook of Exact Solutions for Ordinary Differential Equations* (Chapman & Hall/CRC, 2002).

[59] M. Abramowitz and I. A. Stegun, *Handbook of Mathematical Functions With Formulas, Graphs and Mathematical Tables* (Wiley-Interscience, 1993).

[60] W. Paul and H. Steinwedel, Z. Naturforsh. A **8**, 448 (1953).

[61] P. H. Dawson, ed., *Quadrupole Mass Spectrometry and its Applications* (AIP Press, 1995).

[62] F. G. Major and H. G. Dehmelt, Phys. Rev. **170**, 91 (1968).

[63] S. Schwarz, Nucl. Instr. and Meth. in Phys. Res. A **566**, 233 (2006).

[64] G. Bollen, *The Euroschool lectures on physics with exotic beams, Vol. I* (Springer, 2004), p. 169.

[65] G. Bollen, R. B. Moore, G. Savard, et al., J. Appl. Phy. **68**, 4355 (1990).

[66] M. König, G. Bollen, H.-J. Kluge, et al., Int. J. Mass Spectrom. Ion. Procress **142**, 95 (1995).

[67] G. Graff, H. Kalinowsky, and J. Traut, Z. Phys. A **297**, 35 (1980).

[68] S. Becker, G. Bollen, F. Kern, et al., Int. J. Mass Spectrom. **99**, 53 (1990).

[69] G. Bollen, in *Cortina D'Ampezzo, Italy* (July 3-7, 2006).

[70] G. Bollen, Nucl. Phys. A **693**, 3 (2001).

[71] H. Weick, H. Geissel, C. Scheidenberger, et al., Nucl. Instr. and Meth. B **164-165**, 168 (2000).

[72] P. Lofy, Ph.D. thesis, Michigan State University (2003).

[73] L. Weissman, D. A. Davies, P. A. Lofy, et al., Nucl. Instr. and Meth. A **531**, 416 (2004).

[74] L. Weissman, D. A. Davies, P. A. Lofy, et al., Nucl. Instr. and Meth. A **522**, 212 (2004).

[75] L. Weissman, D. Morrissey, G. Bollen, et al., Nucl. Instr. and Meth. B **540**, 245 (2005).

[76] T. Sun, Ph.D. thesis, Michigan State University (2006).

[77] G. Gabrielse and J. Tan, J. Appl. Phys. **63**, 5143 (1988).

[78] R. Ringle, G. Bollen, A. Prinke, et al., Int. J. Mass Spectrom. (In Press).

[79] R. Ringle, Ph.D. thesis, Michigan State University (2006).

[80] N. Daly, Rev. Sci. Instrum. **31**, 264 (1960).

[81] D. A. Dahl, Int. J. Mass Spectrom. **200**, 3 (2000).

[82] M. Wada, Y. Ishida, T. Nakamura, et al., Nucl. Instr. and Meth. B **204**, 570 (2003).

[83] T. Kim, A. V. Tolmachev, R. Harkewicz, et al., Anal. Chem. **72**, 2247 (2000).

[84] V. L. Varentsov and D. Habs, Nucl. Instr. and Meth. A **490**, 16 (2002).

[85] V. L. Varentsov and A. A. Ignatiev, Nucl. Instr. and Meth. A **413**, 447 (1998).

[86] L. Weissman, P. Lofy, D. Davies, et al., Nucl. Phys. A **746**, 655c (2004).

[87] J. Richards, R. Huey, and J. Hiller, Int. J. Mass Spectrom. Ion Phys. **10**, 486 (973).

[88] M. A. N. Razvi, X. Z. Chu, R. Alheit, et al., Phys. Rev. A **58**, R34 (1998).

[89] W. M. Brubaker, Advan. Mass Spectrom. **4**, 293 (1968).

[90] Y.-J. Fu, J. Laskin, and L.-S. Wang, Int. J. Mass Spectrom. **255**, 102 (2006).

[91] G. Garcia, E. Mejia-Ospino, A. Guerrero, et al., Int. J. Mass Spectrom. **261**, 53 (2007).

[92] W. E. Boxford, M. O. E. Ghazaly, C. E. Dessent, et al., Int. J. Mass Spectrom. **244**, 60 (2005).

[93] A. Wapstra, G. Audi, and C. Thibault, Nucl. Phys. A **729**, 129 (2003).

[94] G. Bollen, H.-J. Kluge, M. König, et al., Phys. Rev. C **46**, R2140 (1992).

[95] R. Birge, Physical Review **40**, 207 (1932).

[96] J. A. Clark, K. S. Sharma, G. Savard, et al., Phys. Rev. C **75**, 032801(R) (2007).

[97] C. Davids, *Proceeding 6th International Conference on Atomic Masses and Fundamental Constants (AMCO-6)* p. 419 (1980).

[98] J. A. Clark, G. Savard, K. S. Sharma, et al., Phys. Rev. Lett. **92**, 192501 (2004).

[99] C. Guénaut, G. Audi, D. Beck, et al., Phys. Rev. C (Accepted for publication).

[100] J. A. Clark, Ph.D. thesis, U. Mannitoba (2005).

[101] J. C. Hardy, J. A. MacDonald, H. Schmeing, et al., Physics Letters B **63**, 27 (1976).

[102] J. A. Macdonald, J. C. Hardy, H. Schmeing, et al., Nucl. Phys. A **288**, 1 (1977).

[103] J. Jänecke, T. ODonnell, and V. Goldanskii, Nucl. Phys. A **728**, 23 (2003).

[104] T. Rauscher and F.-K. Thielemann, At. Dat. Nucl. Dat. Tab. **75**, 1 (2000).

[105] M. Chartier, W. Mittig, N. A. Orr, et al., Nucl. Phys. A **637**, 3 (1998).

[106] M. Hausmann, J. Stadlmann, F. Attallah, et al., Hyperfine Interactions **132**, 289 (2001).

[107] B. E. Tomlin, C. J. Barton, N. V. Zamfir, et al., Phys. Rev. C **63**, 34314 (2001).

[108] G. F. Lima, A. Lépine-Szily, G. Audi, et al., Phys. Rev. C **65**, 44618 (2002).